Investigating the Physicochemical Properties of $B_{12}X_{12}^{2-}$ (X = H, F, Cl, Br, I)

by

Su Ji Lim

A thesis
presented to the University of Waterloo
in fulfillment of the
thesis requirement for the degree of
Master of Science
in
Chemistry

Waterloo, Ontario, Canada, 2019

Author's Declaration

This thesis consists of material all of which I authored or co-authored: see Statement of Contributions included in the thesis. This is a true copy of the thesis, including any required final revisions, as accepted by my examiners.

I understand that my thesis may be made electronically available to the public.

Statement of Contributions

Chapter 4 investigates $B_{12}X_{12}^{2-}$ (X = H, F, Cl, Br, I) using photoelectron spectroscopy and contains experimental data for $B_{12}X_{12}^{2-}$ (X = F, Cl, Br, I) from a published manuscript in *Journal of the American Chemical Society* with the following authors: Jonas Warneke, Gao-Lei Hou, Edoardo Aprà, Carsten Jenne, Zheng Yang, Zhengbo Qin, Karol Kowalski, Xue-Bin Wang, and Sotiris S. Xantheas. As well, it contains experimental data for $B_{12}H_{12}^{2-}$ from a published manuscript in *Journal of Chemical Physics* with the following authors: Edoardo Aprà, Jonas Warneke, Sotiris S. Xantheas, and Xue-Bin Wang.

Chapter 5 investigates $B_{12}F_{12}^{2-}$ in solution and contains data from a recently published manuscript in *Journal of Physical Chemistry Letters*. The co-authors, along with me, are: Meixin Cheng, Nicolás Rivas, Kostyantyn Pichugin, Ariel A. Petruk, Anna Klinkova, Rodney Smith, Germán Sciaini, and W. Scott Hopkins. I have performed part of the electronic structure calculations presented in this work.

Abstract

This thesis focuses on $B_{12}X_{12}^{2-}$ (X = H, F, Cl, Br, I) experimentally and computationally to understand the fundamental behaviour of this multiply charged anion (MCA) in the gas and solution phases. The thesis explores three different phases of $B_{12}X_{12}^{2-}$: gas phase, micro-solvated phase, and solution phase. This allows for the breakdown of the phenomena affecting the stability of the MCA in solution into the MCAs geometric and electronic properties and solvent-binding interactions.

The first study investigates the dynamic clustering behaviour between $B_{12}X_{12}^{2-}$ (X = H, F) and solvent molecules in the gas phase. Differential mobility spectrometry (DMS) is used to induce micro-solvation states of the MCA as an approach to bridge the gas and solution phase properties. DMS is coupled with computational studies to draw connections from the microsolvation states and solvent interaction potentials. This will provide a means to investigate the dominance of the effects of the individual interactions on stability of the dianion.

The second project explores the bare anion of $B_{12}X_{12}^{2-}$ (X = H, F, Cl, Br, I) in the gas phase. Photoelectron spectroscopy (PES) is simulated and compared with the experimental data for a great understanding of the vibronic transitions and electronic structure of the dianion and its monoanionic counterpart. Geometric distortions after electron detachment are also simulated to determine geometric effects on the stability of the $B_{12}X_{12}^{2-}$. Additionally, various computational methods are explored to investigate their accuracy in predicting the MCA's electronic structure.

The solution phase behaviour of $B_{12}F_{12}^{2-}$ is explored in the final chapter, coupling the findings with the knowledge gained in the first two projects. The solvated $B_{12}F_{12}^{2-}{}_{aq}$ is studied

using femtosecond pump probe absorption spectroscopy to investigate the role of charge-transfer-to solvent in stabilizing the MCA.

The investigations detailed in this thesis reveal the intricacies of the electronic and geometric structures of the species in the gas and solution phases. It is concluded that as repulsive Coulombic factors along with solvent interactions determine the stability of the ground and electronic excited states of the MCA in solution phase.

Acknowledgements

I would like to thank my wonderful supervisor Dr. W. Scott Hopkins for always providing me with guidance, advice and offering his scientific expertise during my graduate studies. I could not have succeeded in my degree without him. I would also like to thank my committee members Dr. Terry McMahon, Dr. Marcel Nooijen, and Dr. Germán Sciaini for their unwavering support. Having a knowledgeable committee composed of renowned scientists has greatly improved my learning experience throughout my degree. Additional thanks to past and present members of the Hopkins group for providing a constructive learning environment with constant support and assistance. Finally, I would like to thank my family, friends and Spencer for their constant belief in my academic capabilities. Without their help I would not be the person I am today, I am forever grateful.

Table of Contents

List of Figures

List of Tables

List of Abbreviations

ACE	Acetone
ACN	Acetonitrile
ADE	Adiabatic detachment energies
AMBER	Assisted model building with energy refinement
Aug-cc-PVQZ	Augmented correlation consistent polarized valence quadruple-zeta
B3LYP	Becke, three parameter, Lee-Yang-Parr
bb	Broadband
CHELPG	Charges from electrostatic potentials using a grid-based method
CIS	Configuration iteration single-excitation
CTTS	Charge-transfer-to-solvent
CV	Compensation voltage
DAS	Decay associated spectrum
DFT	Density functional theory
DMS	Differential mobility spectrometry
EC/EMC	Ethylene carbonate/Ethyl-methyl carbonates
EOM-CCSD	Equation of Motion Couple Cluster Single Double
ESI	Electrospray ionization
FCF	Franck-Condon factor
fs	Femtosecond
GF	Global fitting
IPA	Isopropyl alcohol
IR	Infrared
IRMPD	Infrared multiply photon disassociation
LCAO	Linear combination of atomic orbitals
LUMO	Lowest unoccupied molecular orbital
MCA	Multiply-charged anions
MD	Molecular dynamics
MeOH	Methanol
NIR	Near infrared
PCM	Polarizable continuum model
PES	Photoelectron spectroscopy
PFA	Perfluoroalkoxy
PID	Proportional integral derivative
RCB	Repulsive Coulomb barrier
SCF	Self-consistent field
SP	Single pulse
SPC	Simple point charge
SV	Separation voltage
TA	Transient absorption
TCO	Transparent conductive oxides
TD-CAM-B3LYP	Time-dependent Coulomb-attenuating method B3LYP
TD-DFT	Time-dependent density functional theory
TEA	Triethylammonium
TM	Transition metal

UMO	Unoccupied molecular orbitals
UV	Ultraviolet
VDE	Vertical detachment energy
Vis	Visible
VTE	Vertical transition energy
YAG	Yttrium Aluminum Garnet

Chapter 1. Introduction

Multiply charged anions (MCAs) are an interesting class of molecular ions owing to their relative stabilities and unique gas-phase properties.[1–3] Formally, they are molecular ions that bind multiple electrons in excess of their nuclear charge. $B_{12}X_{12}^{2-}$ (X = H, F, Cl, Br, I), a highly symmetric doubly-charged anion, is a promising candidate in the understanding of MCA stability.[1,2] Due to their inert properties, boron-containing species are reported in the medical field as a key component in boron-based neutron capture cancer therapy. [4–6] Other applications include using salts of polyhedral borane and carborane anions and metal ions as electrolytes, catalysts, or in hydrogen/ammonia storage.[4–6]

Recent studies of MCAs in the gas phase have used infrared (IR) multiphoton dissociation (IRMPD) spectroscopy to characterize their geometric structure and physicochemical properties.[7–9] The IRMPD studies conducted by Carr *et al.* studied triethylammonium (TEA) complexed with $B_{12}X_{12}^{2-}$ (X = F, Cl) and identified the two lowest energy dissociation pathways in the fragmentation process: proton-transfer to produce $HB_{12}X_{12}^{-}$ (X = F, Cl) and charge transfer to yield $B_{12}X_{12}^{-}$ (X = F, Cl).[9] Carr *et al.* noticed that $B_{12}X_{12}^{-}$ became more reactive relative to $B_{12}X_{12}^{2-}$.[9] The Hopkins group previously investigated the infrared-driven charge-transfer between the transition metal (TM) ion (TM = Co(II), Ni (II), Zn (II), Cd (II) and $B_{12}X_{12}^{2-}$ (X = H, F); IRMPD of the mixed-cage species yielded appreciable amounts of $B_{12}H_{12}^{-}$ and $B_{12}F_{12}^{-}$ in most cases.[7,8] Charge transfer to the TM cation, leading to monoanion formation dominated the process.[7–9] Upon irradiating the monoanion with IR radiation, fragmentation of the cage occurred, breaking the icosahedral symmetry.[7–9]

These studies highlight the dianion's high stability relative to monoanion and confirm the correlation between the stability of the charge and the geometric structure of the

monoanion.[7–9] However, it is less clear how geometry and electronic structure are related to MCA stability. In this thesis differential mobility spectrometry, photoelectron spectroscopy, femtosecond pump-probe spectroscopy, and corresponding computational work on $B_{12}X_{12}^{2-}$ (X = H, F, Cl, Br, I) are discussed as a means for further insight into the geometric and electronic structure effects on the MCA's stability.

Studies of $B_{12}X_{12}^{2-}$ in gas and solution phase will be approached by a combination of experimental and computational methods. In Chapter 2, the fundamental theory behind the methods used will be explained. We mainly employed density functional theory (DFT) for calculating the optimized geometries, electronic energies, and thermochemical information on the molecule of interest. In order to study the dynamic interaction between $B_{12}X_{12}^{2-}$ and solvents, DMS will be introduced. The PES and pump probe experiments will also be introduced. Detailed methods will be described at the corresponding chapter.

Chapter 3 explores the dynamic clustering behaviour of the $B_{12}X_{12}^{2-}$ (X = H, F) species using DMS. The DMS applies an asymmetric radiofrequency waveform across two planar electrodes affecting ion trajectory passing through the cell.[10] An ion's differential mobility in the cell is affected by its physicochemical properties, which can be further manipulated through the introduction of solvent vapour and inducing cluster formation between the ion and solvent.[10] DMS allows for the investigation of clustering interactions of the boron species in the gas-phase within different clustering environments.[10,11,12] Computational calculations are also performed to estimate chemical properties such as solvent binding energies and electrostatic interactions. Connections to the micro-solvated states and hence solvent interaction potentials of the boron icosahedron are drawn from these investigations.

Chapter 4 examines the calculated electronic structures of $B_{12}X_{12}^{2-}$ (X = H, F, Cl, Br, I) species. The study compares the simulated PES generated from energies of occupied orbitals to the experimentally generated PES performed by Warneke *et al.* at the Pacific Northwest National Laboratory.[13,14] Comparison of theoretical results with experimental observations facilitates the estimation of vertical detachment energies (VDEs) and adiabatic detachment energies (ADEs) as well as vibrational frequencies for low-energy electronic states in $B_{12}X_{12}^{2-}$. PES also allows for the determination of vibronic excitations in the nascent monoanion following detachment.[15] Information on the electronic properties of the boron icosahedra is thus acquired to provide further insight into the species' stability.

MCAs display unique solvent stabilizing effects.[1,3,16] As an example, SO_4^{2-} and PO_4^{3-} are known to be stable in aqueous environments but experience spontaneous electron detachment in the gas phase.[1,3,16] This is a result of strong Coulomb repulsion arising from excess negative charge.[1,2] Regardless of stability in solution, MCAs have low photodetachment thresholds and the ability to inject electrons into the solvent *via* CTTS states on the sub-picosecond timescale.[17,18] In Chapter 5, we report a spectroscopic study of $B_{12}F_{12}^{2-}$, which shows blocking of "CTTS-like" electron ejection. We rationalize these observations *via* an apparent repulsive Coulomb barrier (RCB) which traps the electron. The RCB is an established feature of the potential energy landscape of MCAs *in vacuo*,[13,19] which we have found also applies to the solution phase.

In summary, this thesis presents the results of solution-phase, single molecule and cluster experiments. The synthesis and interpretation of these results give a broad picture of the physicochemical properties of $B_{12}X_{12}^{2-}$ in solution and in the gas phase. In Chapter 3, dynamic clustering behaviour for $B_{12}X_{12}^{2-}$ is examined to draw connections to microsolvation states and solvent interaction potentials. In Chapter 4, PES of $B_{12}X_{12}^{2-}$ is determined to acquire a deeper

understanding the electronic structure. The solution-phase behaviour of $B_{12}X_{12}^{2-}$ studies in Chapter 5 is better understood with the conclusions put forth in Chapters 3 and 4 on micro-solvation states and RCB. The investigations described in this thesis reveal the intricacies of the electronic and geometric structures of the species in the gas and solution phases. By studying these properties in tandem, $B_{12}X_{12}^{2-}$ species can be used as a stepping stone to better explain MCA behaviour.

Chapter 2. Methods

2.1 Overview

The principles of each instrumental setup used in the experiments described in this thesis are discussed in this chapter. Instrument optimization and set up for the experiments conducted are detailed in their corresponding chapters.

2.2 Introduction to theoretical methods

DFT is a useful quantum chemistry method that is utilized to study the electronic structure of molecules. Compared to wavefunction based methods, DFT uses spatially dependent electron density functionals to model the electronic structure of many-electron systems.[20,21,22,23] The electronic energy is defined in terms of kinetic energy, electron-nuclear interaction energy, electron-electron interaction energy, and exchange-correlation energy.

As in wavefunction methods, electron density functionals are defined in terms of common basis sets included in the Gaussian software package.[24] Appropriate basis sets should be used depending on the molecular system to better approximate the wavefunction. Split-valence basis sets employ a single basis function for each core orbital and larger basis function for the valence orbitals.[20,23,25] Polarized sets may be used when atoms are brought together, as they account for distorted atomic orbitals caused by polarization.[20] In cases where electron density lies far from the nucleus, e.g. anions, diffuse basis sets are recommended.[20]

Time-dependent DFT (TD-DFT) is an applied DFT method that investigates the properties of electronically excited states such as excited state structures, vertical transition energies (VTEs) and emission wavelengths.[26] An advantage of using TD-DFT is the ability to map the excited states relative to the ground electronic state.[26] The calculated excited electronic states will be compared with the results from experiments photoelectron spectroscopy and pump-probe experiments.

2.3 Introduction to differential mobility spectrometry

DMS is a variant of ion mobility spectrometry that relies on the differences in ions' abilities under high and low electric fields.[10] In DMS, a radiofrequency asymmetric waveform is applied across two planar electrodes to affect the trajectory of ions in the gas phase passing through the cell (Figure 2.1 a).[10,27] In our experiments, samples are ionized by electrospray ionization (ESI) and carried through the DMS by a neutral carrier gas (N_2).[10,28] An ion's mobility is affected by its size (*i.e.*, collision cross section), its temperature, and the strength of the electric field.[10] Thus, as an ion passes through the DMS, its dynamic clustering and declustering process under low and high fields results in an off-axis trajectory towards one of the electrodes neutralizing the ion.[10] A direct current voltage, the compensation voltage (CV), is applied to stabilize the trajectory and allow the ion to pass through the cell.[10] The CV value required to correct the trajectory as one increases separation voltage (SV) is characteristic of an ion's physicochemical properties.[29,30]

Seeding the carrier gas with solvent molecules (1.5% v/v) leads to the formation of ion-solvent complexes.[10] This alters the apparent collision cross section (CCS) of the ions and hence their trajectory through the DMS cell.[29,31] One can acquire information on the ion's physicochemical properties and its solvent interactions by recording the change in CV value as a function of SV.[10] A schematic diagram of the DMS is shown in Figure 2.1.

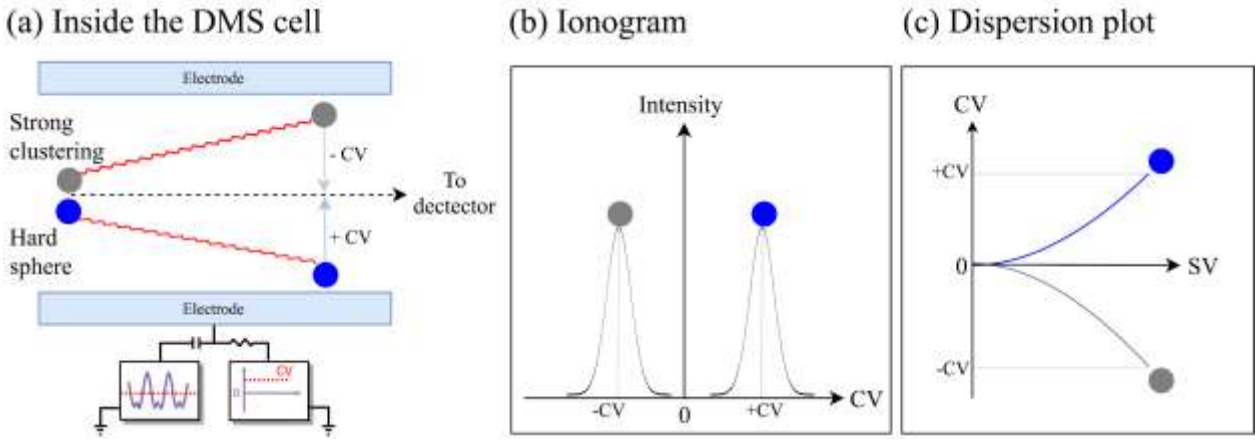

Figure 2.1. Analyte ions in the gas phase are carried through the DMS cell between two planar electrodes by N_2. The carrier gas can be seeded with neutral solvent molecules to induce clustering behaviour in the DMS, affecting the mobility of the ion. SV is applied to one of the planar electrodes altering the ion's trajectory off-axis which is corrected by ramping a direct current CV to determine the optimal CV value for each ion.

Ions display three different behaviours depending on how strongly they cluster with carrier gas and/or solvent vapours.[10] The extent of clustering is dictated by the intermolecular interactions between the ion and solvent modifiers.[10,29] The three main types of DMS clustering behaviours are shown in Figure 2.2.

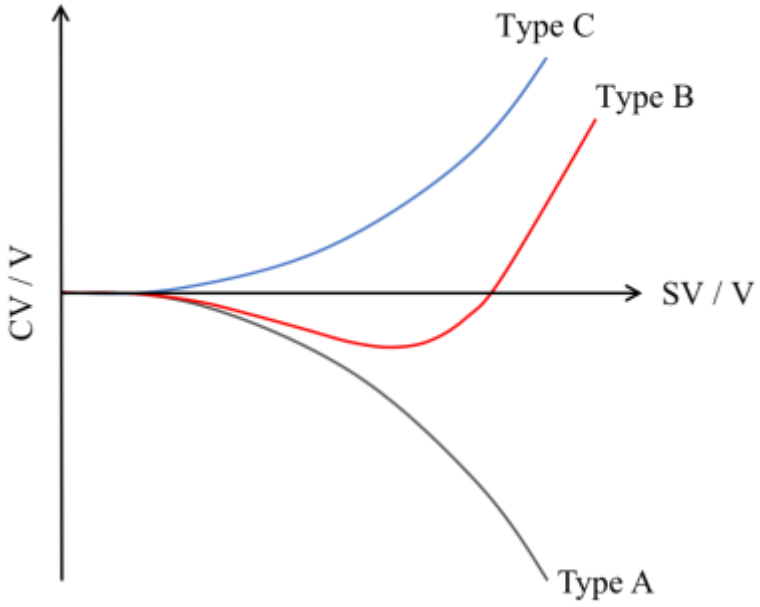

Figure 2.2. Three DMS behaviours are shown as a function of CV and SV. Type A is characterized by an increasingly negative CV as SV increases. Type C occurs when CV increases as SV increases. Type B is a mixture of the two where CV initially decreases and then increases at some critical SV point.

Type A is typified by an increasingly negative CV for optimal ion transmission with increasing SV. This is attributed to "strong" interactions between analyte ions and solvent vapours.[10] This can be understood in terms of the dynamic clustering and declustering processes under low and high fields, respectively. At low field, clustering between the ion and neutral molecules can occur, increasing the apparent CCS.[10] As the cluster migrates through the DMS cell, it collides with carrier gas molecules that lead to a reduction in ion mobility.[29,31] Under high field, ion-neutral collisions are sufficiently energetic to desolvate the ions, leading to declustering and a reduction in apparent CCS.[10] This results in fewer ion-neutral collisions and a higher relative mobility.[29] Figure 2.3 illustrates the dynamic clustering and declustering cycle.

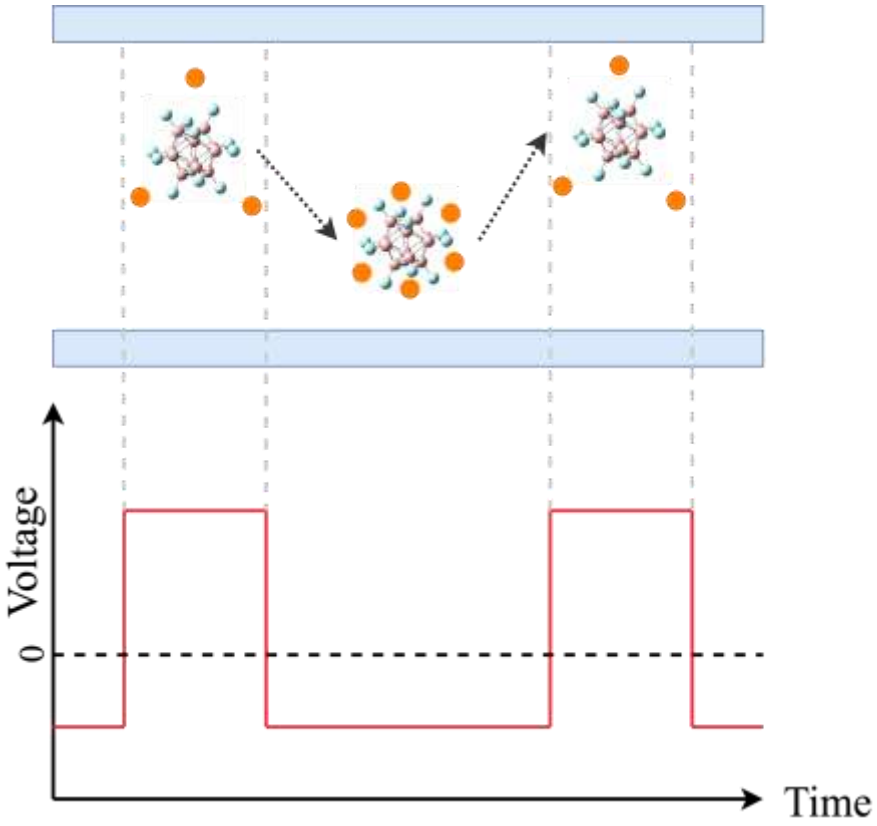

Figure 2.3. At low field, clustering occurs between the analyte and solvent molecules, increasing the apparent CCS. At high field, sufficient energy is acquired to decluster the formed clusters, reducing the apparent CCS and increasing mobility.

Type C behaviour is observed as an increase in CV as SV increases. This is behaviour is also referred to as hard-sphere behaviour, as the clustering process is minimal, leading to a negligible difference in CCS at high and low field.[10,28] Type B is a combination of both Type A and Type C. At low SV values, the ion exhibits Type A behaviour, in which the process of clustering and declustering is observed.[10] However, at a critical SV value, sufficient energy is acquired in which solvent molecules are boiled off more rapidly leading to an observed Type C behaviour.[10,28] Temperature also affects the ion's DMS behaviour, as stated earlier. As the temperature increases, the strength of the cluster formed between the ion and the solvent molecules is reduced.[10] This can lead to a change in behaviour from Type A to Type B to Type C as temperature is increased.[29] Modifying the temperature to achieve a Type B behaviour a useful tool to determine the binding energy of clusters formed in the DMS. The critical SV point in Type B clustering is proportional to the binding energy of the ion solvent cluster,[10,11] which then provides information on the solvent binding interactions of the analyte.[29] A combination of DMS results with computational data is an effective strategy in obtaining thermodynamic data on the analyte species.

2.4 Photoelectron spectroscopy

PES exploits the photoelectric effect to determine the binding energies of solids, liquids, and gas.[15] The photoelectric effect is a phenomenon whereby a photon dislodges an electron from an atom or molecule if the energy of the photon is equal to or greater than the binding energy of the electron.[15] Conservation of energy requires that the photon energy is equal to the sum of the kinetic energy of the ejected electron and its binding energy.[15] This relation is outlined in the following equation:

$$h\upsilon = KE_{electron} + BE\ , \tag{2.1}$$

where *h* is Planck's constant, *v* is the frequency of the photon (in Hz), $KE_{electron}$ is the kinetic energy of the ejected electron (in eV) and *BE* is the binding energy of the electron (in eV). By controlling the frequency of the laser, detecting the speed of the ejected electron and rearranging the equation, the binding energy of the electron can be determined.

The intensity of the spectra is correlated to the Franck-Condon factor (FCF) which describes the probability of a vibrational transition between states. This probability is highest when the transition overlap integral for the initial and final wave functions is maximized:[32]

$$|\langle\mu\rangle|^2 = \left|\left\langle {\psi^*}_{total,f}(\vec{r})\middle|\vec{\mu}(\vec{r})\middle|\psi_{total,i}(\vec{r})\right\rangle\right|^2$$
$$= \left|\left\langle {\psi^*}_{nuc,f}(\vec{r})\middle|\psi_{nuc,i}(\vec{r})\right\rangle\left\langle {\psi^*}_{el,f}(\vec{r})\middle|\vec{\mu}(\vec{r})\middle|\psi_{el,i}(\vec{r})\right\rangle\right|^2. \quad (2.2)$$

The $\vec{\mu}(\vec{r})$ is the dipole moment operator. The Born-Oppenheimer approximation was made, which states that the electronic and nuclear wavefunctions can be separated as the motion of electrons occur on a much faster time scale than nuclear motion.[32,33]

$$FCF = \left|\left\langle {\psi^*}_{nuc,f}(\vec{r})\middle|\psi_{nuc,i}(\vec{r})\right\rangle\right|^2. \quad (2.3)$$

When this transition overlap integral is evaluated, it yields the FCF. The probability distribution of the wavefunctions impact the transition probability significantly.[34] In the case of a different vibrational quantum number between wavefunctions, the transition probability is governed by the FCF.[34] These different vibrational wavefunction overlap scenarios are shown in Figure 2.4:

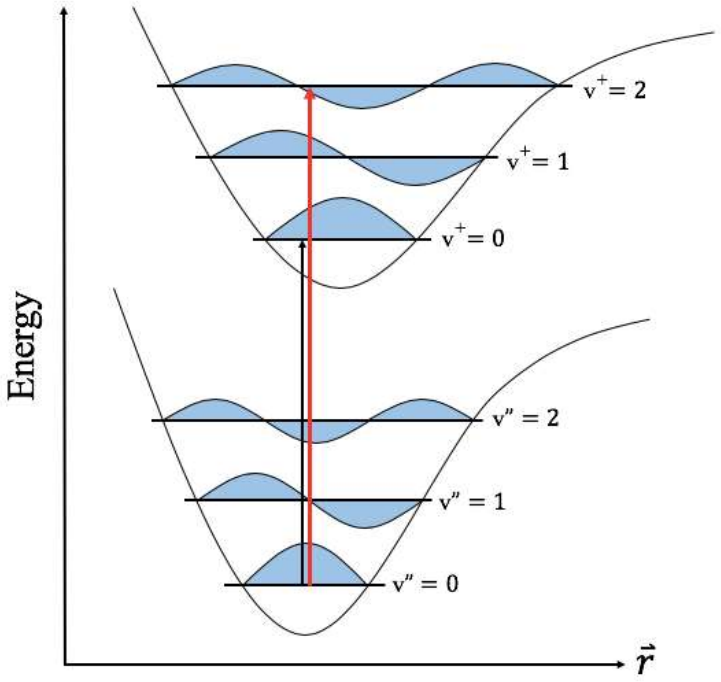

Figure 2.4. The FCF refers to the overlap between the wavefunction of the two vibrational states for a vertical excitation between two electronic states.[15] The transition marked by the black arrow has a greater overlap than that marked by the red arrow.

2.5 Pump probe absorption

Pump-probe spectroscopy is a two-laser experiment that is used for measurement of excited/transient states.[35] In the pump-probe experiments conducted here, a pump pulse excites the sample to a higher electronic state and a second broadband pulse is used to measure the absorbance of the sample in an excited state as shown in Figure 2.5.[35] The absorbance of the excited state is then recorded as a delay, t, introduced between the pump and probe pulses.

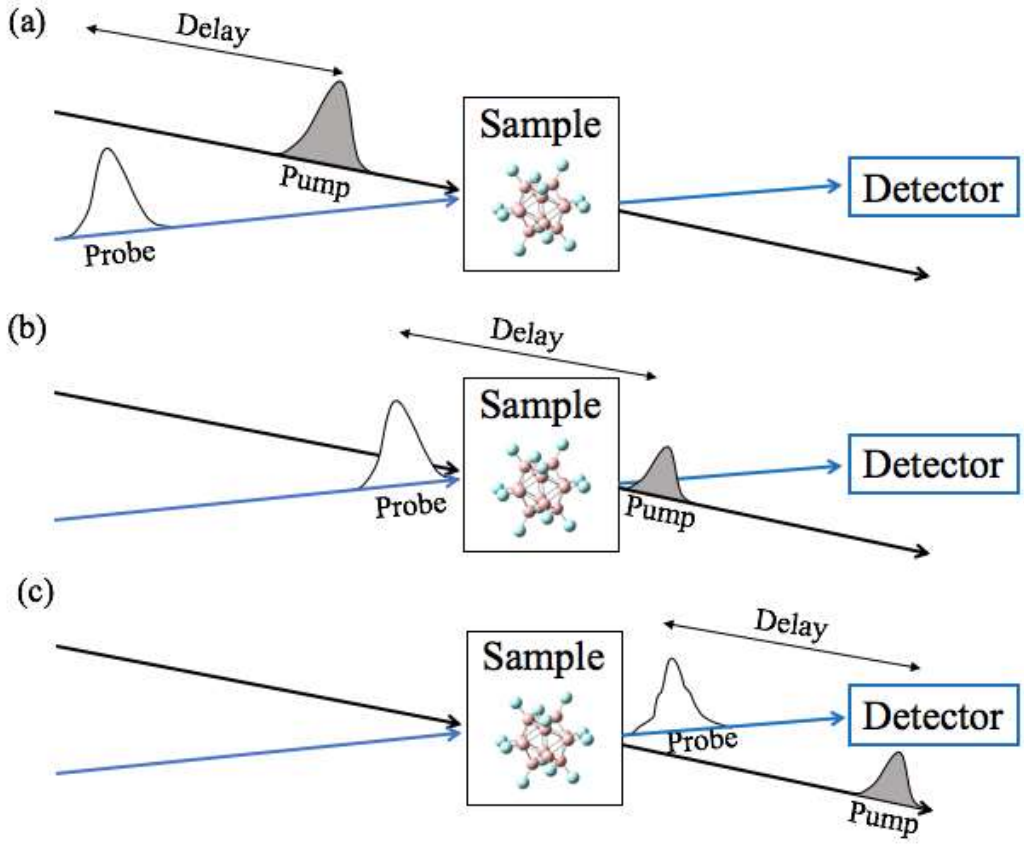

Figure 2.5. Transient spectroscopy can be summarized in the following process. (a) The sample is excited by a pump pulse. (b) The sample then absorbs a light from the probe pulse after a time delay, t. (c) The transmitted intensity is measured in a dispersive spectrometer, as t is varied.

The change in absorbance can be defined as,

$$\Delta A(t) = A(t) - A(t < 0) \tag{2.4}$$

where $A(t)$ is the absorbance as a function of time and $A(t < 0)$ is the absorbance immediately before the pump pulse excites the sample.

$$A(t) = log_{10}\left(\frac{I_0}{I_t(t)}\right) \tag{2.5}$$

The intensity of the probe beam is I_0 and the intensity passing through the sample as a function of time is $I_t(t)$.

$$\Delta A(t) = log_{10}\left(\frac{I_0}{I_t(t)}\right) - log_{10}\left(\frac{I_0}{I_t(t < 0)}\right) \tag{2.6}$$

This equation can be simplified to

$$\Delta A(t) = log_{10}\left(\frac{I_t(t<0)}{I_t(t)}\right). \quad (2.7)$$

By measuring the absorbance as a function of the time delay between the pump and probe pulses, it is possible to determine the relaxation process of transient excited species and observe solvent reorganization dynamics.[35] The corresponding energies of the peaks in the absorbance spectrum determine the excitation energies of the sample.[35]

Chapter 3. $B_{12}X_{12}^{2-}$ (X = H, F) Differential Mobility Spectrometry

3.1 Introduction

The $B_{12}X_{12}^{2-}$ (X = H, F) dianions and clusters containing these species have garnered interest due to the relatively high stability of these systems.[1,2,13] MCAs are commonly unstable and readily undergo spontaneous electron detachment in the gas phase to yield the monoanion owing to the large Coulombic repulsion between the excess electrons.[1,2] Quite interestingly, though, species such as $B_{12}X_{12}^{2-}$ (X = H, F) exhibit electron delocalization and pairing energy to not only be stable in solution but also the gas phase.[1,7] In order to gain a better understanding of $B_{12}X_{12}^{2-}$ (X = H, F) intermolecular interactions, we explore the ion-solvent interactions within an atmosphere of N_2 seeded with 1.5% (v/v) solvent using DMS. Experimental results are supported with high level computational studies.

In a recent study, Campbell *et al.* theoretically calculated binding energies for tetramethlammonium with a single-solvent molecule at the B3LYP/6-311++G(d,p) level and compared them to the SV at the CV extremum that was observed using DMS.[12] The strong correlation between SV at CV_{min} and calculated binding energy (BE) implied that SV at CV_{min} could be interpreted as the point at which field-induced heating overcame the average ion-solvent BE.[12] Here we look to explore this relationship further by studying the dynamic clustering between $B_{12}X_{12}^{2-}$ (X = H, F), a relatively large MCA, and a variety of solvent molecules.

3.2 Methods

3.2.1 Computational methods: Density functional theory

Theoretical calculations were performed using the Gaussian 16 quantum chemistry software.[24] $[Solv{\bullet}B_{12}X_{12}]^{2-}$ (X = H, F) cluster structures were initially optimized at the B3LYP/Def2-SVP level of theory prior to employing the Def2-TZVPP basis set with GD3 empirical dispersion correction, and the analytical free matrix was recalculated every 5 iterations to ensure location of a local minimum. In addition, quadratically converged self-consistent field was employed with a reduced convergence criterion of 1×10^{-8} instead of the default of 1×10^{-7}.

Thermodynamic properties of the system, including the Gibbs free energy, zero-point energies, enthalpies, and entropy values, were extracted from frequency calculations performed on the optimized geometries. The change in Gibbs free energy is then obtained by:

$$\Delta G = \Sigma G_{products} - \Sigma G_{Reactants}, \tag{3.1}$$

in which G represents the thermodynamic property in question.

3.2.2 Reagents and Chemicals

Dried, solid $Na_2B_{12}H_{12}$ and $K_2B_{12}F_{12}$ salts were purchased from Sigma Aldrich. HPLC-grade methanol (MeOH), acetonitrile (ACN), isopropyl alcohol (IPA), acetone (ACE), and 18 mQ ultra-pure water were used as the solvent vapours seeded into the curtain gas of the DMS cell.

3.2.3 Differential Mobility Spectrometry – Mass Spectrometry

Refer to Section 2.2 for a detailed description of DMS-MS. Table 3.1 summarizes the ESI and DMS conditions employed for $B_{12}X_{12}^{2-}$ (X = H, F) experiments.

Table 3.1. ESI conditions used for the analysis of the $B_{12}X_{12}^{2-}$ (X = H, F) species.

Sample Preparation			
ESI Solvent		MeOH:H_2O (+ 0.1% Formic Acid)	
ESI Salt		$Na_2B_{12}H_{12}$ or $K_2B_{12}F_{12}$	
Sample Concentration		100 ng/mL	
Source/Gas Conditions			
Ion Source	TurboSpray	Polarity	Negative
Ion Source Gas 1	20 psi	Temperature	34 °C
Ion Source Gas 2	0 psi	Curtain Gas	20 psi
Ion Spray Voltage	−4500V	Collision Gas	High
Compound Conditions			
Declustering Potential		−100 V	
Collision Energy		−10 V	
Entrance Potential		−10 V	
DMS Conditions			
DMS Temperature		150 °C, 225 °C, 300 °C	
DMS Offset		−3.0 V	
CV Ramp		0.1 V	
Resolving Gas		Off	

To determine the clustering behaviour of the $B_{12}X_{12}^{2-}$ (X = H, F) samples, the SV was ramped from 0 V to 4000 V (*i.e.*, the point at which the DMS electronics commonly trips due to arcing in the cell) stepping at 500 V increments from 0 V to 3000 V, and 200 V increments from 3000 V to 4000V. The intervals at higher SV are reduced due to the large expected shift in optimal CV value as SV is increased. CV was ramped up by 0.1 V increments and the range was shifted to keep the entire ion signal within the CV bounds. Optimal CV values for ion transmission, *i.e.*, the peaks of the ionogram for each SV, describe a dispersion plot that may be used to better visualize the analyte clustering behaviour. In order to isolate the ion signal for $B_{12}X_{12}^{2-}$ (X = H, F), a SCIEX QTRAP 5500 triple quadrupole mass spectrometer is used in enhanced product ion (EPI) mode.[36] EPI employs the first quadrupole (Q1) as a selective mass filter and scans the third quadrupole (Q2) for fragment ions as a result of collision induced dissociation (CID) in the second quadrupole (Q2) region.[36] In this case, parent ions are selected in both Q1 and Q3, but EPI also uses Q3 as a

linear ion trap, which increases ion signal by allowing for population buildup in Q3 prior to detection.[36]

Three main clustering behaviours are observed in DMS: Type A (strong clustering or negative CV values), Type B (weak clustering or transition behaviour between Type A and Type C) and Type C (no clustering or positive CV values). The common ion trajectories through DMS are detailed in Section 2.2. In a pure N_2 environment, most ions display purely Type C behaviour, with rare cases of Type B. In polar solvent, Type A behaviour, for which CV values become increasingly negative with increasing SV, are common. Type B is characterized by an initial decrease in CV with increasing SV, resembling Type A, followed by a turnaround at sufficiently high SV, resulting in Type C-like behaviour. We assert that all components which display pure Type A behaviour for all SV under study are in truth Type B compounds for which the turnaround SV has not been reached. With this in mind, each of the Type A and Type B dispersion plots can be characterized using the following functional form:

$$CV = \frac{1 - (a - SV) \cdot e^{-\frac{a-SV}{b+c \cdot SV}}}{d} \tag{3.2}$$

In Equation 3.2, CV is the compensation voltage being fit and SV represents the experimental separation voltage. Fit parameters a, b, c, and d are determined by fitting experimental data to Equation 3.2 using least squares fitting. Function fitting allows for simple comparisons between experimental data. Additionally, Campbell has shown a correlation of ion-solvent binding energy with experimentally determined SV at CV_{min} values.[11,12] Function extrapolation enables determination of these values for experiments which only show Type A behaviour. Of course, extrapolation for SV at CV_{min} is likely to be unreliable, but calculations can provide further insights.

3.3 Results and Discussion

3.3.1 Differential mobility spectrometry

Figure 3.1 and Figure 3.2 show the dispersion plots produced for $B_{12}H_{12}^{2-}$ and $B_{12}F_{12}^{2-}$, respectively, in a pure N_2 environment, and in N_2 seeded with 1.5% (v/v) water (H_2O), MeOH, IPA, ACN, and ACE. DMS experiments were run with temperatures of 150 °C, 225 °C, and 300 °C. The SV at CV_{min} for these studies was extrapolated using Equation 3.2. The dotted curves in the dispersion plots of Figure 3.1 and Figure 3.2 represent the extrapolated curves. Caution is stressed when determining the SV at CV_{min} using the extrapolated data; this methodology provides only a rough estimate of the CV turnaround point.

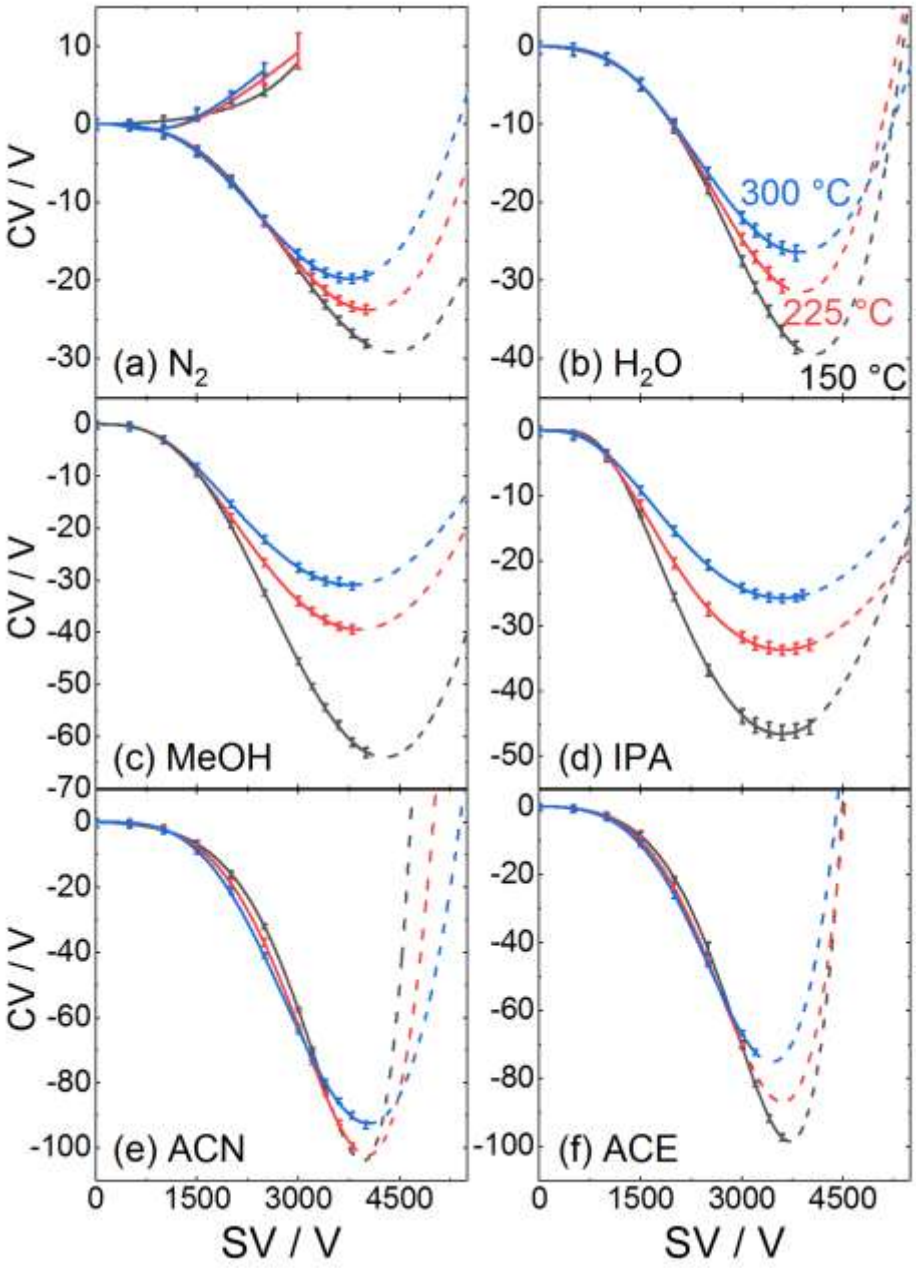

Figure 3.1. The dispersion plots of $B_{12}H_{12}^{2-}$ at different modifiers are shown in (a-f). All modifiers except for ACN and ACE, which showed strong Type A behaviour, exhibited Type B behaviours. The data was extrapolated (shown by the dotted curves) to determine the SV at CV_{min}. Error bars are $\pm\sigma$ obtained from Gaussian fits to the ionogram peaks.

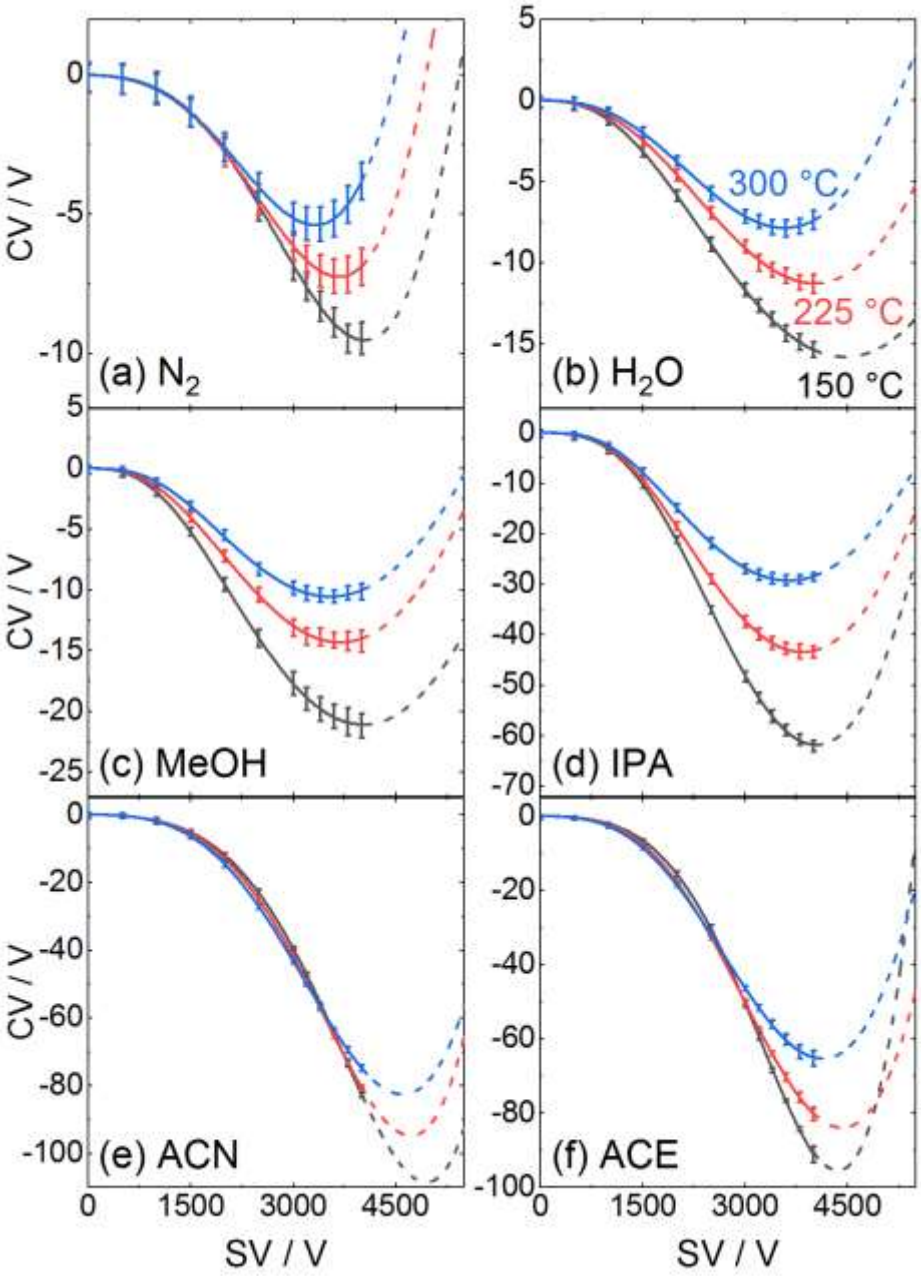

Figure 3.2. The dispersion plots of $B_{12}F_{12}^{2-}$ at different modifiers are shown in (a-f). All modifiers except for ACN and ACE, which showed strong Type A behaviour, exhibited Type B behaviours. The data was extrapolated (shown by the dotted curves) to determine the SV at CV_{min}. Error bars are $\pm\sigma$ obtained from Gaussian fits to the ionogram peaks.

In Figure 3.1 (a), there is an unexpected peak splitting indicating the presence of Type B and Type C clusters. The Type C ion signal disappears at around SV = 3000 V, which typically indicates a strongly bound cluster.[10] This Type C behaviour is likely due to $B_{12}H_{12}^{2-}$ interacting with H_2O or MeOH from the ESI solvent.

Interestingly, there is no peak splitting for $B_{12}F_{12}^{2-}$ in pure N_2 environment, Figure 3.2 (a). This could indicate that $B_{12}F_{12}^{2-}$ does not interact strongly with H_2O or MeOH relative to $B_{12}H_{12}^{2-}$, or that larger clusters containing $B_{12}H_{12}^{2-}$ transit the DMS cell and fragment upon entry into the mass spectrometer when a pure N_2 environment is employed.

The Type B interactions observed in the pure N_2 environment are likely a result of strong electrostatic interactions (*e.g.*, charge-quadrupole and/or charge-dipole interactions). The charge quadrupole interaction can be described by Equation 3.3:

$$\phi_\Theta = \frac{1}{4\pi\epsilon_0}\frac{\Theta}{2}\frac{(3\cos^2\theta - 1)}{\left|\vec{R}_{COM}\right|^3} . \tag{3.3}$$

In Equation 3.3, ϕ_Θ represents the electrostatic potential at $\vec{R}_{COM}$ due to a quadrupole moment orientated such that $\Theta_{zz} = \Theta = -2\Theta_{xx} = -2\Theta_{yy}$. $\vec{R}_{\mathrm{COM}}$ is determined from the centre of mass (COM) distances between $B_{12}X_{12}^{2-}$ and N_2. θ is the angle $\vec{R}_{COM}$ makes with the z-axis of the quadrupole and ϵ_0 is the permittivity of free space. The electrostatic energy is therefore

$$E_{q\Theta} = \frac{q}{4\pi\epsilon_o}\frac{\Theta}{2}\frac{3\cos^2\theta - 1}{\left|\vec{R}_{COM}\right|^3} , \tag{3.4}$$

where $E_{q\Theta}$ represents the charge-quadrupole electrostatic energy, and q is the charge at position $\vec{R}_{COM}$. For N_2 interactions with $B_{12}X_{12}^{2-}$, q = $-2e$ and from literature, $\Theta_{N_2} = -5.01 \times 10^{-40} cm^2$.[37] The minimum for $E_{q\Theta}$ will occur for $\theta = \frac{\pi}{2}$ and using a value for $\vec{R}$ from theoretical calculations, $R_{min} = 5.1$ Å for $B_{12}H_{12}^{2-}$•N_2, the charge quadrupole energy is calculated to be:

$$E_{q\Theta} = \frac{(-2e)}{4\pi\epsilon_0}\frac{(-5.01\times10^{-40}cm^2)}{2}\frac{-1}{(5.1\times10^{-10}m)^3} = -3.37\frac{kJ}{mol} \quad (3.5)$$

In Figure 3.1, Figure 3.2 (b), (c) for the H_2O and MeOH modifier cases, Type C behaviour is not observed. A possibility is that in the modified 1.5% (v/v) MeOH or H_2O environment, solvent interactions act to desolvate / dissociate clustered $B_{12}H_{12}^{2-}$ species so that only one DMS signal is observed. $B_{12}H_{12}^{2-}$ and $B_{12}F_{12}^{2-}$ interaction with polar solvents are likely to be dominated by charge-dipole forces. The charge dipole electrostatic energy is given by

$$E_{q\mu} = \frac{q}{4\,\pi\,\varepsilon_0}\cdot\frac{|\vec{\mu}|\,\left|\vec{R}_{COM}\right|\cos\theta}{\left|\vec{R}_{COM}\right|^3}\,. \quad (3.6)$$

In Equation 3.6, $E_{q\mu}$ is the charge dipole energy, q is the charge of the point ion and $\vec{R}$ is the position vector from the dipole moment to the charge, q. θ is the angle between the dipole vector, $\vec{\mu}$, and $\vec{R}$ as seen in Figure 3.3.

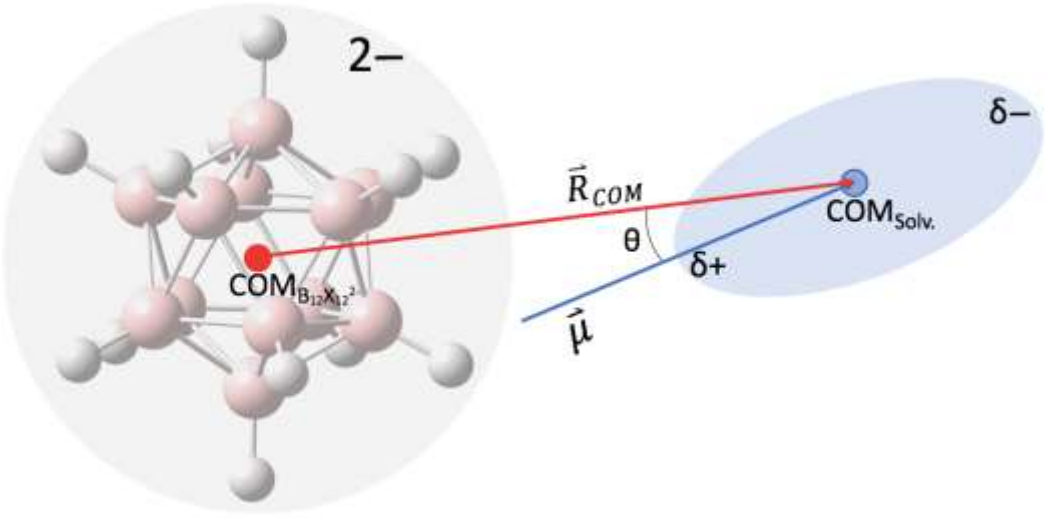

Figure 3.3. The coordinate system used to calculate charge-dipole interactions in $[Solv{\bullet}B_{12}X_{12}]^{2-}$ (X = H, F) clusters.

From Equation 3.6, electrostatic energy is directly proportional to $|\vec{\mu}|$. We expect that if charge dipole interactions dominate, then we should observe stronger binding with increasing modifier dipole. Table 3.2 shows the dipole moments for the modifiers studied.

Table 3.2. The calculated dipole moments of each solvent molecule seeded in the DMS at 1.5% of the curtain gas compared with experimental SV at CV_{min} for $B_{12}H_{12}^{2-}$ and $B_{12}F_{12}^{2-}$ unless stated otherwise.[38]

Modifier	**Dipole Moment‡, $\|\vec{\mu}\|$ (*D*)**	**SV at CV_{min} For $B_{12}H_{12}^{2-}$ At 300 ºC (V)**	**SV at CV_{min} For $B_{12}F_{12}^{2-}$ At 300 ºC (V)**
N_2	0	3760	3320
Isopropyl Alcohol	1.58	3590	3632
Methanol	1.70	3773	3540
Water	1.86	3846	3572
Acetone	2.88	3442*	4132*
Acetonitrile	3.92	4040*	4599*

‡ Dipole moment values are taken from the NIST database.[38]
* These values are taken from predictions using the fitting function.

Referring to Table 3.2 and Equation 3.6, one would expect the trend in SV at CV_{min} to progress in the order of N_2 < IPA < MeOH < H_2O < ACE < ACN, with ACN exhibiting the strongest clustering behaviour. Figure 3.4, Figure 3.5, and Table 3.2 show the determined SV at CV_{min} values. For $B_{12}H_{12}^{2-}$, the trend observed is IPA < MeOH < H_2O < ACN, aligning well with the dipole moment trend. For $B_{12}F_{12}^{2-}$, the trend observed is N_2 < MeOH < H_2O < IPA < ACE < ACN, again demonstrating that the solvent interaction is largely dictated by the dipole moment of the solvent.

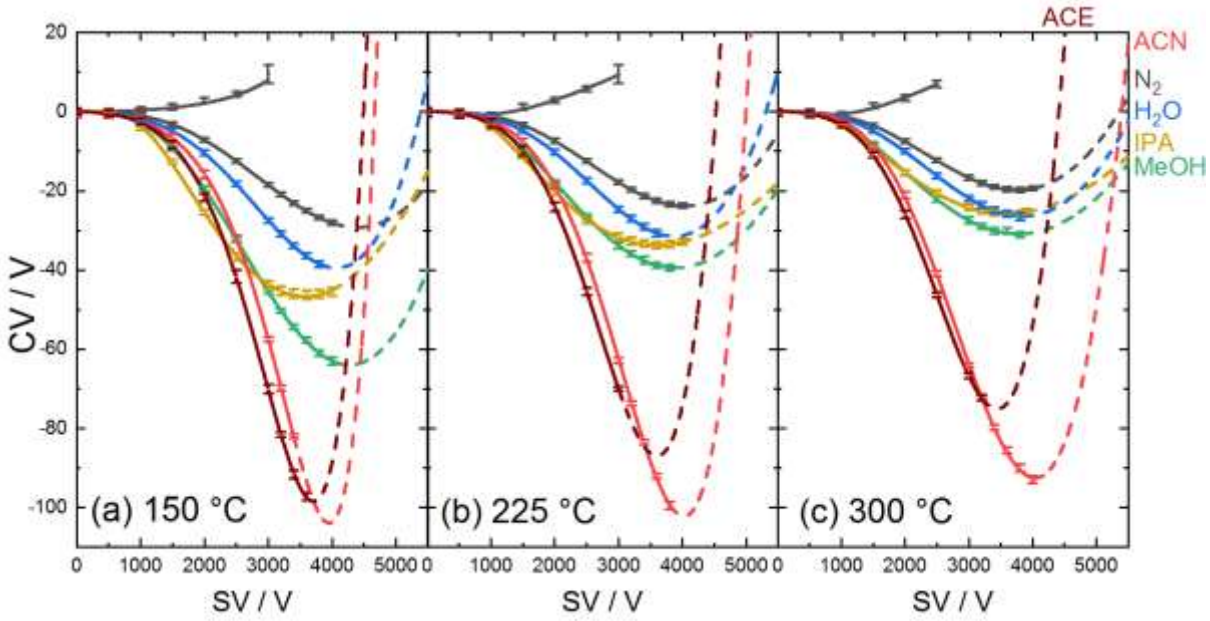

Figure 3.4. The dispersion plots of $B_{12}H_{12}^{2-}$ for different modifiers at (a) 150 °C, (b) 225 °C, and (c) 300 °C are shown, with the extrapolated data shown as dotted lines.

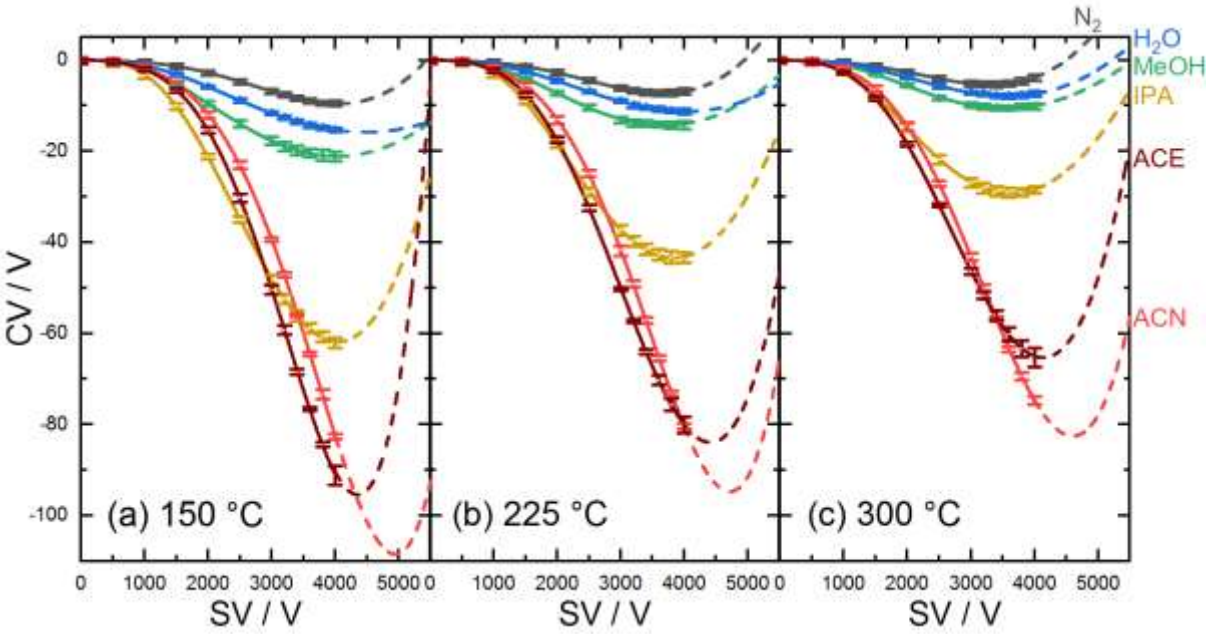

Figure 3.5. The dispersion plots of $B_{12}F_{12}^{2-}$ for different modifiers at (a) 150 °C, (b) 225 °C, and (c) 300 °C are shown, with the extrapolated data shown as dotted lines.

As temperature is increased, the kinetic energy of the system increases. An increase in collisions leads to an overall decrease in cluster formation due to heating of the analyte molecules. Thus, clustering behaviour trends are expected to move towards more positive CVs, or Type C

behaviour, as temperature is increased. This anticipated behaviour is observed for $B_{12}X_{12}^{2-}$ (X = H, F) in Figure 3.4 and Figure 3.5. All dispersion plots show a trend towards more positive CVs and lower SV at CV_{min} as temperature is increased. Unlike the protic modifiers, ACE and ACN resulted in more subtle differences between the three temperature studies owing to the fact that the CV turnaround point is (anticipated to be) off the measurable SV scale. It is also worth noting that for temperature studies in the pure N_2 environment, the Type C ion peak observed for $B_{12}H_{12}^{2-}$ disappears at lower SV with increasing temperature, further supporting the hypothesis that this additional feature is associated with a larger $B_{12}H_{12}^{2-}$-containing cluster.

Looking at the specific CV values for both $B_{12}H_{12}^{2-}$ and $B_{12}F_{12}^{2-}$ under different modifier conditions, it is seen that very large negative CVs are required for high SVs. For context, CV values for most analytes typically reach values of approximately −30 V, while those for $B_{12}H_{12}^{2-}$ and $B_{12}F_{12}^{2-}$ in the ACE- and ACN-modified environments approached −90 V at SV = 4000 V. Since DMS measures mobility differences between high and low field conditions, a CV value of −90 V indicates a large field-dependent change in ion mobility for the aprotic solvents. Table 3.3 shows the trend of the dipole moments compared to the trend in CV_{min}. The general trend of CV_{min} aligns well with the dipole moment trend, however, within the protic solvents there is a discrepancy. In particular, the behaviour in the H_2O-modified environment deviates from expectation, exhibiting weaker interactions than anticipated.

Table 3.3. The calculated dipole moments of each solvent molecule seeded in the DMS at 1.5% of the curtain gas compared with experimental CV_{min} for $B_{12}H_{12}^{2-}$ and $B_{12}F_{12}^{2-}$ unless stated otherwise.

Modifier	**Dipole Moment‡, $\|\vec{\mu}\|$ (*D*)**	**CV_{min} For $B_{12}H_{12}^{2-}$ At 300 ºC (V)**	**CV_{min} For $B_{12}F_{12}^{2-}$ At 300 ºC (V)**
N_2	0	−19.8	−5.4
Isopropyl Alcohol	1.58	−25.7	−29.3
Methanol	1.70	−30.9	−10.7
Water	1.86	−26.4	−7.9
Acetone	2.88	−75.1*	−65.3*
Acetonitrile	3.92	−92.5*	−82.5*

‡ Dipole moment values are taken from the NIST database.[38]
* These values are taken from predictions using the fitting function.

The high (I_h) symmetry of $B_{12}X_{12}^{2-}$ (X = H, F) and its central delocalized negative charge result in multiple binding sites for solvent molecules. For the $B_{12}H_{12}^{2-}\cdots H_2O$ case, the computational investigation of the single solvent molecule showed that the water molecule binds along the edge of the icosahedral structure which allows us to deduce that there are 30 potential binding sites available. Therefore, it is possible that many solvent molecules can bind at low field, resulting in solvation shells forming around the dianion. These solvent molecules desorb at high field, resulting in an exaggerated mobility change owing to the large change in apparent collision cross section (CCS).

It is useful at this point to summarize the observed DMS behaviour for $B_{12}H_{12}^{2-}$ and $B_{12}F_{12}^{2-}$. Referring to Figure 3.4, 3.5, and Table 3.2, 3.3 it is evident that charge-dipole interaction

dominates the observed clustering behaviour. The main exception is the behaviour of water, which exhibits a weaker clustering behaviour relative to its dipole moment, both regarding CV_{min} and SV at CV_{min}. It is important to keep in mind that the dispersion curves are mainly a depiction of the difference in mobility under a dynamic electric field. While the strength of binding will largely affect this differential mobility, size effects also factor into the observed behaviour. Water-containing clusters may exhibit more subtle differences in mobility under dynamic field conditions than do those containing IPA or MeOH owing to the fact that H_2O might form geometrically smaller species due to its relative size and weaker ion-solvent interactions. To investigate $B_{12}H_{12}^{2-}$ and $B_{12}F_{12}^{2-}$ solvent interactions more deeply, we turn to quantum chemical calculations.

3.3.2 Computational results

To investigate solvent interactions with $B_{12}X_{12}^{2-}$ (X = H, F, Cl, Br, I), electronic structure calculations were conducted. Figure 3.6 shows the geometrically optimized structures of binary clusters containing $B_{12}H_{12}^{2-}$ and N_2, H_2O, MeOH, IPA, ACN, and ACE. In cases other than N_2 (which does not exhibit a dipole moment), the solvent molecule generally orients to maximize the interaction with the dianion via the site with highest partial positive charge. In the cases of H_2O, ACE, and ACN, the optimized cluster clearly adopts a geometry that is indicative of charge – dipole interaction. However, in the cases of MeOH and IPA there appears to be an additional orientational effect due to hydrogen bonding. Similar structures are observed for the global minima of binary solvent clusters that contain $B_{12}X_{12}^{2-}$ (X = F, Cl, Br, I) (see Appendix A.1).

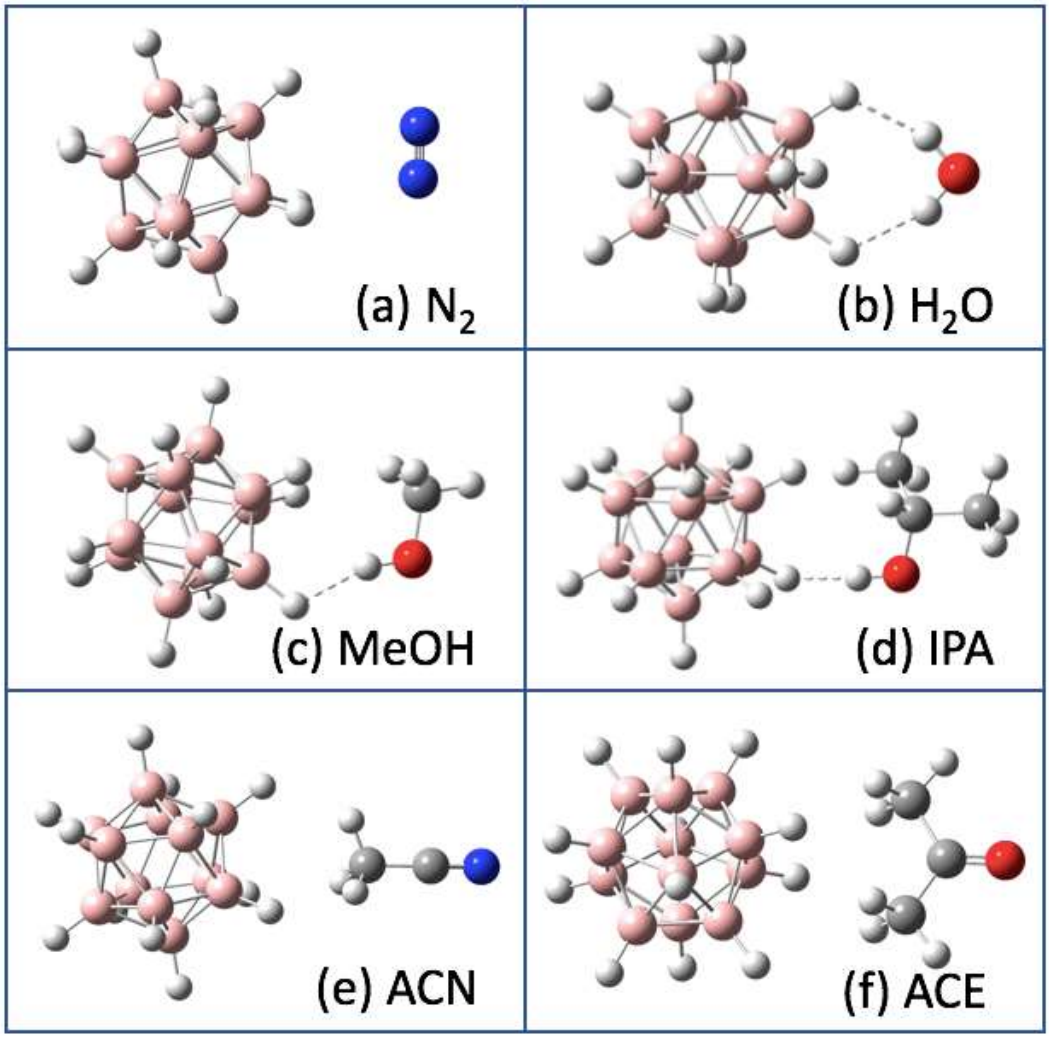

Figure 3.6. Optimized geometries of $B_{12}H_{12}^{2-}$ and solvent molecules as determined by DFT calculations. Note the orientation taken by all the solvent molecules besides N_2 that allow for the formation of charge-dipole interactions.

In the case of $B_{12}H_{12}^{2-}$, the molecular size is relatively small and most of the electron density is located on the surface of the cage. This is supported by partial charge calculations which show that the H atoms of $B_{12}H_{12}^{2-}$ have a cumulative charge of $\sum q_H$ = -2.93, whereas the boron framework exhibits a partial charge of $\sum q_B$ = +0.93 (see Figure 3.7). As the molecular size increases with successive halogen substitution (going from F to I), the concomitant drop in electronegativity of the halogen results in an increasingly negatively charged boron framework and positively charged halogen outer shell (see Figure 3.7). Consequently, the distance between the negatively charged region of the $B_{12}X_{12}^{2-}$ dianion and the solvent moiety increases as X

progresses from F to I (see Figure 3.8), and a decrease in ion-solvent binding energy is observed (see Table 3.4).

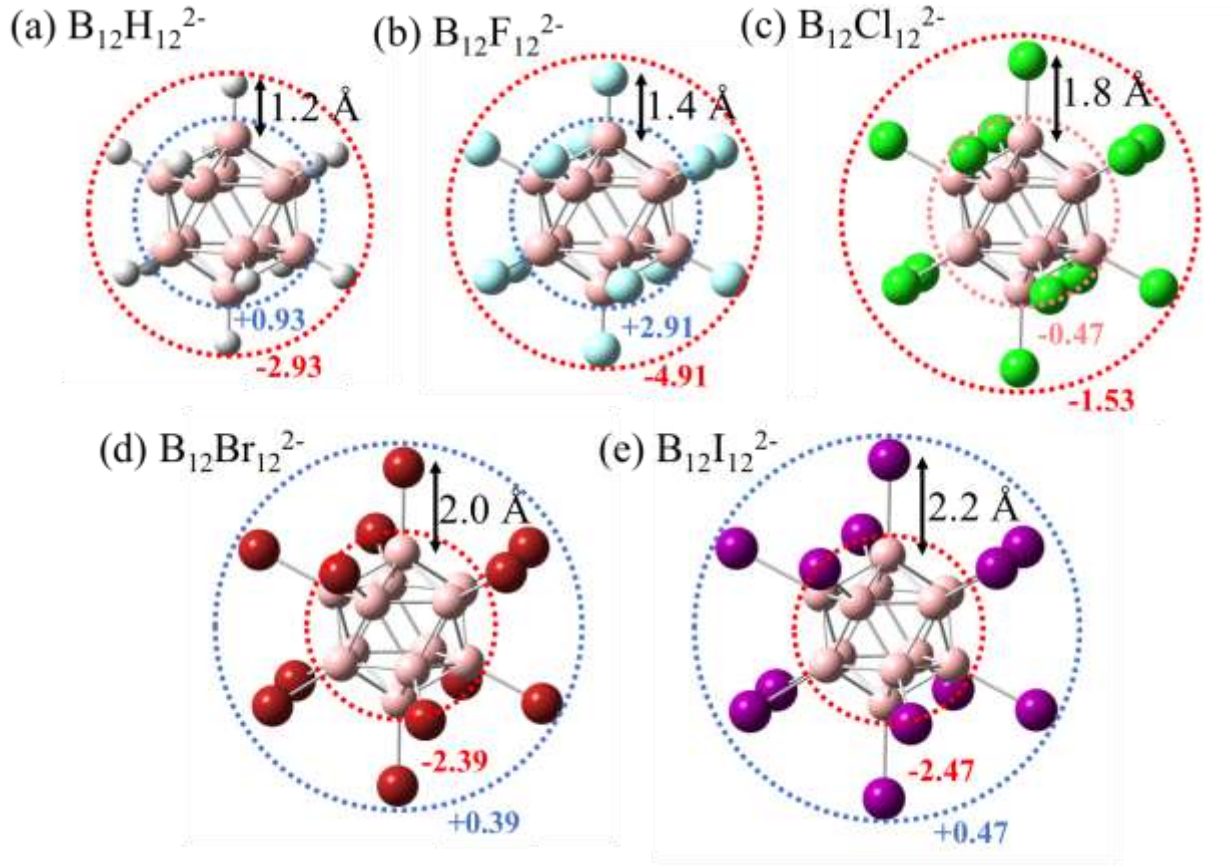

Figure 3.7. Charge distribution of $B_{12}X_{12}^{2-}$ (X = H – I), (a) - (e) respectively. Generally, the outer shell of the $B_{12}X_{12}^{2-}$ gets relatively more electropositive with respect to the inner boron cage. The bond length between boron and X increases from X = H to I.

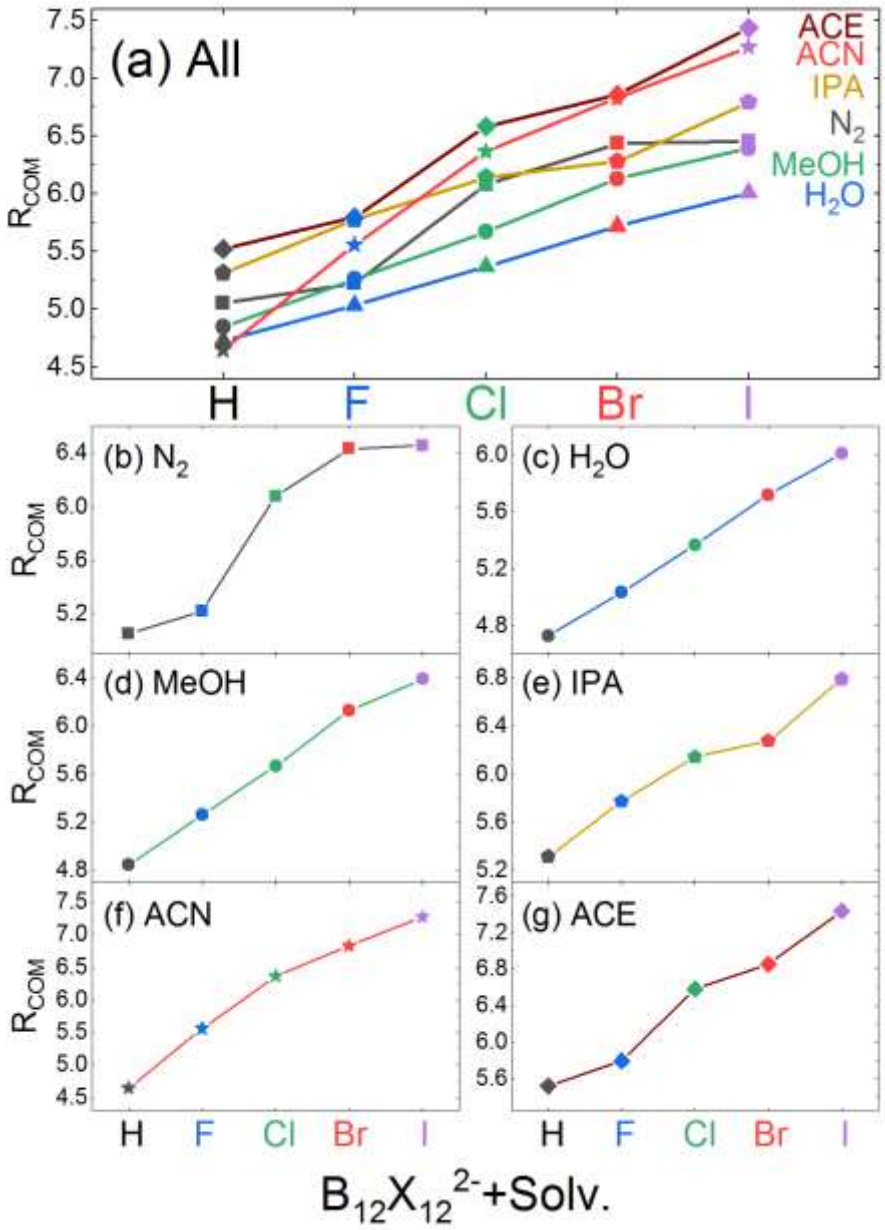

Figure 3.8. (a) The computed radii of all clusters formed between each $B_{12}X_{12}^{2-}$ sample and various solvent molecules. (b-g) The radii of the clusters formed between the $B_{12}X_{12}^{2-}$ samples for the individual solvents. As expected, the radii of the clusters increase with the increasing size of the $B_{12}X_{12}^{2-}$ moiety.

Using the optimized cluster geometries, one can employ Equations 3.4 and 3.6 to estimate the charge-dipole (and in the case of N_2, charge-quadrupole) interaction energies. The angle, θ, is simply determined from R_{COM} and $\vec{\mu}$. Electrostatic interaction energies for all solvents are tabulated in Table 3.4. The magnitude of the electrostatic interaction energies between the dianion and solvent molecules increases, in general agreement with the expected dipole moment trend.

The interaction of ACN and ACE with $B_{12}H_{12}^{2-}$ is, however, and exception to the anticipated trend; this is due to the fact that ACN is more closely bound to $B_{12}H_{12}^{2-}$ than is ACE as shown in Figure 3.8 (a) (*i.e.,* shorter R_{CoM}, so higher interaction energy). Interestingly, IPA exhibits somewhat anomalous behaviour. Inspection of the $[IPA{\bullet}B_{12}X_{12}]^{2-}$ structures shows that solvent binding occurs such that the R_{CoM} is not parallel to the molecular dipole axis (as mentioned above). This results in relatively small charge-dipole interaction energies for IPA-containing species (see Table 3.4). This lends support to the hypothesis that IPA binding is predominantly associated with H-bonding interactions.

Table 3.4. Electrostatic energy for clusters formed between the $B_{12}X_{12}^{2-}$ and various solvent molecules. All values are in kJ/mol.

	$E_{q\Theta}$ (kJ/mol)	$E_{q\mu}$ (kJ/mol)				
Species	N_2	H_2O	MeOH	IPA	ACN	ACE
$B_{12}H_{12}^{2-}$	−3.4	−67.5	−47.9	−29.8	−107.3	−117.0
$B_{12}F_{12}^{2-}$	−3.1	−51.0	−37.1	−17.7	−75.1	−72.6
$B_{12}Cl_{12}^{2-}$	−1.9	−39.9	−29.7	−17.4	−57.2	−49.7
$B_{12}Br_{12}^{2-}$	−1.6	−35.4	−24.1	−16.5	−49.7	−41.4
$B_{12}I_{12}^{2-}$	−1.6	−31.1	−22.2	−19.1	−43.8	−33.8

The Gibbs free energy of binding can be computed following normal mode analysis of the clusters. Assuming a binding reaction of $B_{12}X_{12}^{2-} + Solv \rightarrow [Solv{\bullet}B_{12}X_{12}]^{2-}$:[10]

$$\Delta G_{binding} = G_{[Solv\bullet B_{12}X_{12}^{2-}]} - G_{B_{12}X_{12}^{2-}} - G_{Solvent} \tag{3.7}$$

The calculated $\Delta G_{binding}$ for $B_{12}X_{12}^{2-}$ (X = H, F, Cl, Br, I) at room temperature and at each of the experimental temperatures (150 ºC, 225 ºC, and 300 ºC) is provided in Table 3.5 and Figure 3.9.

Contrary to what is observed experimentally for $B_{12}H_{12}^{2-}$ and $B_{12}F_{12}^{2-}$, calculations predict spontaneous dissociation of clusters containing $B_{12}X_{12}^{2-}$ and N_2 for all X. It is not surprising that binding with N_2 is not a spontaneous reaction, due to its very weak charge-quadrupole interaction. This may indicate the need to add more dispersive functions to describe $B_{12}X_{12}^{2-}$•N_2, and anharmonic corrections are necessary to improve calculation accuracy. Nevertheless, the anticipated binding trends are observed in calculation results; spontaneous formation of $[Solv•B_{12}X_{12}]^{2-}$ (X = H – I) clusters is predicted at room temperature, with decreasing spontaneity of formation as temperature is increased.

Table 3.5. Gibbs energy of binding for the clusters formed between the $B_{12}X_{12}^{2-}$ and various solvent molecules at different temperatures. Gibbs energy is given in kJ/mol.

Species	Temperature (°C)	N_2	H_2O	MeOH	IPA	ACN	ACE
$B_{12}H_{12}^{2-}$	25	15.6	−23.5	−18.5	−22.1	−39.4	−28.1
	150	25.3	−9.4	−3.8	−6.4	−26.0	−12.3
	225	30.9	−1.1	4.8	2.7	−18.2	−3.1
	300	36.4	7.0	13.2	11.8	−10.7	5.9
$B_{12}F_{12}^{2-}$	25	9.4	−19.3	−11.8	−15.1	−31.9	−18.9
	150	16.2	−5.0	3.4	1.1	−16.5	−0.7
	225	20.0	3.3	12.2	10.5	−7.6	9.9
	300	23.7	11.5	20.9	19.8	1.2	20.4
$B_{12}Cl_{12}^{2-}$	25	15.7	−13.8	−5.5	−7.15	−25.6	−13.1
	150	25.0	−1.2	10.0	10.2	−11.8	3.8
	225	30.3	6.1	19.0	20.3	−3.9	13.6
	300	35.4	13.2	27.9	30.2	3.8	23.2
$B_{12}Br_{12}^{2-}$	25	16.4	−11.4	−3.1	−4.5	−20.9	−9.1
	150	25.7	1.1	12.5	12.9	−6.8	7.9
	225	31.0	8.3	21.6	23.0	1.3	17.8
	300	36.3	15.4	30.5	33.0	9.3	27.5
$B_{12}I_{12}^{2-}$	25	17.2	−4.4	−0.1	−1.6	−17.0	−5.2
	150	26.5	10.9	15.6	15.5	-3.4	11.5
	225	31.8	20.0	24.7	25.5	4.5	21.3
	300	37.0	29.0	33.6	35.3	12.2	30.8

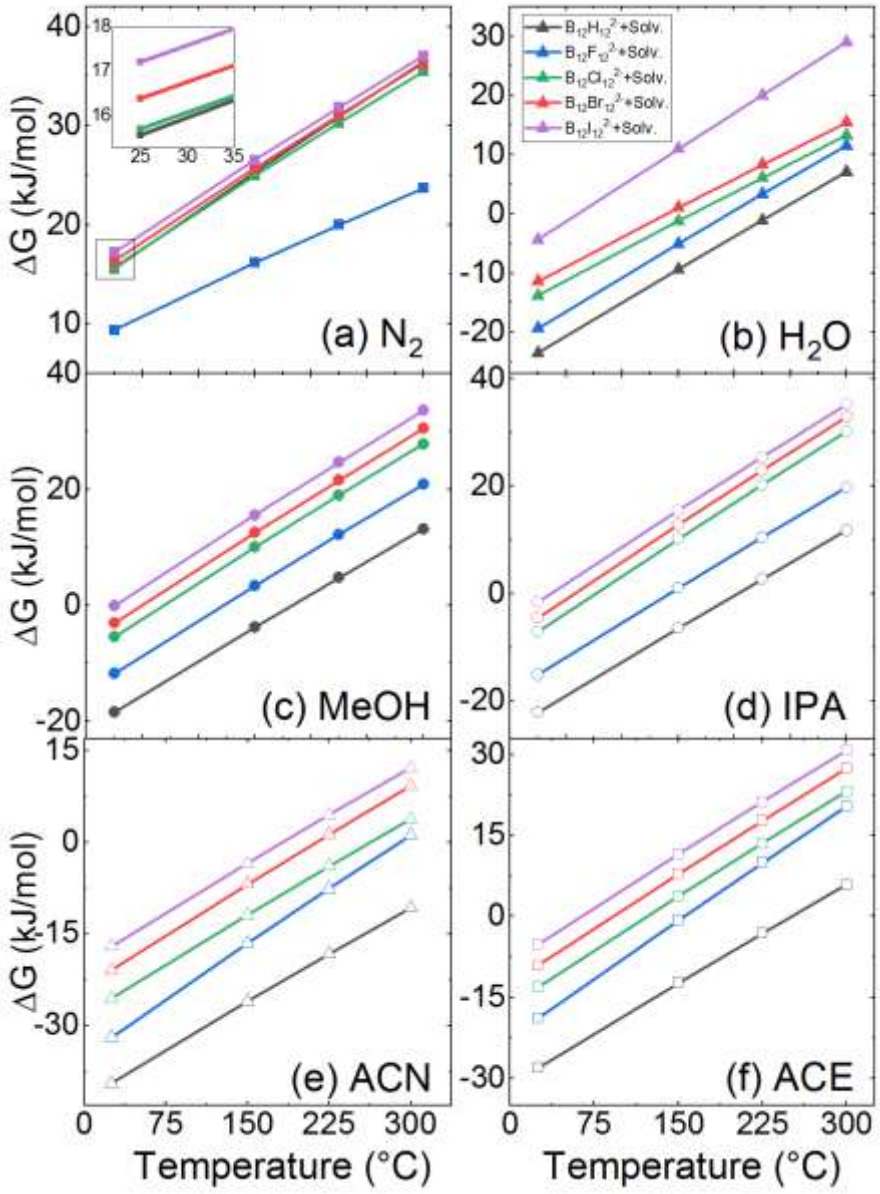

Figure 3.9. The Gibbs energies of binding as a function of temperature for $B_{12}X_{12}^{2-}$ (X = H – I) in N_2 (a) and all solvents. (b-g). The relationship between Gibbs energy, temperature, and $B_{12}X_{12}^{2-}$ moiety is displayed individually for each solvent molecule.

Figure 3.10 plots the correlation between the calculated binding energy and the SV at CV_{min} for $B_{12}H_{12}^{2-}$ and $B_{12}F_{12}^{2-}$ in the various DMS environments. The linear trends observed for other, smaller singly charged systems is not reproduced in the case of $B_{12}X_{12}^{2-}$ (X = H, F). There are three major sources of error that could explain this discrepancy. First, it is unlikely that the clustering of $B_{12}X_{12}^{2-}$ (X = H, F) can be reasonably modeled/represented with a single solvent

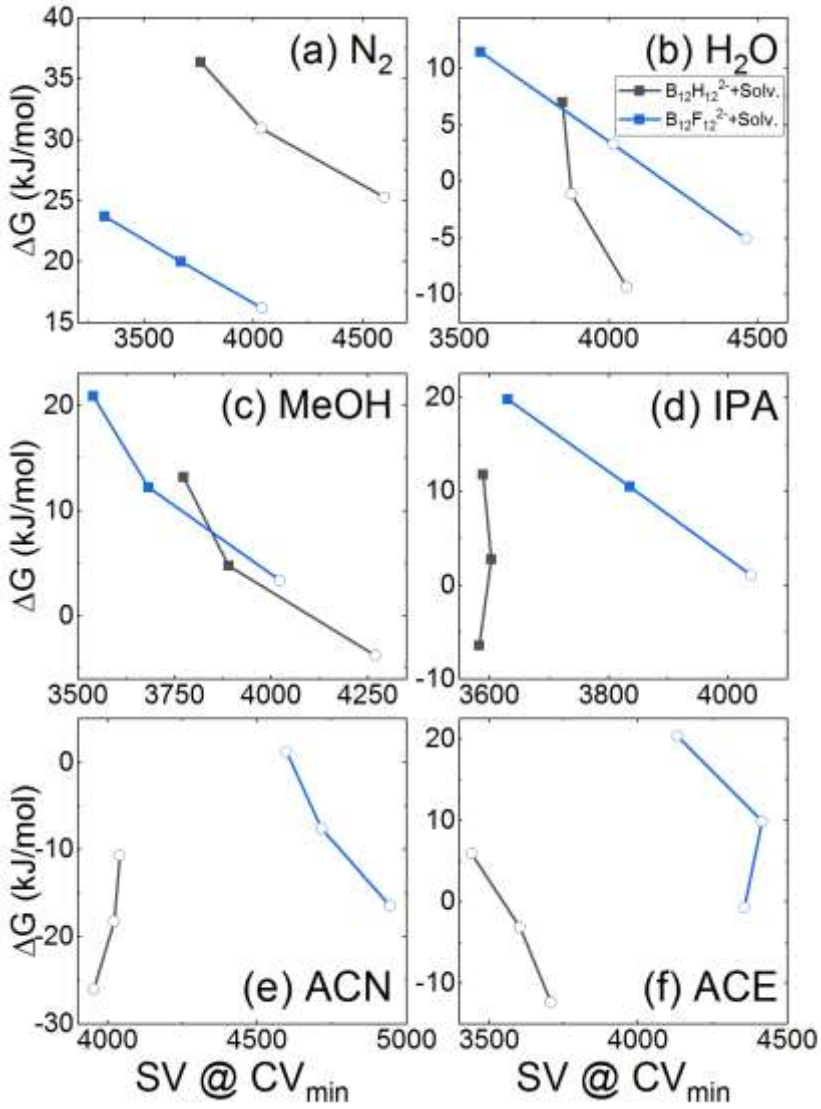

Figure 3.10. (a-f) The Gibbs binding energies for the different clusters, $B_{12}H_{12}^{2-}$ (black) and $B_{12}F_{12}^{2-}$ (blue) compared to the SV at CV_{min} values determined experimentally. Open circle markers indicate extrapolated SV values using the fitting function from Equation 3.2.

molecule. Second, the accuracy of calculations of ion-solvent interactions could be improved by introducing anharmonic corrections. Third, many of the SV at CV_{min} data points are extrapolated from the measured data; this is expected to be progressively worse as the SV at CV_{min} moves farther out of the measured range. It may be useful to consider the clustering when determining solvent effect on solvent binding energies of the dianion. A recent study by Walker *et al.* improved

accuracy by employing machine learning to correlate the entire dispersion curves to the computed binding energy.[39]

3.4 Conclusion

The DMS behaviour of $B_{12}X_{12}^{2-}$ (X = H, F) was studied in a variety of environments at temperatures of 150 °C, 225 °C, and 300 °C. In general, we find that the observed clustering behaviour can be rationalized in terms of electrostatic interactions between the dianion and the solvent molecules. However, in the case of protic modifiers, there seem to be significant contributions from hydrogen bonding; this seems to be particularly important in the case of IPA. Calculated charge-dipole interactions decrease with increasing halogen size owing to the increased separation between moieties. The anticipated (and well documented) correlation between calculated ion-solvent binding energy and SV at CV_{min} was not observed for $B_{12}X_{12}^{2-}$ (X = H, F). This can likely be attributed to the fact that these dianion species have multiple equivalent sites for solvent interaction. Consequently, large solvation shells are likely to form, resulting in large CCS (*i.e.*, mobility) differences under the dynamic electric field conditions of the DMS cell. This physical scenario is not likely to be well-modelled by binary analyte-solvent clusters. Nevertheless, DFT calculations were conducted to investigate the observed phenomena. It was found that clustering reactions become less favourable under increasing temperature conditions and with decreasing dipole moment of the solvent moiety. For the most part, optimize cluster structures adopted geometries as would be expected for species bound by electrostatic interactions. However, in the case of MeOH and IPA, solvent orientations were indicative of additional hydrogen bonding interactions.

Chapter 4. $B_{12}X_{12}^{2-}$ Photoelectron Spectra

4.1 Introduction to PES

Strong Coulombic repulsive forces dictate the relative stability of multiply charged anion (MCA) species.[13] In general this leads to instability in the gas phase, e.g. SO_4^{2-} and HPO_4^{2-};[1,3,16,40] these species typically undergo spontaneous electron detachment in the gas phase,[13] which motivates the search for stable gas-phase MCAs. Boron cage species, such as $B_{12}X_{12}^{2-}$ (X= H, F, Cl, Br, I), are prominent MCAs, popularized due to their relative stability unlike SO_4^{2-} and HPO_4^{2-}.[1,3,16,40] To better understand $B_{12}X_{12}^{2-}$, PES studies will be conducted on $B_{12}X_{12}^{2-}$ to investigate the role of geometric and electronic structure on anion stability. In addition, density functional theory (DFT) calculations are performed using the quantum chemical software package Gaussian 16 in order to assign the experimentally observed PES and provide a simple visualization of the electronic states for $B_{12}X_{12}^{2-}$ (X = H, F, Cl, Br, I).[24]

In PES, a sample is interrogated with photons of a known frequency to induce electron detachment[15]. The kinetic energy of the detached electron is measured and used to determine the electron binding energy (*i.e.,* ionization energy),[15] as shown in Figure 4.1. The electron binding energy provides information on ionization thresholds and through comparison with calculations can be used to elucidate the characteristics of electronic states.[15]

The PES for $B_{12}X_{12}^{2-}$ can be estimated by comparing the simulated spectrum with the experimental PES allows assignment of the specific vibronic transitions which give rise to the observed spectrum. In Figure 4.1 is shown a few example electron detachment transitions for excitation of ground state $B_{12}X_{12}^{2-}$ (v = 0) to two different electronic states of the anion, $B_{12}X_{12}^{-}$, and different vibrational states. Figure 4.1 also provides a pictorial representation of PES, in which

the energy of the incoming photon, *hv*, is distributed between the measured electron kinetic energy (eKE) and the internal energy of the anion, $B_{12}X_{12}^-$.

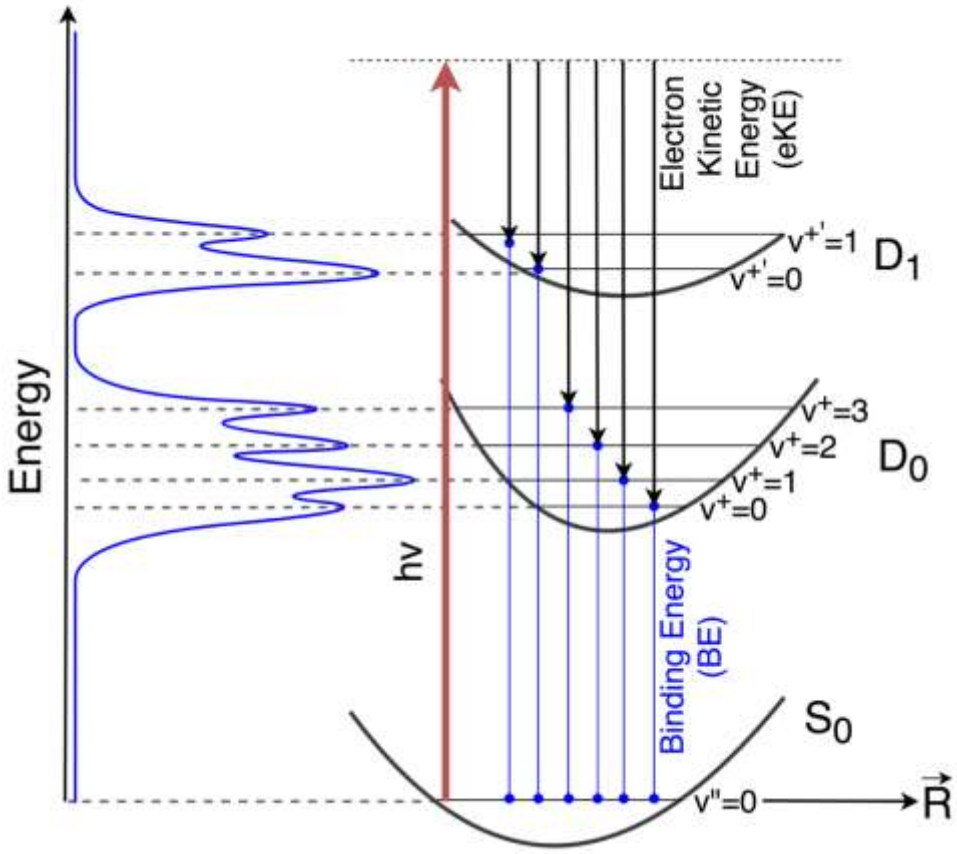

Figure 4.1. A diagram of a hypothetical PES which illustrates the connection between the electron detachment vibronic transitions with the observed PES through the measured electron kinetic energy. Transitions between the ground $B_{12}X_{12}^{2-}$ singlet electronic state (S_0) to the two lowest doublet states of $B_{12}X_{12}^-$ (D_0 and D_1) are shown in blue. The anion lies higher in energy and its structure is distorted as indicated by the shift in the doublet states relative to the dianion singlet state along an internal coordinate, $\vec{R}$.

One significant factor dictating relative stability in MCAs is the presence of an RCB.[13] The magnitude of the RCB is affected by the geometric size of $B_{12}X_{12}^{2-}$.[41] In general, as charge separation increases, RCBs decrease with the increase in stability of the MCA.[41] A depiction of the effect of charge separation on RCBs is shown in Figure 4.2 for the case of $B_{12}H_{12}^{2-}$ and $B_{12}I_{12}^{2-}$, in which D is used to indicate the cage diameter in each case. Note that the RCB is measured with respect to the separated $B_{12}X_{12}^-$ and e^- and so represents the barrier to electron association to form the dianion.

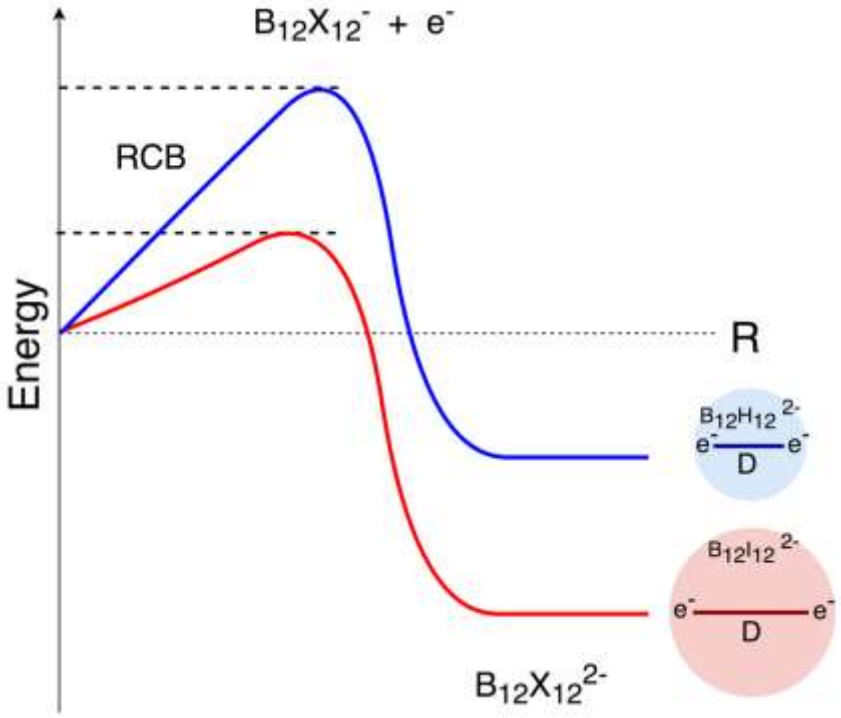

Figure 4.2. Energy diagram for $B_{12}X_{12}^-$ electron association to form $B_{12}X_{12}^{2-}$. Energy is shown with respect to infinite separation of the electron and anion. As the $B_{12}X_{12}^-$—e^- separation (D) decreases repulsive coulomb interactions dominate giving rise to an RCB. As molecular size increases, as depicted by D, the charge separation increases stabilizing the dianion and decreasing the RCB.

Upon photodetachment from $B_{12}X_{12}^{2-}$ a change in multiplicity occurs (singlet → doublet) and Jahn-Teller distortion induces a change in geometry.[42] This results in electronic state splitting for the previously degenerate $B_{12}X_{12}^{2-}$ HOMO, shown in Figure 4.3.[13]

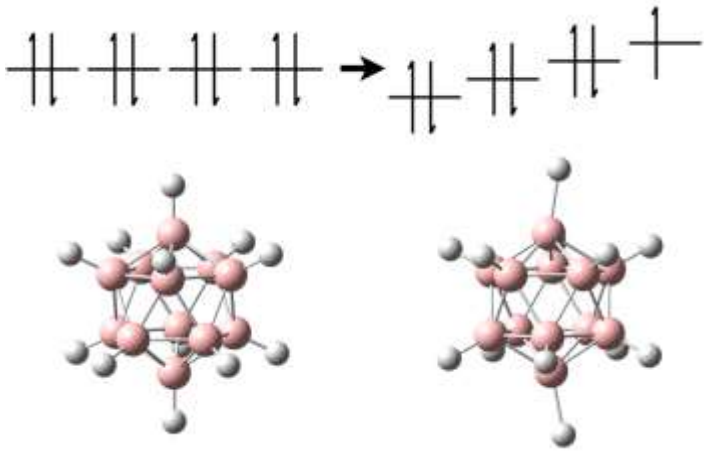

Figure 4.3. Jahn-Teller distortion as seen in the four highest occupied states of $B_{12}H_{12}^{2-}$ in comparison to the degenerate HOMO of $B_{12}H_{12}^{2-}$. The four-fold degenerate $B_{12}H_{12}^{2-}$ state becomes four singly degenerate states as a result of the distortion. Note that the geometry change is exaggerated to highlight the distortion.

4.2 Methods

A general description of the combined theoretical calculations and experimental methods used to study the electronic and geometric structures of $B_{12}X_{12}^{2-}$ (X = H, F, Cl, Br, I) can be found in section 2.3. Further details are provided below.

4.2.1 Photoelectron spectroscopy

PES for $B_{12}X_{12}^{2-}$ (X = F, Cl, Br, I) are reported in reference 13, and spectra for $B_{12}H_{12}^{2-}$ are reported in reference 14. For experiments involving $B_{12}H_{12}^{2-}$, a $K_2B_{12}H_{12}$ sample was prepared in methanolic solution,[14] whereas the rest of the derivatives (X = F, Cl, Br, I) were prepared in ACN and tetrabutylammonium (TBA) under a N_2 atmosphere.[13]

PES experiments were performed using a magnetic bottle time-of-flight (TOF) photoelectron spectrometer coupled with a temperature-controlled cryogenic ion trap.[43] A Nd:YAG-pumped, Quanta-Ray MOPO-730 OPO, and a F_2 excimer laser operated at 20 Hz to produce 266 nm (4.661 eV), 225 nm (5.510 eV), or 157 nm (7.866 eV) were used for sample irradiation.[13,14] A magnetic bottle collected the photoelectrons with 100% efficiency, which were then analysed in a 5.2 m long TOF.[13,14,43]

An ESI source was used to ionize the sample. ESI is a soft ionization source which should maintain the structural integrity of the samples.[43] Once ionized by the ESI source, samples were accumulated into the ion trap for 20-100 ms, where they were cooled *via* collisions with buffer gas composed of 20% H_2 and 80% He at 20 K.[13,14,43] Low temperatures improve spectral resolution and reduce any peaks due to hot bands.[13] The species of interest were mass-selected in the TOF mass spectrometer and decelerated for photo detachment experiments.[43]

Previously recorded PES of I^- and $OsCl_6^-$ were used as energy calibration standards to convert the acquired photoelectron TOF spectra of $B_{12}X_{12}^{2-}$ samples into electron kinetic energy

spectra.[13,14] Electron detachment transitions, e.g. see Figure 4.1, are calculated by subtracting the measured electron kinetic energy from the photon energy of the probe laser.[15]

4.2.2 Computational Methods

All electronic structure calculations reported in this Chapter were performed at the B3LYP/Def2-TZVPP level of theory. In addition, time dependent density functional theory (TD-DFT) calculations were performed on $B_{12}X_{12}^{2-}$ species in order to calculate excited electronic state energies as indicated in Figure 4.4. The $B_{12}H_{12}^{-}$ ground electronic doublet state, D_0, lies 0.90 eV above the $B_{12}H_{12}^{2-}$ singlet state, S_0. The $S_0 \rightarrow S_1$ $B_{12}H_{12}^{2-}$ electronic transition energy is 4.47 eV which is higher than the $S_0 \rightarrow D_0$ transition energy. Similarly, for $B_{12}X_{12}^{2-}$ (X = F, Cl, Br, I). This means internal transitions for $B_{12}X_{12}^{2-}$ won't compete with the photoelectron detachment transition to form the anion, $B_{12}X_{12}^{-}$.

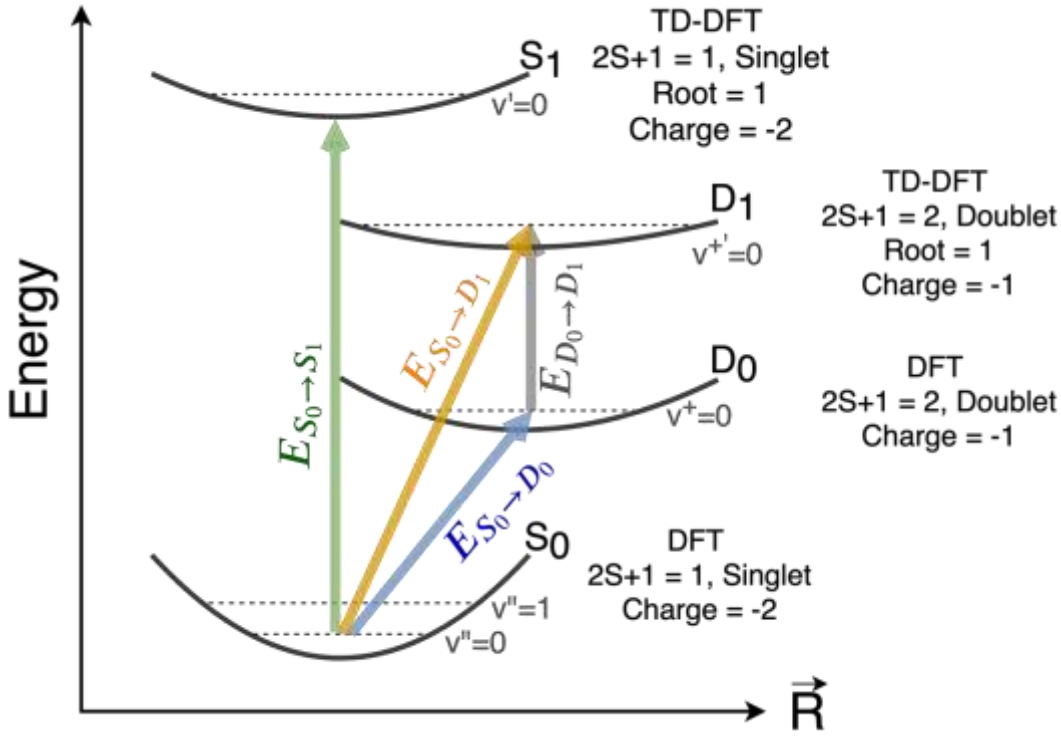

Figure 4.4. S_0 refers to singlet ground state of the dianion, D_0 refers to doublet ground state of the monoanion and D_1 is the first excited state of the monoanion. The $S_0 \rightarrow S_1$ transition of the dianion is much larger in energy.

Next, two possible pathways, ADE and VDE, of the dianion to the monoanion were calculated. ADE was calculated by first optimizing the dianion and monoanion geometries and comparing their energies. VDE, on the other hand, was calculated after optimizing the dianion geometry and preserving this geometry for the monoanion, such that no geometry distortions are induced between the two molecules. These transitions are shown in Figure 4.5.

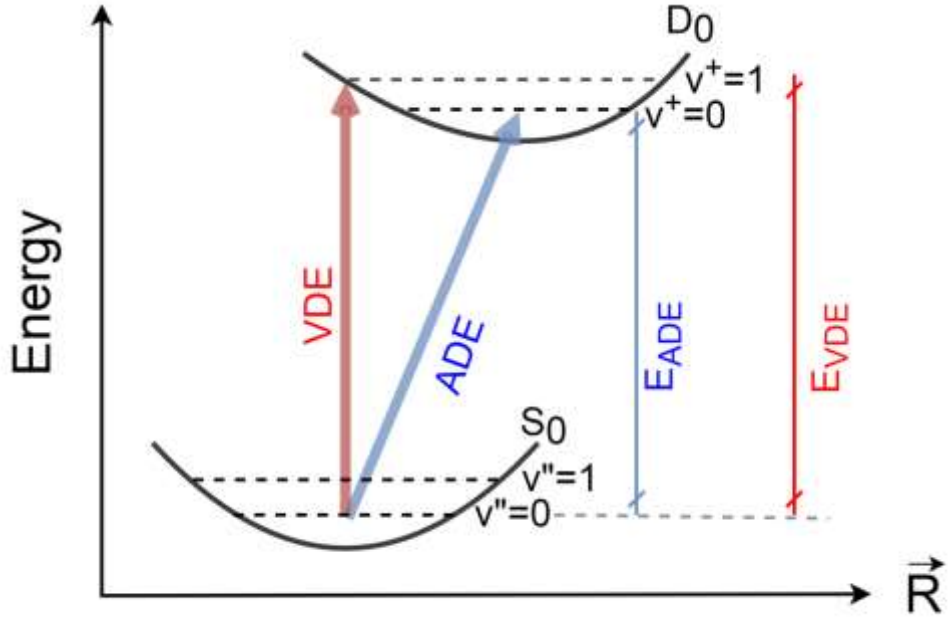

Figure 4.5. Comparison of the energy and conformational difference of the VDE and ADE transitions.

To compliment experimental studies of $B_{12}X_{12}^{2-}$ PES conducted by Warneke *et al.*,[13,14] theoretical spectra were modeled using the approach depicted in Figure 4.6. As a first approximation, the energy of the highest occupied molecular orbital (HOMO) in the monoanion is set to the observed ionization energy and subsequent levels are shifted accordingly (*i.e.*, HOMO-1, HOMO-2, etc). With this shift, the calculated D_0 (monoanion) energy is just the ionization energy, ($S_o \rightarrow D_0$), whereas the D_1 (monoanion) energy would correspond to the S_0 (dianion) $\rightarrow$ D_1 (anion) transition energy. An electronic stick spectrum can be generated from each of the shifted monoanion state energies for D_0, D_1, D_2, … etc. As an approximation,

a simple Gaussian broadening of 0.05 eV is used to introduce peak width. The resulting intensities of each PES peak are representative of the molecular density of states. result from the convolution with all electronic states given an intensity of 1.0. Ideally, vibrational broadening as well as transition intensities would be calculated *via* transition dipole moment integrals or more simply, FCFs. Refer to Section 2.4 for a detailed description of FCF. To improve simulation accuracy for the $S_0 \rightarrow D_0$ transitions, FCF calculations were conducted. TD-DFT calculations for higher excited anion states, are ongoing.

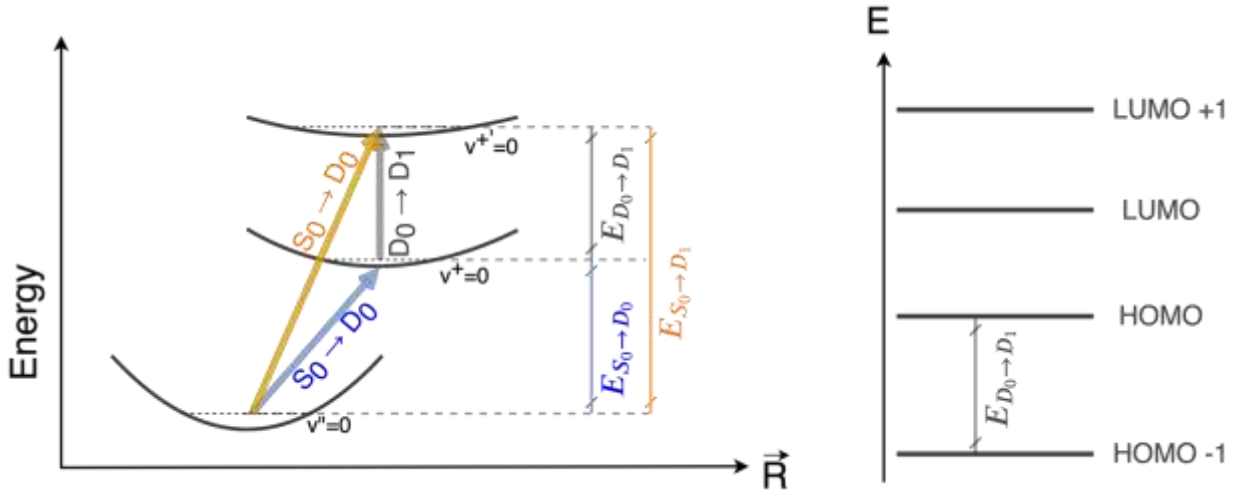

Figure 4.6. The energies of the various transitions can be related to the electronic states of the cages, in which the energy of the doublet ground state to the doublet first excited state transition can be related to that of the HOMO-1 to HOMO level transition.

4.3 Results and Discussion

The excitation energy between the ground state dianion singlet (S_0) and the first excited singlet (S_1) state was calculated using TD-DFT. By comparing this value with the calculated energy difference between the dianion ground state and the states for the monoanion, we could confirm that less energy is required for electron detachment to produce the monoanion than for the excitation to the first excited singlet state of the dianion, see Table 4.1. Both calculations were performed while preserving the optimized geometry of the dianion (*i.e.*, vertical energy transition).

The effect of geometry was also considered, to obtain a more well-rounded study on the energy transitions, ADE and VDE. Both processes were studied using TD-DFT and their results are tabulated in Table 4.2.

Table 4.1. Calculated energies of the first excited state transition and of the ionization of $B_{12}X_{12}^{2-}$.

X	$S_0 \rightarrow S_1$ Transition Energy (eV)	$S_0 \rightarrow D_0$ (VDE) Transition Energy (eV)
H	4.47	1.61
F	3.93	2.00
Cl	4.57	2.80
Br	4.19	3.12
I	3.09	2.31

Table 4.2. Calculated energies for the ADE and VDE transitions of $B_{12}X_{12}^{2-}$.

X	ADE Transition Energy (eV)	VDE Transition Energy (eV)	Δ(VDE-ADE) (eV)
H	0.90	1.61	0.71
F	1.64	2.0	0.40
Cl	2.59	2.80	0.22
Br	2.89	3.12	0.22
I	2.28	2.31	0.02

The differences between ADE and VDE values, see Table 4.2, are due to the geometry change upon ionization (arising from Jahn-Teller distortion).[42] As the identity of X in $B_{12}X_{12}^{2-}$ progresses from hydrogen to iodine the energy difference between ADE and VDE decreases. These results indicate that the geometry is not significantly affected by the change in electronic structure upon electron detachment for the larger cage.

The general increase in VDE and ADE values, as X progresses down the periodic table, can be rationalized by trends in the electronic structure. As the cage size increases with substitution, the system generally experiences greater stabilization for the HOMO states. However, $B_{12}I_{12}^{2-}$ does not follow this trend. This is explained by a consideration of MOs, as described by Warneke *et al.*[13] The HOMO in the $B_{12}X_{12}^{2-}$ for X = F, Cl, Br is boron-centered, whereas the HOMO in the iodine species is halogen-centered. This switch over leads to the observed deviation in IE trend.

All theoretical calculations were compared to the 157 nm wavelength experimental data from references. [13,14] The photoelectron stick spectra as simulated for in the two cases (ADE and VDE) for $B_{12}X_{12}^{2-}$ (X = H, F, Cl, Br, I) are shown in Figure 4.7, 4.8, 4.9, 4.10 and 4.11 respectively. As is clear from Figure 4.7 (b) and (c), the broadened stick spectra do not provide an accurate representation of the peak intensities nor the peak widths. Clearly the vibrational states for dianion and anion should be considered in the simulation to calculate peak widths and intensities via wavefunction overlap between states. To accomplish this, FCF values for each $B_{12}X_{12}$ derivative were simulated using Gaussian16.[24] The vibronic simulations for $B_{12}X_{12}^{2-}$ (X = H, F, Cl, Br, I) $S_0 \rightarrow D_0$ PES are shown in figures, Figure 4.7 (d) to Figure 4.11 (d) respectively.

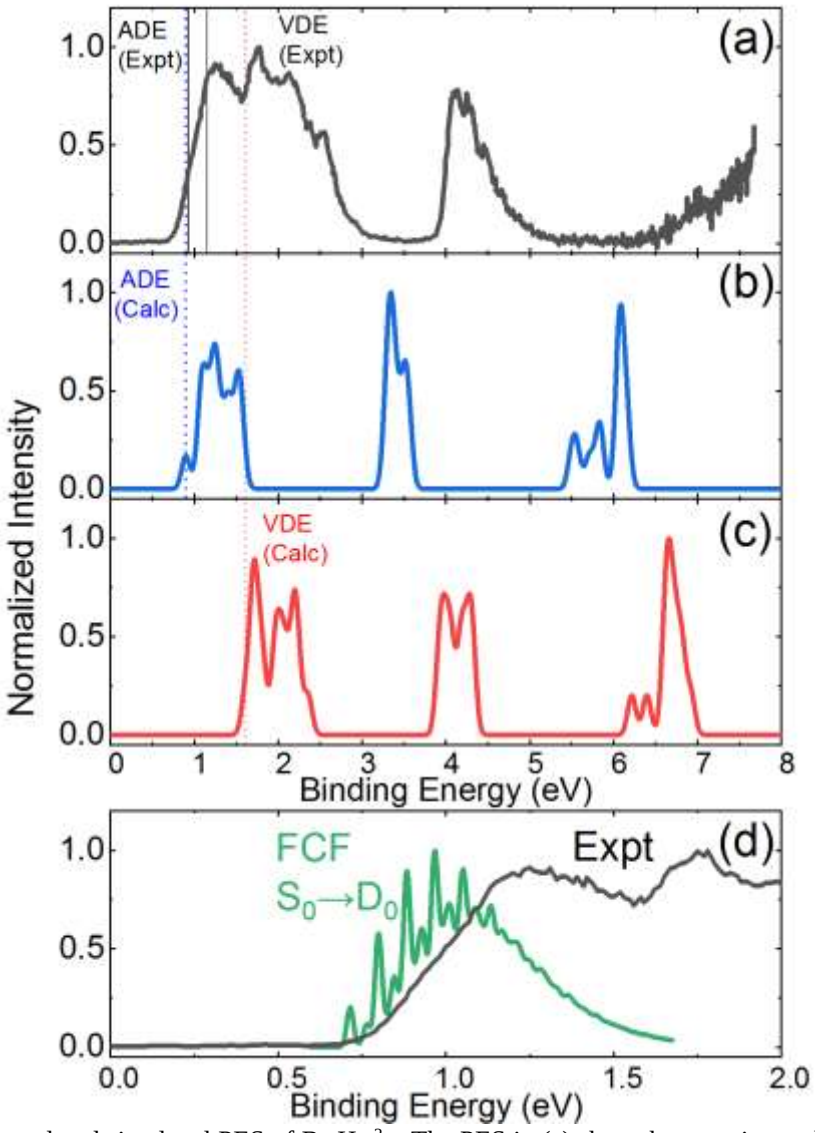

Figure 4.7. Experimental and simulated PES of $B_{12}H_{12}^{2-}$. The PES in (a) show the experimental PES obtained from reference [14]. (b) Calculated ADE PES using the B3LYP method could be compared to the calculated VDE PES (c). FCFs were also generated for the first excited state as shown in (d). The calculated ADE and VDE values are compared with those determined experimentally.

The experimental PES is shown in Figure 4.7 (a). The vibronic structure is washed out in the experiment due to the high density of states (DoS); individual vibronic transitions cannot be resolved experimentally. Comparing the PES experimental data, Figure 4.7 (a), to the FCF simulation, (d), the vibronic simulation does well with the onset. It is thus shown that the ADE calculation matches up nicely with the experimental data. The additional structure around 4 eV in Figure 4.7 (a) is evidently due to electronic states which is captured in Figure 4.7 (b) and (c).

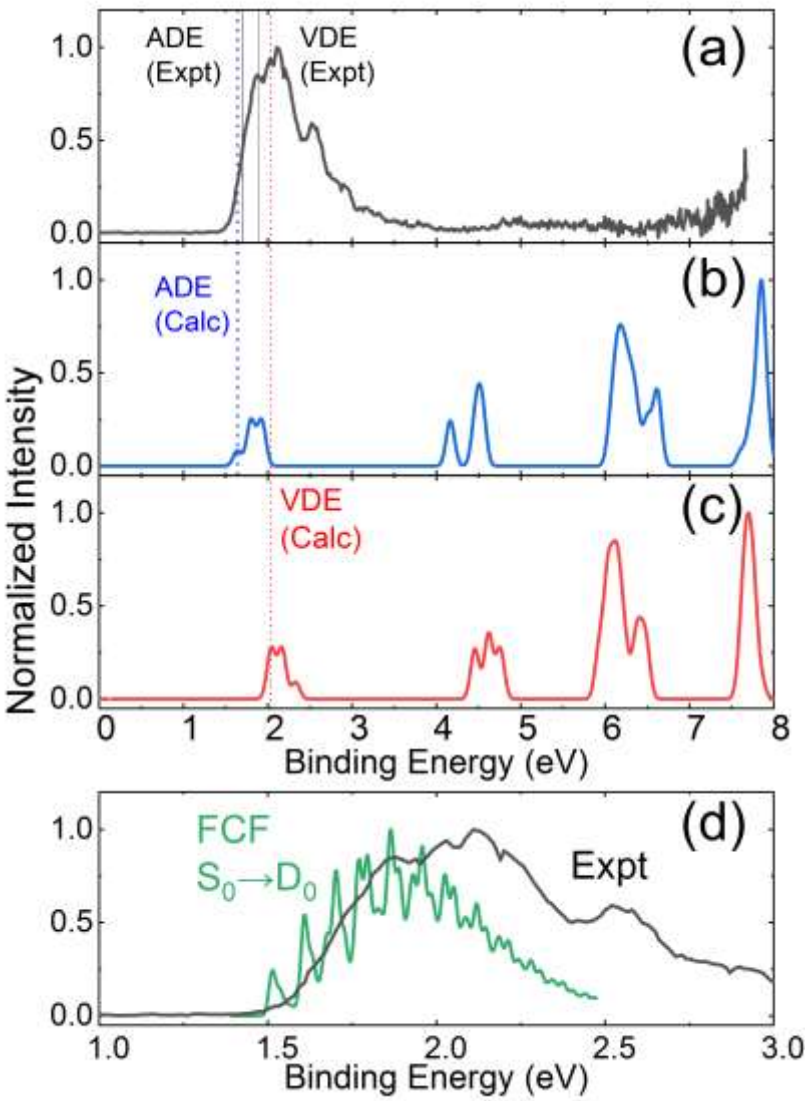

Figure 4.8. Experimental and simulated PES of $B_{12}F_{12}^{2-}$. The PES in (a) show the experimental PES obtained by Warneke *et al*.[13] (b) Calculated ADE PES using the B3LYP method could be compared to the calculated VDE PES (c). FCFs were also generated for the first excited state as shown in (d). The calculated ADE and VDE values are compared with those determined experimentally.

Compared to the $B_{12}H_{12}^{2-}$ DoS broadened stick spectra, the calculated spectra for $B_{12}F_{12}^{2-}$ are poorer; at higher energy and in terms of width/intensity of the peaks. However, the Franck Condon simulation in Figure 4.8 (d) shows excellent agreement with the experimental data. The calculated vibrational manifold correlates well with experiment and suggests that spectral structure in the experimental data is associated with vibronic states.

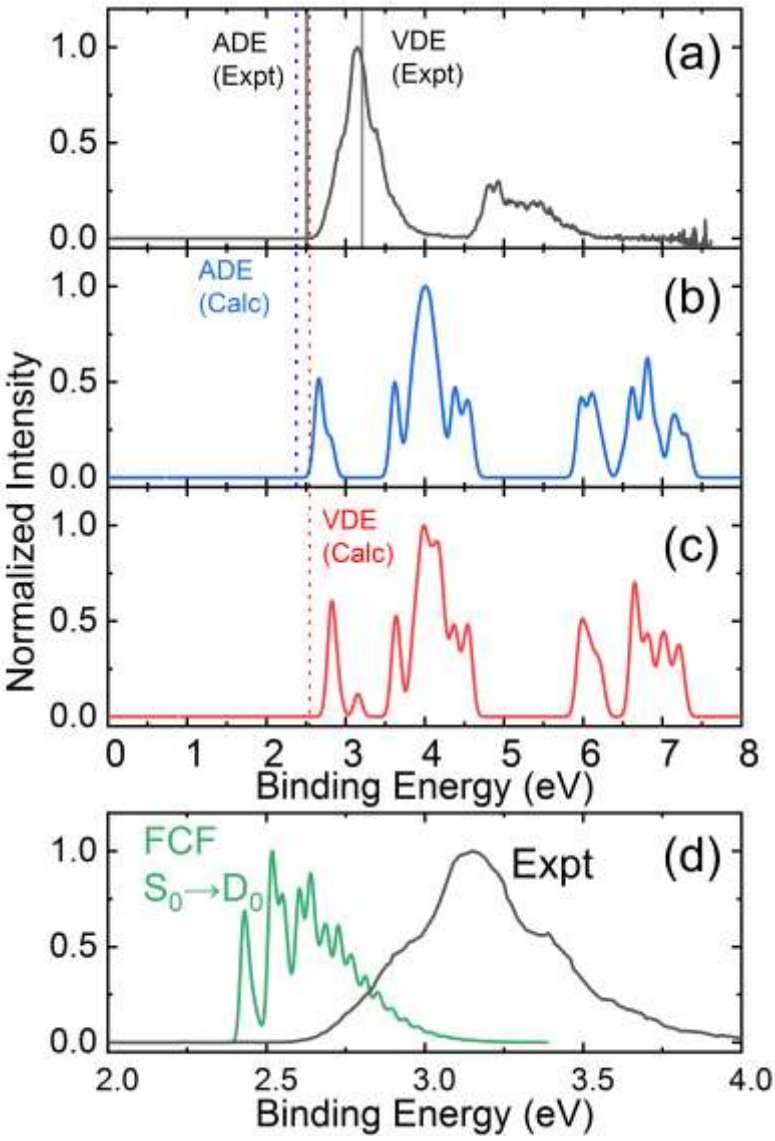

Figure 4.9. Experimental and simulated PES of $B_{12}Cl_{12}^{2-}$. The PES in (a) show the experimental PES obtained by Warneke *et al*.[13] (b) Calculated ADE PES using the B3LYP method could be compared to the calculated VDE PES (c). FCFs were also generated for the first excited state as shown in (d). The calculated ADE and VDE values are compared with those determined experimentally.

The calculated DoS spectra for $B_{12}X_{12}^{2-}$ (X = Cl, Br, I) are, in general, representative of the experimental data as shown in (b) and (c) for Figure 4.9, 4.10, 4.11. Interestingly though, the Franck Condon simulations are consistently red shifted relative to the experimental results. This may be indicating that the def2-TZVPP poorly represents the orbitals on the heavier halogen atoms, and thus the electronic structures of the heavier derivatives.

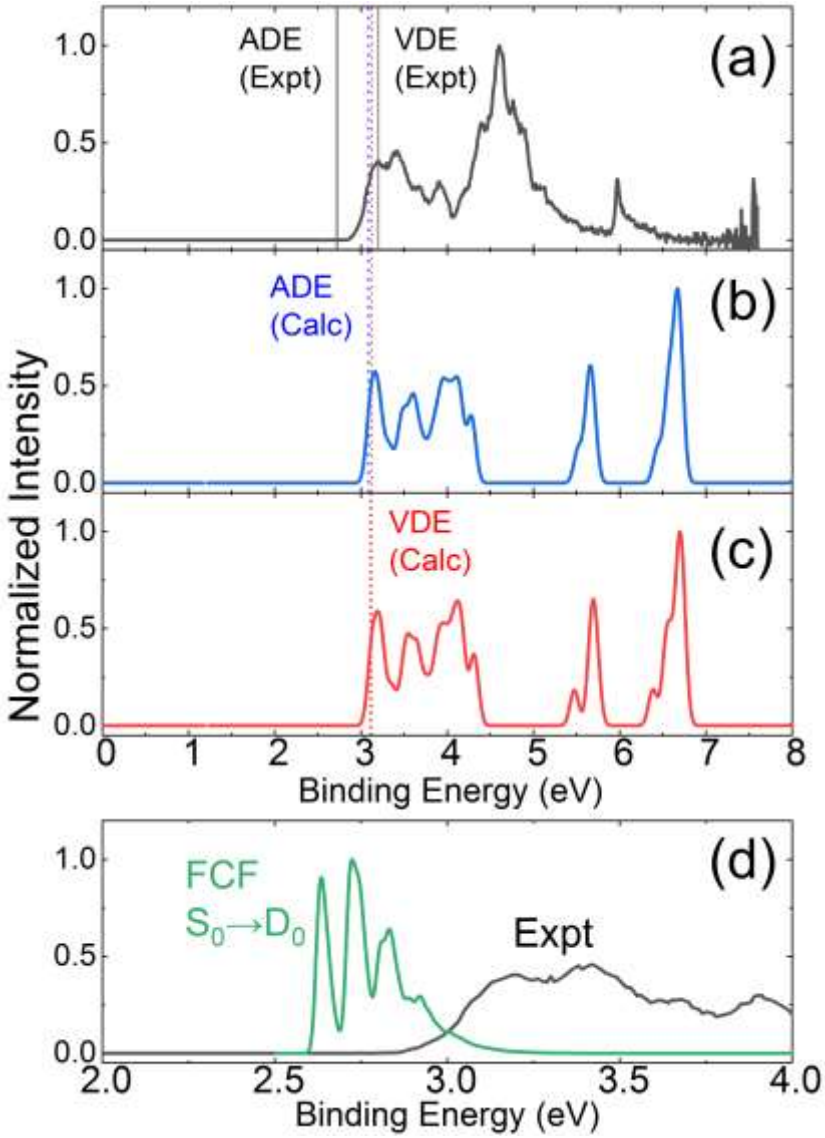

Figure 4.10. Experimental and simulated PES of $B_{12}Br_{12}^{2-}$. The PES in (a) show the experimental PES obtained by Warneke *et al*.[13] (b) Calculated ADE PES using the B3LYP method could be compared to the calculated VDE PES (c). FCFs were also generated for the first excited state as shown in (d). The calculated ADE and VDE values are compared with those determined experimentally.

From Figure 4.9 (d) to Figure 4.11 (d), it is important to note the collapse in the vibrational structures from Cl to I which is consistent with the trend of decrease in geometry distortion as the mass of X in $B_{12}X_{12}^{2-}$ gets heavier.

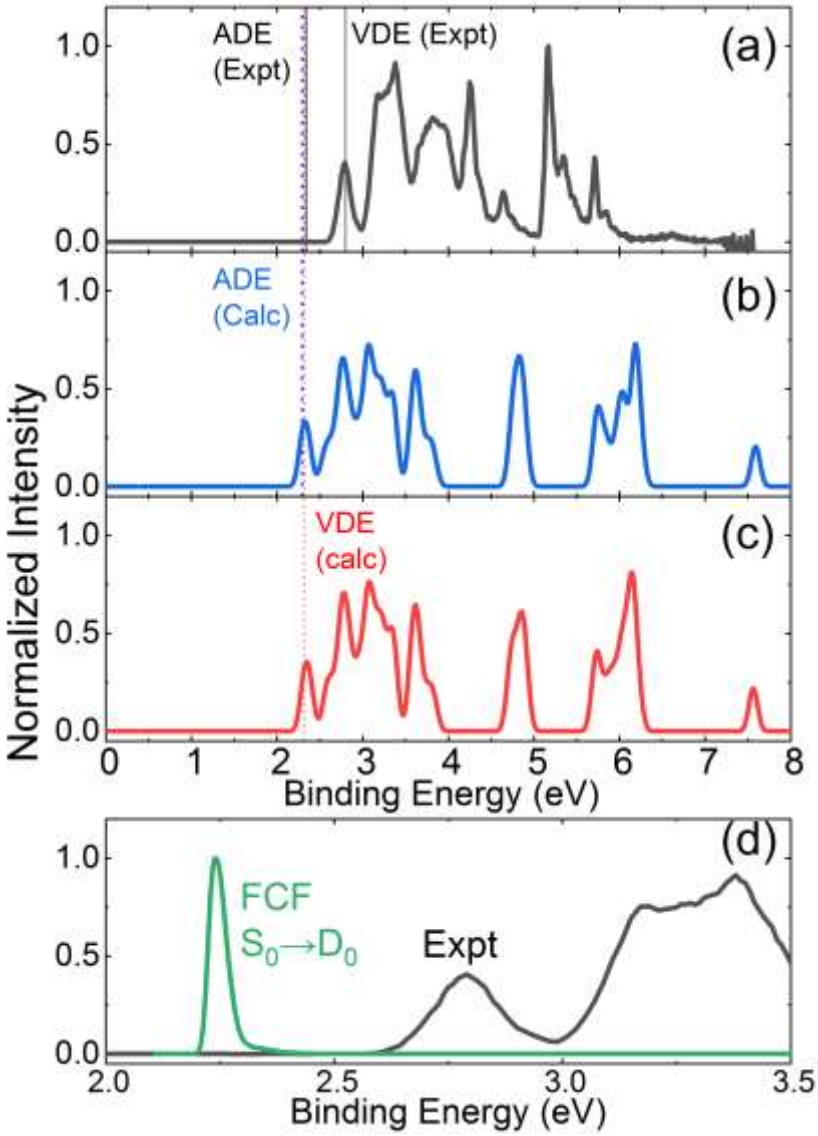

Figure 4.11. Experimental and simulated PES of $B_{12}I_{12}^{2-}$. The PES in (a) show the experimental PES obtained by Warneke *et al*.[13] (b) Calculated ADE PES using the B3LYP method could be compared to the calculated VDE PES (c). FCFs were also generated for the first excited state as shown in (d). The calculated ADE and VDE values are compared with those determined experimentally.

The vibrational frequencies measured using IRMPD correlated well with the calculated frequencies, shown in Table 4.3, which allows us to take confidence in the computational results.

Table 4.3. Comparisons of computational and IRMPD experimental values.

X =	Computational (cm^{-1})	IRMPD Experimental Data (cm^{-1})	Vibrational Motion
H	1072	1050[(a)]	Wagging
F	1225	1250[(b),(c)]	Breathing
Cl	1012	1045[(c)]	Breathing

[(a)] This value is taken from reference [7].
[(b)] This value is taken from reference [8].
[(c)] This value is taken from reference [9].

As X of $B_{12}X_{12}^{2-}$ increases in size, the vibrational frequency that corresponds to the $B_{12}X_{12}$ breathing mode decreases, as seen in Table 4.4. Again, the same trend is seen for the monoanion case. The difference in the dianion and monoanion vibrational frequencies tells us that after removing an electron, there is a change in the electronic and geometric structure, which agrees with the observations we have seen for PES in which there are differences between ADE and VDE values.

Table 4.4. Calculated vibrational frequencies of $B_{12}X_{12}$ breathing mode for the monoanion, D_0, and dianion, S_0.

X =	$B_{12}X_{12}^{2-}$, Dianion S_0 (cm^{-1})	$B_{12}X_{12}^{-}$, Monoanion D_0 (cm^{-1})	$\Delta\ (\nu_{S_0} - \nu_{D_0})$ (cm^{-1})
H	2511	2621	110
F	1225	1262	37
Cl	1012	997	15
Br	955	931	24
I	897	906	9

For a diatomic molecule, the vibrational frequency, ω_e (in cm^{-1}) can be described with reduced mass μ (kg) and force constant, k_f (N/m):

$$\omega_e = \frac{1}{200\pi c}\sqrt{\frac{k_f}{\mu}}. \tag{4.1}$$

It is clear to see that the vibrational frequency is inversely proportional to the reduced mass. $B_{12}X_{12}^{2-}$ is not a diatomic model but the same concept can be applied. When X increases in mass, going from H to I, the vibrational frequency decreases, which is observed in Table 4.4. This indicates the accuracy of the computational results.

4.4 Conclusion

Using DFT and FCF calculations, the PES of the $B_{12}X_{12}^{2-}$ species were simulated. Theoretical calculations accurately predicted the trend of each transition, ADE and VDE, as X = H, F − I, which was comparable with the experimental data. DFT calculations mimicked the general trend of the PES data, which was further refined using FCF calculations. The FCFs were only calculated for the first transition (from the ground singlet state to the ground doublet state) but they significantly improve the accuracy of the first PES band, especially for $B_{12}F_{12}^{2-}$. Further calculations for the other transitions are required to fully represent the vibronic transitions. Fewer structural distortions were observed computationally as $B_{12}X_{12}^{2-}$ size increased, leading to similar ADE and VDE values and a collapse of vibrational structure in the FCF simulations. Using the IRMPD data studied by the Hopkins group,[7–9] the high accuracy of the DFT calculations were confirmed. Further studies are required to better understand the electronic spectra observed.

Chapter 5. Broadband femtosecond transient absorption of $B_{12}F_{12}^{2-}$

Meixin Cheng, Dr. Nicolás Rivas, and Prof. Germán Sciaini performed broadband-femtosecond-transient absorption (bb-fs-TA) measurements. Meixin Cheng and Dr. Nicolás Rivas analysed the experimental data. Meixin Cheng, Prof. Anna Klinkova and Prof. Rodney Smith carried out spectroelectrochemistry measurements. Dr. Ariel A. Petruk performed molecular dynamics (MD) simulations. Prof. W. Scott Hopkins, Dr. Kostyantyn Pichugin and I carried out electronic structure calculations.

5.1 Introduction

Charge to transfer solvent (CTTS) states are weakly bound excited electronic states, which are stabilized by the solvent field. As an example, CTTS states are responsible for the generation of the well-studied solvated electron, e^-_{sv}.[44–61] CTTS states have been widely investigated, with most of the original steady state spectroscopic work and a long list of CTTS capable anions being reported in the 1970's.[62] More recent investigations have focused on the dynamics of CTTS states and reaction intermediates involved in the geminate recombination and production of the solvated electron, $e^-_{sv.}$ To date, the most studied CTTS system has been I^- in aqueous solutions as well as in gas phase water clusters.[17,18,63–72] The popularity of I^-_{aq} for elucidating the ultrafast dynamics of the electron photodetachment process is due to its simple atomistic nature which facilitates model calculations as well as the fact that its broad ultraviolet (UV) CTTS absorption band is readily accessible by femtosecond laser technology via high harmonic generation. The formation and solvation dynamics of the hydrated electron, e^-_{aq}, from I^-_{aq} have been investigated by fs-TA and fs-PES.[18,67–72] One of the main challenges has been the clear identification of the kinetic channels due to the fact that signals originating from the CTTS state I^{-*}_{aq}, e^-_{aq}, and reaction intermediates such as the caged contact pair $\{I^{\bullet}\cdot e^-\}_{aq}$ and solvent separated pairs show substantial overlap in the

visible-near infrared (Vis-NIR) spectral region.[71] This has been circumvented to some extent by the application of broadband femtosecond transient absorption (bb-fs-TA) with probe wavelengths in the UV-Vis range[69] and fs-X-ray absorption,[17] which made possible the observation of $I^{\bullet}_{aq}$. In addition, fs-fluorescence up conversion garnered unique insights into the early electron ejection dynamics from the CTTS state, I^{-*}_{aq}.[63] Furthermore, careful bb-fs-TA studies of the CTTS state of the exotic solvated sodide system Na^{-}_{sv} in tetrahydrofuran have broadened our understanding of electron detachment and recombination dynamics through detection of solvated electrons, e^{-}_{sv}, the nascent solvated neutral atom $Na^{\bullet}_{sv}$ or tight contact pair $\{Na^{+}\cdot e^{-}\}_{sv}$, and other relevant reactive species.[73–75]

The literature reporting on fs-TA studies of CTTS electrons of MCAs is relatively sparse. An exception is ferrocyanide $Fe(CN)_6^{4-}$, which is considered the actinometric standard for the production of e^{-}_{aq}.[68] However, $Fe(CN)_6^{4-}$ is an interesting case in its own right due to the fact that its CTTS band overlaps with intramolecular charge transfer transitions and absorption from ferricyanide and other photoproducts.[68,76] Other fs-TA experiments on the compact aqueous dianions CO_3^{2-} and SO_3^{2-} suggest that the CTTS electron escapes to the solvent without the preformation of the caged contact pair, $\{CO_3^{1-}\cdot e^{-}\}_{sv}$ or $\{SO_3^{1-}\cdot e^{-}\}_{sv}$; possibly because of the strong Coulomb repulsion between the photoexcited electron and the nascent radical monoanion.[68] Regardless of the system under study, the dynamics of CTTS electrons have been so far well described by similar kinetic mechanisms that inherently assume a very short-lived CTTS state which spontaneously releases the photoexcited electron to the surrounding solvent medium. In the case of I^{-}_{aq}, for instance, the CTTS state was found to thermalize in less than 100 fs followed by electron ejection in the 100 – 400-fs timescale.[63]

In order to bring new insights to the understanding of Coulomb repulsion effects on the ejection dynamics of photoexcited electrons in MCAs, we have chosen the doubly-charged $B_{12}F_{12}^{2-}$ anion as a model system. $B_{12}F_{12}^{2-}$ belongs to a family of superweakly coordinating anions, which have attracted the attention of chemists due to their three-dimensional aromatic properties[77] and potential applications in energy storage and neutron capture cancer therapy.[5,78,79] In the gas phase, $B_{12}F_{12}^{2-}$ is a stable and highly symmetric dianion with a VDE of 1.90(5) eV.[13] Recently, through a combination of gas-phase photoelectron spectroscopic measurements and theoretical TD-DFT calculations, the stability and electron detachment processes have been investigated for the family of $B_{12}X_{12}^{2-}$ (X = H, F – At). These studies indicate the presence of a repulsive Coulomb barrier (RCB) at the exit channel.[13] The RCB is a special feature of the potential energy surface of MCAs, which arises from an interplay between the stabilization energy inherent in filling the MCA MO's and the electron leading to an observed barrier to electron detachment, at which point the electron is free.[13,19] Since the initial studies which outline the role of RCB in the electron detachment process, focus has been on gas phase MCA's[80] as well as $SO_4^{2-}(H_2O)_n$ (n = 4–40)[81] clusters; the role of RCB in solution remains largely unexplored. Herein, we provide spectroscopic evidence for the effect of the RCB on the lifetime of the photoexcited doubly-charged aqueous anion $B_{12}F_{12}^{2-}{}_{aq}$.

5.2 Methods

5.2.1 Broadband femtosecond transient absorption measurements

The fs-laser system is a Light Conversion Pharos SP, which provides output pulses with 600 μJ of energy, 180 fs in duration, and a central wavelength λ = 1030 nm. The repetition rate of the laser is 10 kHz, which was reduced to 1 kHz through the use of an external pulse picker. This reduction in repetition rate was necessary to avoid undesirable effects (*i.e.*, cumulative heating and

photoproducts that can alter the TA signal). An optical parametric amplifier (Orpheus) followed by a fourth-harmonic generation module was used to generate (pump) pulses of about 2 μJ in the UV range. A small fraction of the fundamental radiation (about 0.2 μJ pulse energy) was employed to generate white light using a 3 mm thick YAG crystal. The white light beam was collimated and focused by two off-axis parabolic mirrors to minimize group velocity dispersion in the probe beam line. The white light (probe) spot size at the cuvette was 50 μm whereas the pump spot size was set 200 μm. The TA experiments were performed in a quasi-collinear arrangement with a small angle of 7° between the incident pump and probe beams. In addition, the angle between pump and probe (linear) polarizations was set at the magic angle of 54.7° to eliminate anisotropic rotational contributions to the TA signal; no differences were detected between parallel polarizations and magic angle configurations, most likely, due to the high symmetry (spherical) shape of the dianion.

Pump and probe beams were initially overlapped in space through the use of an aperture at the position of the liquid cell. The overlap was optimized by maximizing the transient absorption signal. We record differential TA spectra as a function of pump-probe time delay by modulating the pump beam with a mechanical chopper. The measured TA spectra were collected using a synchronized dispersive spectrometer (Avantes AvaSpec-ULS2048).

The white light probe spectrum generated from the YAG crystal was found to extend from λ = 500 nm to 950 nm (1.31 eV to 2.48 eV), see Figure 5.1. The lower photon energy limit was due to a short pass filter used to block the laser fundamental. In order to broaden the probe spectral range, a 3 mm thick CaF_2 window was also employed instead of YAG crystal (see Figure 5.1). This extended white light wavelength down to 380 nm (3.27 eV). We only implemented white light generation from CaF_2 to rule out the photoproduction of $B_{12}F_{12}^{-}{}_{aq}$. Laser damage of the CaF_2 crystal was found to be a serious problem, which required the illuminated area in the CaF_2 crystal

to be refreshed regularly and resulted in poorer white light source stability. Because of this, several time delay points were measured and averaged to improve data quality.

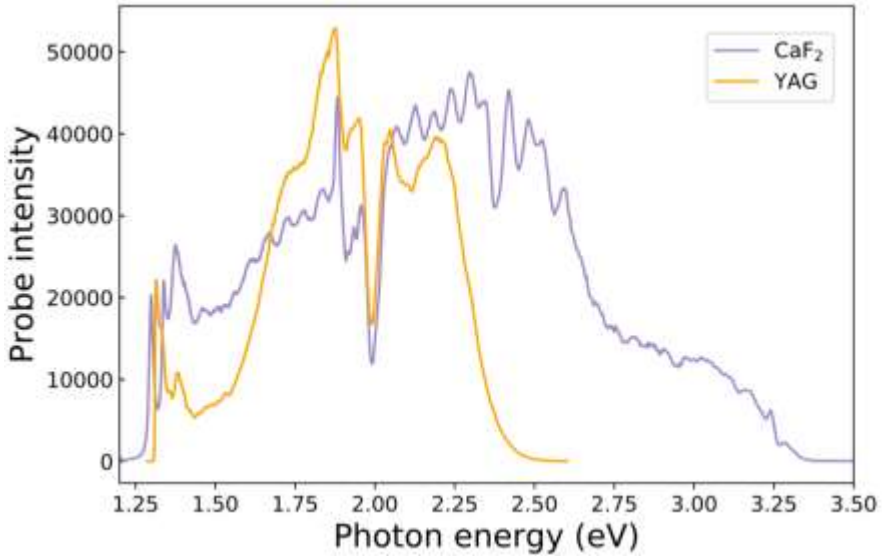

Figure 5.1. Femtosecond white light sources. Spectra of white light generated from a YAG crystal (orange trace) and from a CaF_2 crystal (purple trace). White light from CaF_2 was only implemented during a very short experiment carried out to prove that within the explored temporal span $B_{12}F_{12}^{-}{}_{aq}$ is not formed. Note that if photogenerated, $B_{12}F_{12}^{-}{}_{aq}$ and e^{-}_{aq} should be produced in a 1:1 ratio and both should be observable experimentally. We were not able to use CaF_2 as our white light source in long-term TA experiments owing to radiation damage. This is a well-known problem that requires the continuous translation of the CaF_2 crystal.

5.2.2 Sample preparation and temperature control

The potassium dodecafluoro-closo-dodecaborate $K_2B_{12}F_{12}$, solute (Sigma-Aldrich 720887) was diluted in deionized distilled water to a concentration of about 60 mM and placed in a quartz cuvette with a 1 mm pathlength. The solution was maintained at the desired temperature through the use of a proportional integrative derivative (PID) controller. Once the system reached stable conditions, temperature fluctuations were found to be ± 0.3 °C. Two temperature sensors were implemented. One sensor (Omega RTD PRTF-10-3-100-M30-50-E-GG) provided feedback to the PID controller and was installed in a conductive metallic block which was in thermal equilibrium with the heating element. The other temperature sensor, a fine gauge PFA insulated thermocouple (Omega 5TC-TT-K-30-36) was submerged into the analyte solution and positioned very close to the irradiated volume. This sensor configuration is essential to avoid systematic deviations from

the real temperature value. The cell was placed onto a conductive copper bar and surrounded by thermal insulation material. The copper rod was firmly attached to the heated metallic block. A set of small holes throughout the copper bar and the insulation layers allowed for experiments to be carried out in transmission mode.

5.2.3 UV-Vis Spectroelectrochemistry

UV-Vis spectroelectrochemical measurements were performed on a 4 mM $K_2B_{12}F_{12}$ solution in ACN using a Pt mesh as well as a glass-TCO as working electrodes. The reference electrode was a Pt disk and counter electrode was also a Pt wire. The relatively low concentration of $K_2B_{12}F_{12}$ in ACN was dictated by solubility. UV-Vis spectra were measured as a function of applied potential implementing a commercial fiber-based spectrometer (Ocean Optics Flame, equipped with a light source Ocean Optics DH-2000-BAL). A quartz cuvette with a 1 cm pathlength was used. A background spectrum was measured with pure ACN and all electrodes inside. Absorption measurements were performed on the $K_2B_{12}F_{12}$ solution as it underwent cyclic voltammetry scans from 0 V to 1.5 V and back to 0 V at a rate of 20 mV/s.

5.2.4 Electronic structure calculations

All electronic structure calculations reported in this work were performed using Gaussian 16 program package for computational chemistry.[24,82–85] The geometries of $B_{12}F_{12}^{2-}$, $B_{12}F_{12}^{-}$, and $B_{12}F_{11}H^{2-}$ anions were optimized using the B3LYP/6-311++g(d,p) level of theory in the presence of solvent using a polarizable continuum model (PCM). We have chosen the B3LYP DFT as it is well known to deliver good quality molecular structures with a reasonable computational burden for systems with a large number of degrees of freedom.[86] For all calculations, the point group of $B_{12}F_{12}^{2-}$ dianion had to be reduced from I_h to C_1 as the density

matrix breaks symmetry during the self-consistent field (SCF) procedure. Interestingly, there was no such problem for the same calculations on $B_{12}F_{12}^{2-}$ in vacuum; the error only occurs in the presence of solvent, as simulated through a PCM. This might be an indication of Jahn–Teller instability, which has been experimentally and theoretically confirmed for the radical anion.[42]

VDEs as a function of the dielectric constant for the optimized ground state $B_{12}F_{12}^{2-}$, $B_{12}F_{12}^{2-\bullet}$ were calculated using TD-DFT. Various solvent environments were treated by embedding the anions into PCMs.[87–89] ADEs for $B_{12}F_{12}^{2-}$ in each solvent were estimated by calculating the difference in energy between the dianion and the radical anion in their fully optimized geometries. The difference between ADE and VDE corresponds to the energy stabilization of $B_{12}F_{12}^{-}$ caused by structural reorganization. We found this value to be approximately 0.4 eV across the entire range of modeled solvents. In general, there is a reasonable agreement between theoretical predictions, bb-fs-TA and spectroelectrochemical measurements.

In order to gain a more realistic description of the electronic distribution of the "CTTS-like" state, $B_{12}F_{12}^{2-}$ dianion was embedded into an explicit primary solvation shell of water which was subsequently treated with PCM for long-range interactions. The water shell structure was obtained from MD simulations carried out with the AMBER 14 software package.[90] MD simulations were conducted as follows. The optimized geometry of $B_{12}F_{12}^{2-}$ as well as the charge distribution from natural population analysis using CHELPG were imported from our DFT/PCM calculations. The dianion was immersed in a truncated octahedral box of 760 water molecules, each treated using the simple point charge (SPC) water model,[91] and the system was optimized using a conjugate gradient algorithm for 2000 steps. One ns time interval between MD steps was used for the thermalization period to ensure numeric stability as the system was heated to 300 K over a time period of 1 ns. Subsequently, the system was equilibrated at constant pressure

(Berendsen barostat) and temperature (Langevin thermostat) for 4 ns. MD simulations were performed with periodic boundary conditions. The SHAKE algorithm was used to restrict the hydrogens to equilibrium bond lengths thus allowing the use of a 2 fs time step. A general Amber force field[92] was used to treat all interactions within $B_{12}F_{12}^{2-}$ and between $B_{12}F_{12}^{2-}$ and H_2O, with parameters for H_2O given by SPC.[91] Several snapshots of the system were randomly taken during a nanosecond time interval following the equilibration period. For ensuing electronic structure calculations to be practical, the number of water molecules was reduced to include only those located within the boundary of the first solvation shell.

Structures of $B_{12}F_{12}^{2-}$ with explicit water molecules shell from MD simulations were further optimized with B3LYP/6-311++g(d,p). All degrees of freedom but those of $B_{12}F_{12}^{2-}$ were fixed during optimization procedure. Thus, excited state calculations (TD-DFT) were performed on relaxed dianion within the "frozen" water environment from the previous step. Furthermore, we run a series of excited state calculations on $B_{12}F_{12}^{2-}$ in PCM along using the "best set" of density functionals as well as other theoretical methods (CIS and EOM-CCSD) to ensure the consistency and validity of our results. The excitation energies of the first ten excited singlet states of $B_{12}F_{12}^{2-}{}_{aq}$ from all aforementioned simulations are summarized in Table 5.1. Overall, the simulations (including that with higher aug-cc-pVQZ basis set) produce very similar results of about 4.1 eV and 6.2 eV for the first (1-4 states) and second (5-9 states) manifolds of quasi degenerate excited states. The exception is TD-CAM-B3LYP and EOM-CCSD predicting first and second manifolds to be by 0.4 eV and 0.6 eV higher in energy. The addition of explicit water molecules has no significant effect on transition in the first manifold since the LUMO remains primarily localized on $B_{12}F_{12}^{-}$ core. However, the situation is different (about 0.6 eV drop in excitation energy) for the second manifold where electronic excitations involve LUMO+1 and

higher orbitals that are more diffuse and thus become significantly perturbed by the presence of water molecules. In addition, the calculations with explicit water shell predict much stronger (oscillator strength is a factor of 20-50 larger) transitions to the second manifold than for those to the first. This outcome is in good qualitative agreement with our experimental observations of $B_{12}F_{12}^{2-}$ ground state absorption spectra, Figure 5.3. In contrast, the simulations with the solvent represented by PCM along suggest that transition to both manifolds are largely forbidden, *i.e.*, the oscillator strength is 0, which is definitely not the case for the higher energy transitions contributing to the more intense absorption bands around 6 eV. Finally, we found that excitation energies of $B_{12}F_{12}^{2-}$ enclosed in explicit water shell from different MD simulations snapshots to be essentially identical including those with different number of water molecules.

Since $B_{12}F_{11}H^{2-}$ is the highest yield by-product in the $B_{12}F_{12}^{2-}$ synthesis we carried out excited states calculations (TD-DFT) for the former to estimate its possible contribution to the electronic spectra. The results are presented in Table 5.2. Although slightly blue shifted (about 0.3 eV) the electronic spectra of $B_{12}F_{11}H^{2-}$ essentially overlaps with that of fully fluorinated dianion. Considering that the oscillator strength of the first absorption band (1-4 transitions) of $B_{12}F_{11}H^{2-}$ is predicted to be at least an order of magnitude larger than that of $B_{12}F_{12}^{2-}$ there is a chance that this by-product could be responsible for the observed fast decaying spectral feature (A1); see Global fitting analysis section for more details.

5.2.5 Global fitting analysis

Global lifetime analysis is a well-known method that is applied to model kinetic processes. In general, when analyzing unknown kinetics, it is necessary to start with a sufficient number of exponential decays (or growths) to fit data and their amplitudes.

In our case, we decided to conduct a global absorbance fitting assuming a single delay process, or equivalently two processes, one of which has $\tau_2 \rightarrow +\infty$.

$$A(E,t) = A_1(E)\, exp\left(-\frac{t}{\tau_1}\right) + A_2(E) \tag{5.1}$$

In Equation 5.1, *A(E,t)* is the transient absorbance at a photon energy of E and time delay after laser pump pulse of t. $A_2(E)$ corresponds to the absorbance of the long-lived species (e^-_{aq}), and therefore its spectral shape is readily obtained experimentally. $A_2(E)$ was collected by averaging our bb-fs-TA data in the range 500 ps – 800 ps, where the contribution to the absorption from $A_1(E)$, the short lifetime species, is negligible.

Thus, Eq. 1 can be rewritten as,

$$A_1(E,t) = A(E,t) - A_2(E) = A_1(E)\, exp\left(-\frac{t}{\tau_1}\right) \tag{5.2}$$

This procedure eliminates convergence issues and is found to produce consistent global fitting (GF) results among all the bb-*fs*-TA data measured, providing small residuals < 2% in all datasets.

5.2.6 Estimation of TA signal from e^-_{aq}

For the following, we estimate the expected absorbance for solvated electrons assuming that each absorbed photon produces one solvated electron. First, we calculate the absorbance for $B_{12}F_{12}^{2-}$ in solution using Beer-Lambert law.

$$A = \varepsilon \cdot c \cdot l \tag{5.3}$$

In which ε is the molar absorptivity of $B_{12}F_{12}^{2-}{}_{aq}$, 60 $M^{-1}cm^{-1}$, c is the concentration, 60×10^{-3} M, and l is the path length for absorption, 0.1 cm.

$$A(4.43\ eV) = 60M^{-1}cm^{-1} \cdot 60 \times 10^{-3}M \cdot 0.1cm = 0.36 \tag{5.4}$$

Absorbance is related to the incoming photon density *via* the following:

$$A = -log\left(\frac{\varphi^t}{\varphi^i}\right), \tag{5.5}$$

And

$$\varphi^t = \varphi^i - \varphi^{abs}, \tag{5.6}$$

Where φ^t is the transmitted photon flux, $\varphi^i - \varphi^{abs}$, and φ^i is the incoming laser flux, 1.7 mJcm^{-2}. Combining Equations 5.5 and 5.6, the flux of absorbed photons in the experiment is found from

$$\frac{\varphi^i - \varphi^{abs}}{\varphi^i} = 10^{-A} = 10^{-0.36} = 0.436, \tag{5.7}$$

Or

$$\varphi^{abs} = 0.564 \cdot \varphi^i = 0.564 \cdot 1.7 \times mJ\ cm^{-2} = 0.96\ mJ\ cm^{-2}, \tag{5.8}$$

This quantity can be converted to a total concentration of photons absorbed over the path length, *l*,

$$[photon_{abs}] = \frac{\varphi^{abs}}{l \cdot E_{photon}}, \tag{5.9}$$

in which E_{photon} is the energy per photon, 4.43 eV. As stated, we assume the concentration of absorbed photons is equal to the concentration of solvated electrons produced, [e^-_{aq}]. Therefore,

$$\left[e^-_{aq}\right] = \frac{0.00096\ J\ cm^{-2} \times 10^3 \frac{cm^3}{L}}{0.1\ cm \cdot 4.43 \frac{eV}{ph} \cdot 1 \frac{ph}{e^-} \cdot 1.602 \times 10^{-19} \frac{J}{eV} \cdot 6.022 \times 10^{23} \frac{e^-}{mol}} \approx 2 \times 10^{-5} M. \tag{5.10}$$

Finally, using the extinction coefficient for e^-_{aq} which is about $2 \times 10^4\ M^{-1}cm^{-1}$,[93] we can estimate the contribution to measure absorbance from e^-_{aq}.

$$A_{max}\left(e^-_{aq}\right) = 2 \times 10^{-5} M \cdot 2 \times 10^4 M^{-1}cm^{-1} \cdot 0.1cm = 0.040 \tag{5.11}$$

Hence the absorption due to the presence of solvated electron species would be at least a factor of two larger than that of the observed TA signal from $B_{12}F_{12}^{2-*}{}_{aq}$ at t = +2 ps (A($B_{12}F_{12}^{2-*}{}_{aq}$) = 0.017).

5.3 Results and discussion

We have performed a battery of spectroscopic experiments and theoretical calculations to gather sufficient information about solvation effects and relative energies of ground and electronic excited states for all relevant species in aqueous solution. Our findings are summarized in Figure 5.2.

We have observed that $B_{12}F_{12}^{2-}{}_{aq}$ exhibits a very weak "CTTS-like" absorption band (blue spectrum) in the UV spectral region with an extinction coefficient of only $\varepsilon_{max} \approx 67\ M^{-1}\ cm^{-1}$. It should be mentioned that the use of the acronym "CTTS" is rather arbitrary and comes from the fact that $B_{12}F_{12}^{2-}$ shares some similarities with I^- and other CTTS enabling anionic species. In the vacuum, they are both stable anions with no bound electronic excited states. However, in polar solvent media such as water and ACN, $B_{12}F_{12}^{2-}$ presents bound-to-bound transitions, see Figure 5.3 (b).

Our estimated absorbance (Section 2.5) for the $[e^-_{aq} \rightarrow e^{-*}_{aq}]$ transition confirms that if hydrated electrons are formed as main photoproducts, their transient signal should be at least twice the intensity observed for the $[B_{12}F_{12}^{2-*}{}_{aq} \rightarrow B_{12}F_{12}^{2-**}{}_{aq}]$ band. Note that the absorption spectrum of e^-_{aq} shown in Figure 5.2 (a) (yellow) has been reproduced from reference 94 whereas the light blue band corresponds to our ground-state $B_{12}F_{12}^{-}{}_{sv}$ absorption measurements as determined from spectroelectrochemistry, *vide infra* and Figure 5.3 (a), It is clear that there is no apparent contribution to the $B_{12}F_{12}^{2-*}$ spectrum from e^-_{aq} or $B_{12}F_{12}^{-}{}_{aq}$. Thus, we conclude that the observed transient signal must arise solely from the excited state absorption of the $B_{12}F_{12}^{2-}{}_{aq}$ dianion; *i.e.*, $[B_{12}F_{12}^{2-*}{}_{sv} \rightarrow B_{12}F_{12}^{2-**}{}_{sv}]$.

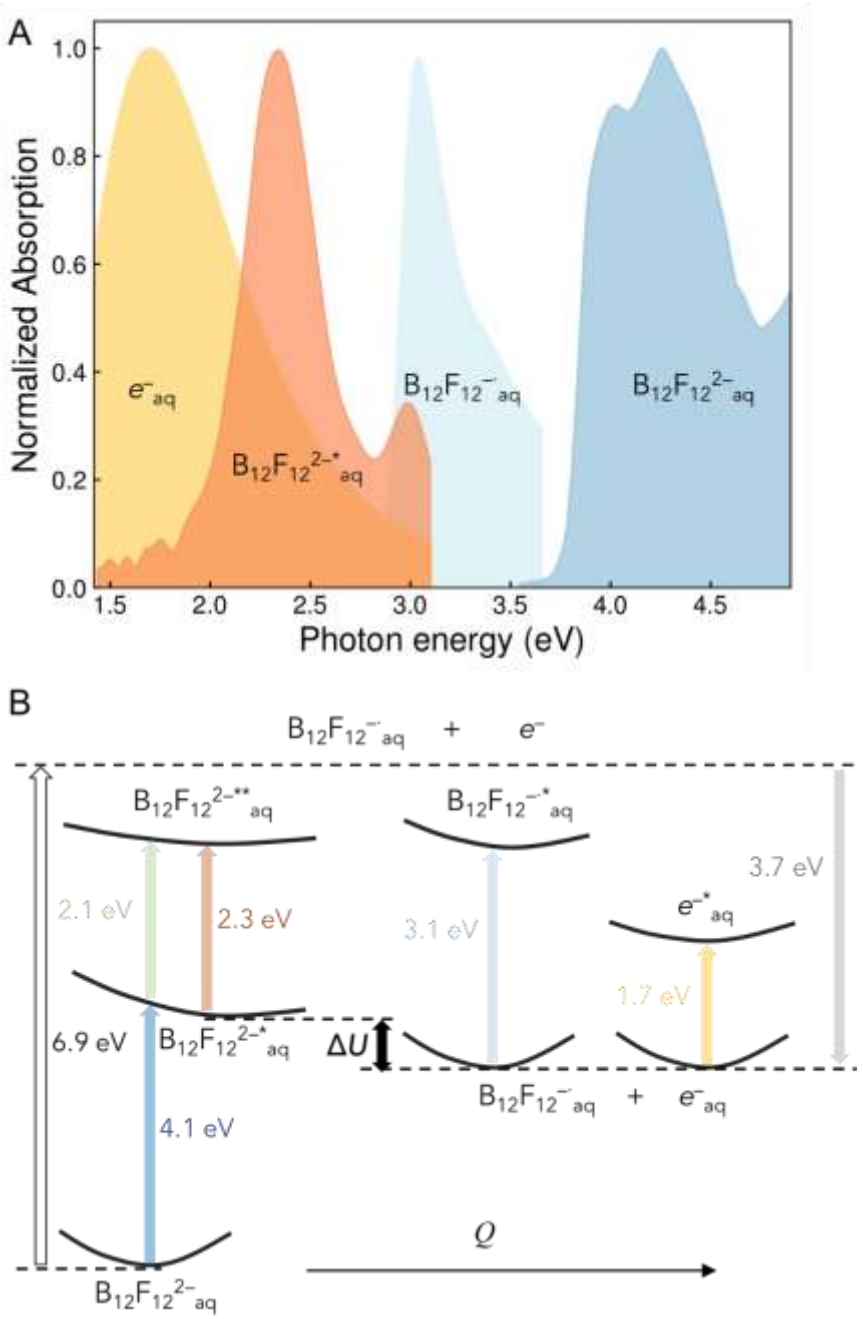

Figure 5.2. Measured and calculated spectroscopic bands and transitions for all relevant anionic species in liquid water. (a) Measured spectra color-coded to guide the eye according to their pertinent electronic transitions in panel b. Blue: absorption spectrum of $B_{12}F_{12}^{2-}{}_{aq}$ determined by UV-Vis spectroscopy; light blue: absorption spectrum of $B_{12}F_{12}^{2-\bullet}{}_{sv}$ measured by UV-Vis spectroelectrochemistry, see Methods and Figure 5.3 (a); orange: absorption spectrum of first electronic excited state of $B_{12}F_{12}^{2-}{}_{aq}$ obtained by bb-fs-TA at t = + 500 ps; yellow: absorption spectrum of aqueous electron adapted from reference [95]. (b) Blue, green, and light blue arrows correspond to calculated VTEs by TD-DFT/B3LYP with a PCM that accounts for the dielectric properties of water. Orange and yellow arrows correspond to the absorption maxima of the experimental spectra shown in panel a. Q is a generalized reaction coordinate. The first and second electronic excited states are distinguished with (*) and (**), respectively. Values corresponding to experimentally observed absorption maxima of $B_{12}F_{12}^{2-*}{}_{aq}$ and e^-_{aq} are displayed in orange and yellow, respectively. The VDE of aqueous e^- (≈ 3.3 - 3.7 eV)[96–98] is indicated with a grey arrow. We estimated a value for the energy stabilization following the CTTS process and equilibration of $\Delta E \approx 0.3 – 0.7$ eV.[99]

Comparative UV-Vis and bb-fs-TA spectroscopic measurements carried out in water and ACN indicate that the electronic transitions [$B_{12}F_{12}^{2-}{}_{sv}$ → $B_{12}F_{12}^{2-*}{}_{sv}$] (blue) and [$B_{12}F_{12}^{2-*}{}_{sv}$ → $B_{12}F_{12}^{2-**}{}_{sv}$] (orange) are nearly insensitive to changes in the dielectric constant of the surrounding media, see Figure 5.3 (b) and Figure 5.4.

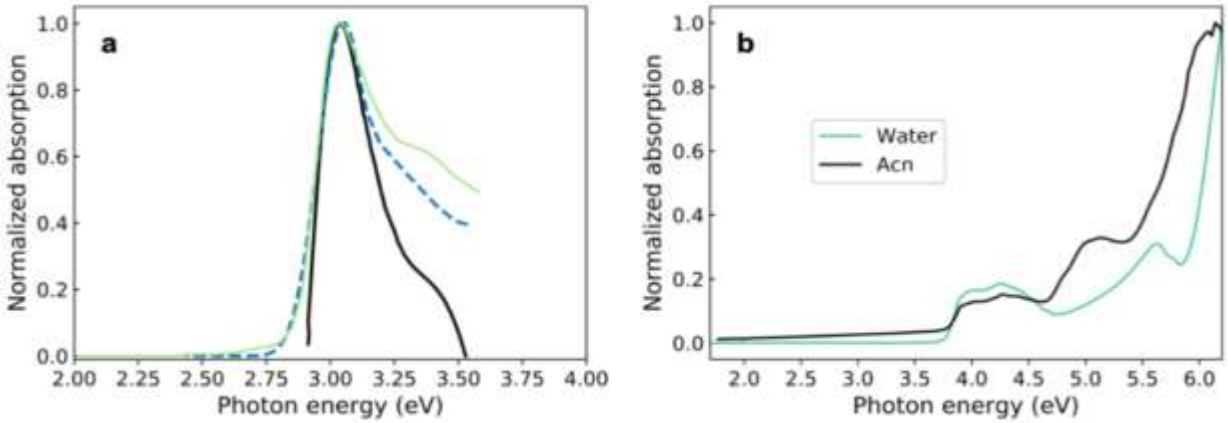

Figure 5.3. Absorption spectra of dianion and radical anion. (a) Absorption spectra of radical anion $B_{12}F_{12}^{-}{}_{sv}$ obtained by spectroelectrochemistry in ACN (dark trace); SO_2 (green trace),[100]; and EC:DEC (dashed blue trace).[101] The absorption maxima in these solvents were found at $E_{max} \approx 3.05$ eV. This is in accord with calculations that show no dependence of E_{max} upon changes of the dielectric constant of the solvent media. (b) Normalized absorption spectra obtained from solutions of $K_2B_{12}F_{12}$ dissolved in water (purple) and ACN (black). Note that the CTTS-like band of $B_{12}F_{12}^{2-}{}_{sv}$ is also insensitive to changes in the dielectric strength of the solvent.

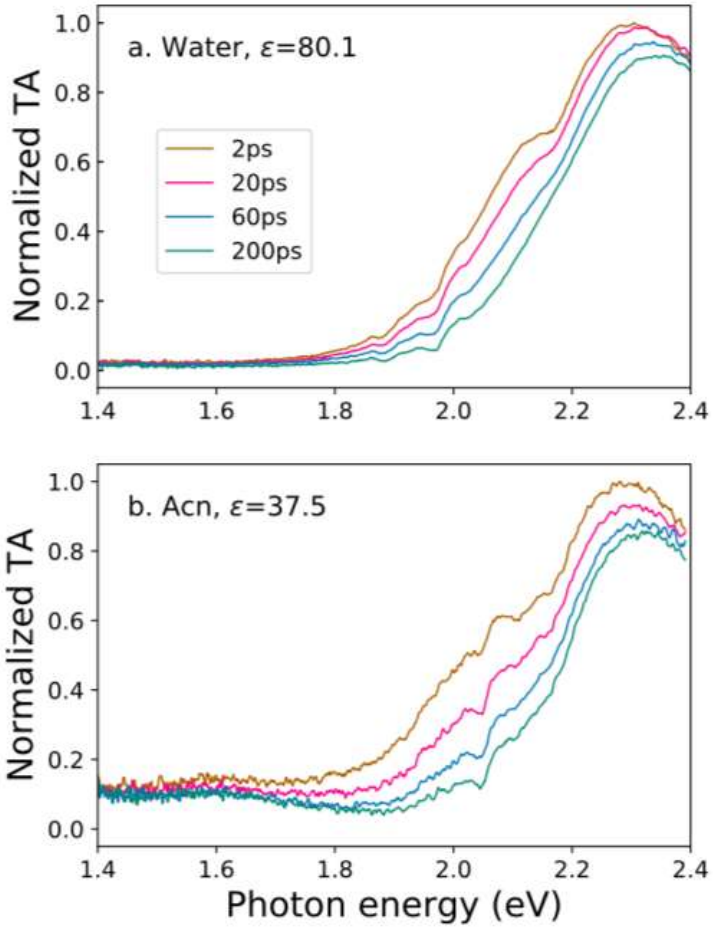

Figure 5.4 Bb-fs-TA in water and ACN. Bb-fs-TA spectra recorded at t = +2 ps, +20 ps, +60 ps, +200 ps and at a pump photon energy of 4.43 eV. (a) 60 mM solution of $K_2B_{12}F_{12}$ in water. (b) 4 mM $K_2B_{12}F_{12}$ solution in ACN. The data in ACN is much noisier due to the low concentration of $B_{12}F_{12}^{2-}$ that was limited by solubility. In addition, the background subtraction was not very effective owing to cumulative damaging effects of the window material during data collection. Measurements in ACN required a higher incident fluence.[102]

This fact suggests that the photoexcited electron remains in close proximity to the $B_{12}F_{12}^{-}$ core; a necessary condition for all aforementioned electronic states to preserve divalent character, and therefore experience a similar degree of electrostatic stabilization in different polar solvents. This is already a distinct difference when compared with previously investigated CTTS states which, because they show a large degree of electronic delocalization about the first solvation shell, are known to be sensitive to changes of both the solvent media and temperature.[62] Moreover, the application of spectroelectrochemistry allowed us to generate ground-state $B_{12}F_{12}^{-}{}_{sv}$ by oxidation of $B_{12}F_{12}^{2-}{}_{sv}$ in ACN, see Figure 5.5 and Figure 5.6.

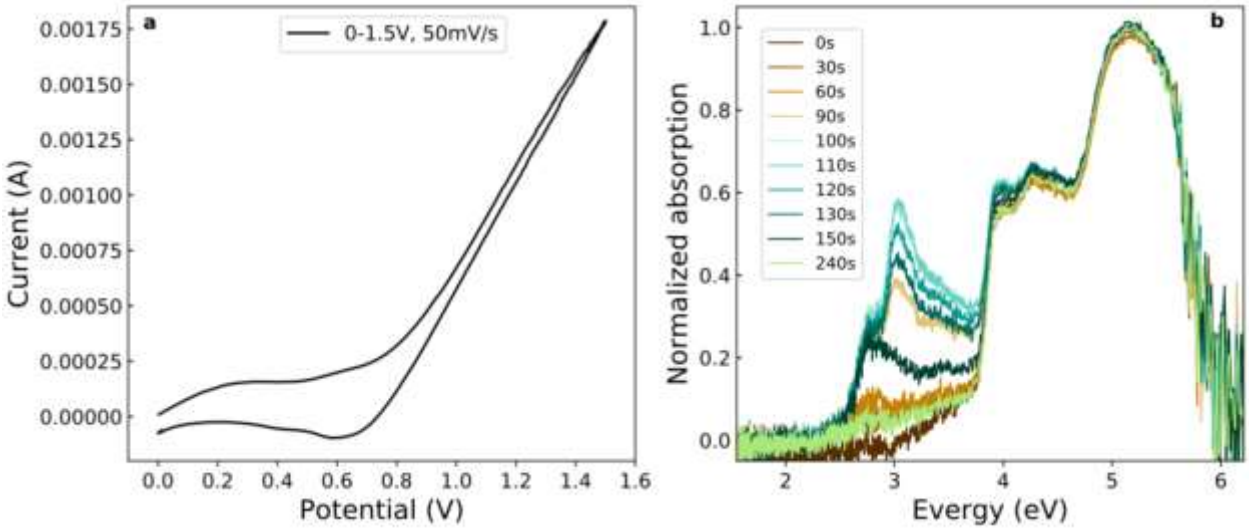

Figure 5.5 Spectroelectrochemical results part 1. (a) Cyclic voltammetric trace of 4mM $K_2B_{12}F_{12}$ in ACN with Pt mesh as working electrode, Pt wire as the counter electrode and Pt disk as the reference electrode. The scan range was 0 – 1.5V, and the scan rate was 20 mV/s. (b) UV-Vis spectra of $B_{12}F_{12}^{2-}{}_{sv}$ and $B_{12}F_{12}^{-}{}_{sv}$ (electrochemically generated) in ACN as a function of time (0 s corresponds to the start of the scan). As can be inferred from the relative intensities from the absorptions of $B_{12}F_{12}^{2-}{}_{sv}$ and $B_{12}F_{12}^{-}{}_{sv}$, the extinction coefficient of $B_{12}F_{12}^{-}{}_{sv}$ >> the extinction coefficient of $B_{12}F_{12}^{2-}{}_{sv}$. Therefore, if $B_{12}F_{12}^{-}{}_{sv}$ was produced by UV photoexcitation its TA signal should be noticeable. This also proves that $B_{12}F_{12}^{-}{}_{aq}$ is not produced by UV light irradiation.

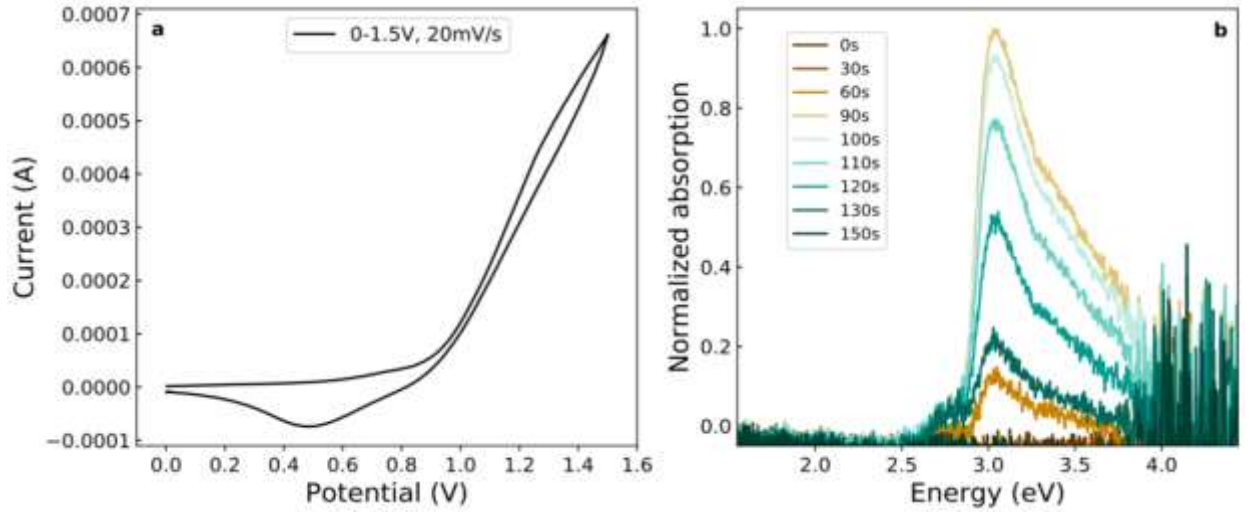

Figure 5.6 Spectroelectrochemical results part 2. (a) Cyclic voltammetric trace of 4mM $K_2B_{12}F_{12}$ in ACN with TCO coated-glass as the working electrode, Pt wire as the counter electrode and Pt disk as the reference electrode. The scan range was 0 –1.5 V, and the scan rate was 50 mV/s. Less noisy results were obtained with TCO coated-glass. The trace at 90 s has been smoothed before including it in Figure 5.2 (a) and Figure 5.3. (b) UV-Vis spectra of $B_{12}F_{12}^{2-}{}_{sv}$ and $B_{12}F_{12}^{-}{}_{sv}$ (electrochemically generated) in ACN as a function of time (0 s corresponds to the start of the scan). The signal saturates above 3.7 eV due to the absorption from the glass electrode.

The excitation energies to the first ten excited singlet states of $B_{12}F_{12}^{2-}{}_{aq}$ from all aforementioned calculations are summarized in Table 5.1. Overall, the calculations (including that

with the larger aug-cc-pVQZ basis set) produce very similar results of about 4.1 eV and 6.2 eV for the first (1-4 states) and second (5-9 states) manifolds of quasi-degenerate excited states. The exception is TD-CAM-B3LYP and EOM-CCSD predicting first and second manifolds to be 0.4 eV and 0.6 eV higher in energy, respectively. The addition of explicit water molecules has no significant effect on transitions to the first manifold. This is unsurprising as the lowest unoccupied molecular orbital (LUMO) remains primarily localized on the $B_{12}F_{12}^{-}$ core. However, the situation is different for the second manifold (about 0.6 eV drop in excitation energy) where electronic excitations involve LUMO+1 and higher orbitals that are more diffuse and thus become significantly perturbed by the presence of explicit water molecules. In addition, the calculations with an explicit water shell predict much stronger (oscillator strength is a factor of 20-50) transitions to the second manifold than for those to the first. This outcome is in good qualitative agreement with our experimental observations of $B_{12}F_{12}^{2-}$ ground state absorption spectra, Figure 5.3 (b). In contrast, the simulations with the solvent represented by PCM suggest that transitions to both manifolds are largely forbidden, *i.e.,* the oscillator strength is 0, which is definitely not the case for the higher energy transitions contributing to the more intense absorption bands around 6 eV. Finally, we also performed calculations of excitation energies for $B_{12}F_{12}^{2-}$ enclosed in an explicit water shell from different MD simulation snapshots. to be essentially identical including those with different number of water molecules.

Table 5.1. Excited States of $B_{12}F_{12}^{2-}$ in water.

Computational Method	Excitation Energies, eV									
	1	2	3	4	5	6	7	8	9	10
TD-B3LYP/ 6-311++g(d,p)	4.05	4.05	4.05	4.07	6.16	6.16	6.16	6.16	6.16	6.17
[1]TD-B3LYP/ 6-311++g(d,p)	4.13	4.15	4.16	4.18	5.39	5.43	5.70	5.74	5.77	5.82
[2]TD-B3LYP/ 6-311++g(d,p)	4.16	4.18	4.26	4.33	5.43	5.52	5.59	5.65	5.69	5.70
TD-B3LYP/ aug-cc-pVQZ	4.02	4.02	4.02	4.02	6.02	6.02	6.02	6.02	6.02	6.03
TD-LC-wPBE(20)/ 6-311++g(d,p)	3.92	3.92	3.92	3.94	6.18	6.18	6.19	6.19	6.19	6.40
TD-PBE0/ 6-311++g(d,p)	4.02	4.02	4.02	4.04	6.36	6.36	6.36	6.36	6.36	6.40
TD-mPW1PW91/ 6-311++g(d,p)	4.07	4.07	4.07	4.08	6.31	6.31	6.31	6.32	6.32	6.35
TD-X3LYP/ 6-311++g(d,p)	4.06	4.06	4.06	4.08	6.12	6.12	6.12	6.12	6.12	6.14
TD-CAM-B3LYP/ 6-311++g(d,p)	4.51	4.51	4.51	4.52	6.71	6.71	6.71	6.71	6.71	6.88
CIS-B3LYP/ 6-311++g(d,p)	4.07	4.07	4.07	4.08	6.17	6.17	6.17	6.17	6.17	6.18
EOM-CCSD/ 6-311++g(d,p)	4.46	4.46	4.46	4.47	6.79	6.79	6.79	6.79	6.79	6.91

Unless explicitly indicated, the water environment is treated using PCM for all calculations of the first ten excited singlet states of $B_{12}F_{12}^{2-}$

[1] $B_{12}F_{12}^{2-}$ in PCM with 20 explicit water molecules

[2] $B_{12}F_{12}^{2-}$ in PCM with 30 explicit water molecules

The $B_{12}F_{12}^{2-}{}_{sv}$ spectra show that the absorption maximum of $B_{12}F_{12}^{-}{}_{sv}$ (light blue spectrum in Figure 5.2) shows no dependence on the dielectric constant of the surrounding media, see Figure 5.3 (a). The aforementioned experimental observations were found to be in good agreement with our theoretical predictions obtained by TD-DFT at the B3LYP 6-311G++(d,p) level, in which we show there are very little changes to the electronic states of $B_{12}F_{12}^{2-}$ and $B_{12}F_{12}^{-}$ in various solvent environments, see Figure 5.7 and Figure 5.8.

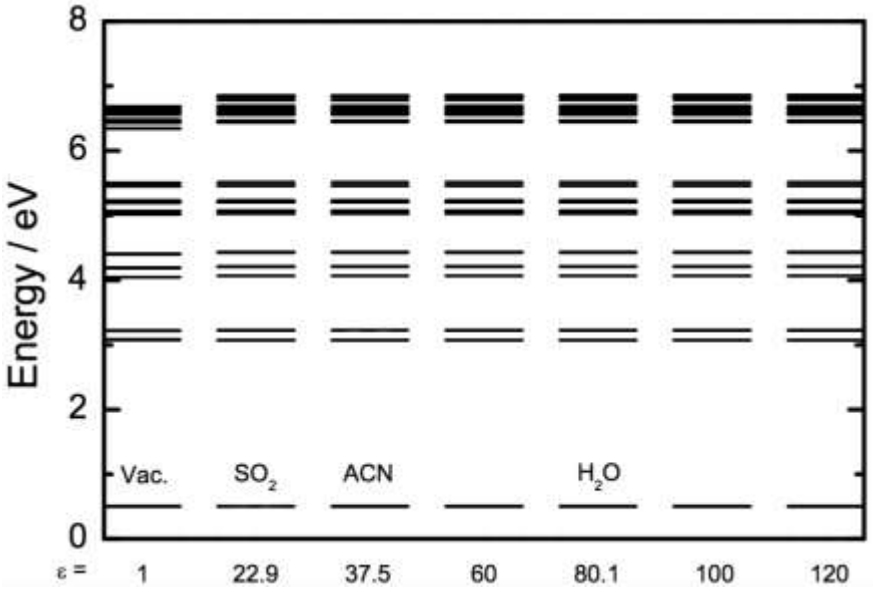

Figure 5.7. TD-B3LYP calculations in PCMs for $B_{12}F_{12}^{-}$. Electronic structure calculations at TD-DFT level of theory using the B3LYP functional and 6-311++G(d,p) basis set for the optimized ground-state structure of the radical anion $B_{12}F_{12}^{-}$. Energies are relative to the electronic ground state. Small to negligible relative energy changes are observed as a function of dielectric constant. This observation correlates very well with the fact that measured absorption maxima of $B_{12}F_{12}^{-}{}_{sv}$ in ACN, SO_2, and EC/EMC are all about 3.05 eV.

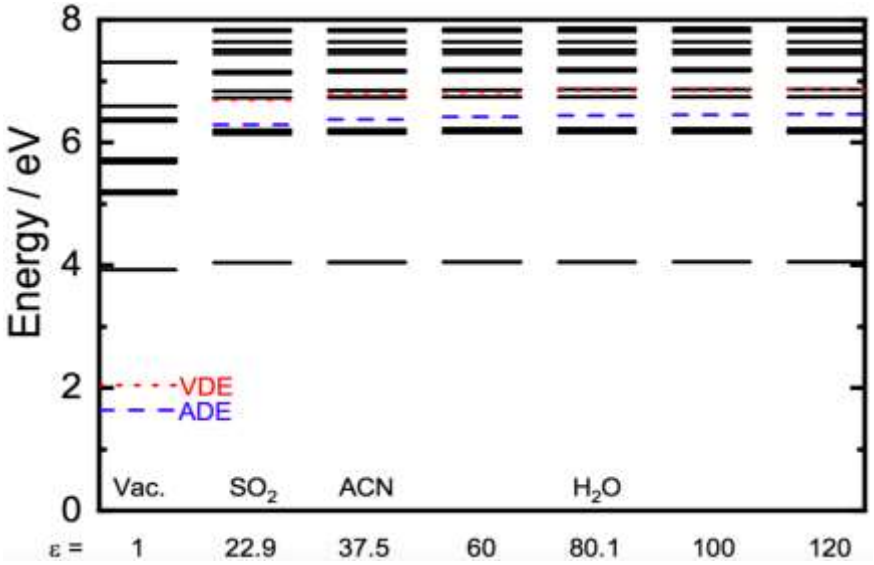

Figure 5.8. TD-B3LYP calculations in PCMs for $B_{12}F_{12}^{2-}$. Electronic structure calculations at TD-DFT level of theory using the B3LYP functional and 6-311++G(d,p) basis set for the optimized ground-state structure of dianion $B_{12}F_{12}^{2-}$. Energies are relative to the electronic ground state. Small to negligible relative energy changes are observed as a function of dielectric constant in the range of $\varepsilon = 22.9 - 120$. This observation correlates very well with the fact that measured absorption maxima of $B_{12}F_{12}^{2-}{}_{sv}$ and $B_{12}F_{12}^{2-*}{}_{sv}$ in ACN and water show negligible solvent dependence. The red dashed line corresponds to the VDE while the blue dashed line to the ADE. The difference between these two values correspond to the nuclear structural relaxation energy of $B_{12}F_{12}^{-}$, which is about 0.4 eV.

The detailed evolution of the TA signal is presented in Figure 5.10; the bb-fs-TA exhibit a shoulder at a probe photon energy of $E \approx 2.1$ eV that comes into sight immediately after photoexcitation and gradually depletes over a timespan of several tens of picoseconds, see Figure 5.4, 5.9 and 5.10 (a),(b). Following the disappearance of this spectral feature the bb-TA signal was found to remain essentially unchanged up to the 1 nanosecond limit of our optical delay stage. We observed very similar results when exploring different temperatures, photoexcitation conditions, and ACN as the solvent medium, as discussed previously. GF analyses of the bb-fs-TA data in Figure 5.10 (f) show that two spectral components and a single exponential decay, as per Equation 5.1, suffice to accurately model the observed behaviour.

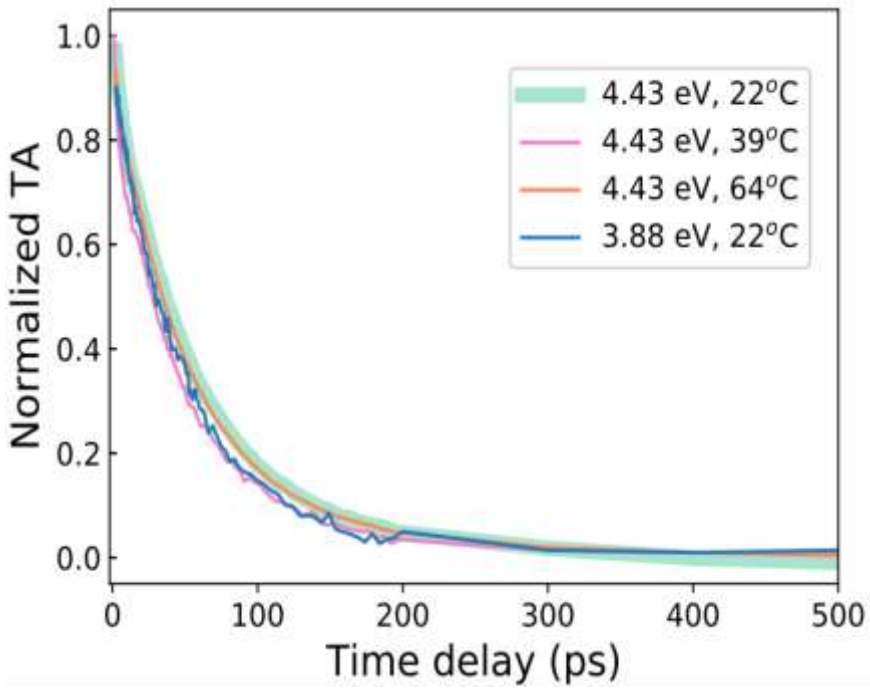

Figure 5.9. Exponential decay of A_2 under different conditions. Normalized time-dependent TA changes obtained by integrating the TA signal within the probe photon energy interval = 1.91–2.07 eV. Green trace: pump photon energy = 4.43 eV, temperature = 22 ˚C; pink trace: pump photon energy = 4.43 eV, temperature = 39 C; orange trace: pump photon energy = 4.43 eV, temperature 64 ˚C; blue trace: pump photon energy = 3.88 eV, temperature = 22 ˚C. All decay time constants were found to be in the 50-60 ps range, showing a very weak dependence on temperature and photoexcitation energy.

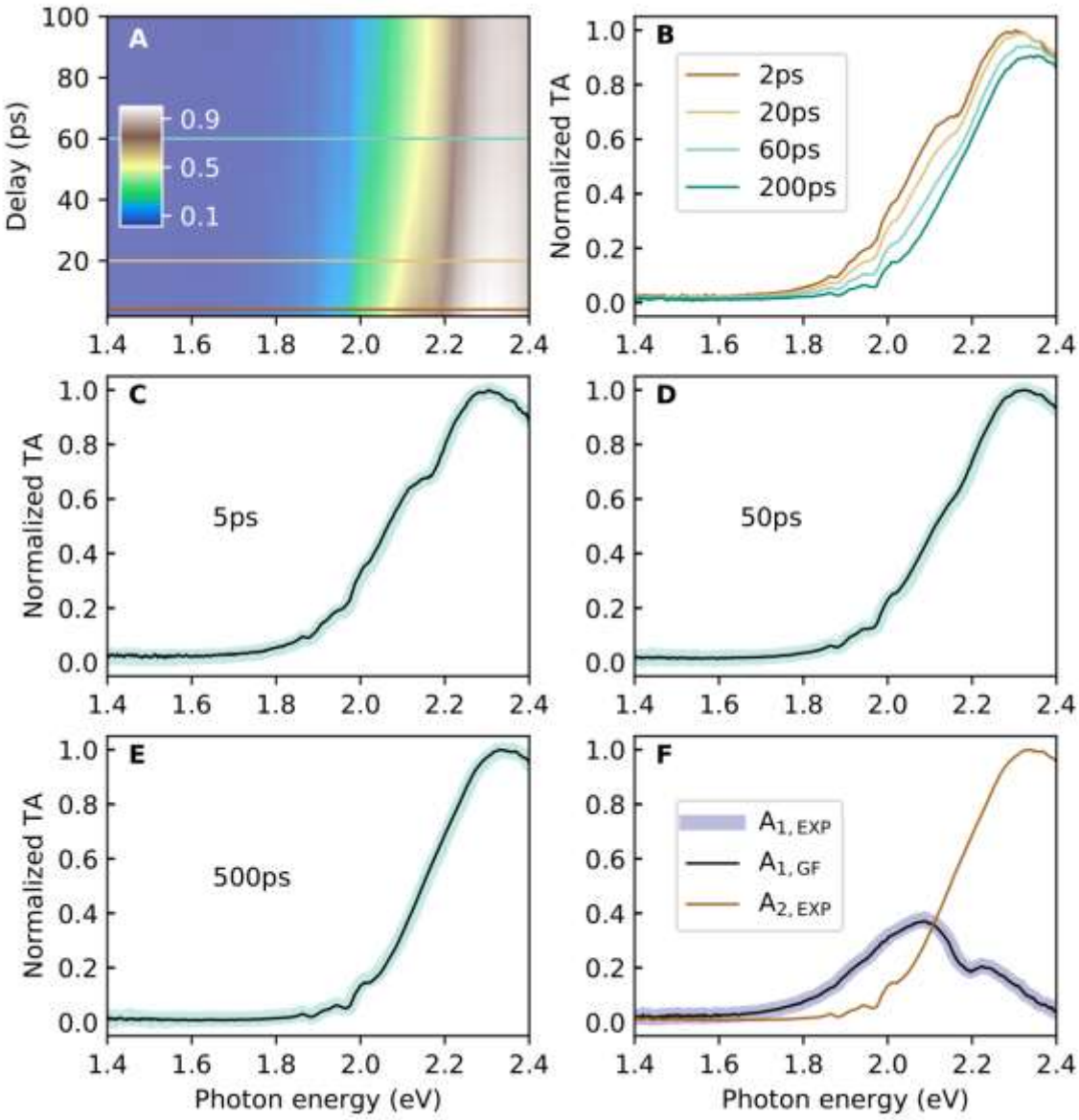

Figure 5.10. Bb-fs-TA and GF analysis. (a) Raw bb-fs-TA spectra obtained following excitation with a pump photon energy of 4.4 eV. (b) TA signal at four selected time delays (inset). (c) to (e) Results from GF analysis (thin black trace) overlaid with TA spectra (light cyan trace) at delays of t = +5, +50, and +500 ps. The line thickness of the experimental data has been exaggerated for clarity. (f) $A_{2,\ EXP}$ corresponds to the recorded bb-fs-TA signal at t > +500 ps. $A_{1,\ EXP}$ was obtained by subtracting $A_{2,\ EXP}$ from the bb-fs-TA spectrum at t = +2 ps. $A_{1,\ GF}$ is the result of the GF procedure. The decay time constant of A_1 was found to be $\tau_1 \approx 51$ ps. The maximum peak-to-peak deviation in residuals was of about 2% throughout the complete dataset.

In Equation 5.1, *E* spans the complete probed energy interval 1.4 eV – 2.4 eV, and *t* is in the range of +2 ps to +1000 ps. We selected $t > +2$ ps to ensure transient species are locally thermalized and to avoid possible artifacts from the cuvette windows in the proximity of time zero.

The results from the GF analysis are presented in Figure 5.10 (c) to (e). The spectral constituents, A_1 and A_2, are shown in Figure 5.10 (f). The origin of the shoulder (A_1) remains unclear; a plausible explanation is the presence of another excited state which, in analogy to the contact pair observed in iodide and sodide, decays to the ground electronic state of $B_{12}F_{12}^{2-}$ on the time span of tens of picoseconds. Alternatively, but less likely, the signal could arise due to the presence of small amount of $B_{12}F_{11}H^{2-}{}_{aq}$, the main impurity in the synthesis of $K_2B_{12}F_{12}$.[103,104] We carried out excited states calculations (TD-DFT) for $B_{12}F_{11}H^{2-}$ to estimate its potential contributions to the electronic spectra. The results are presented in Table 5.2. Although slightly blue shifted (about 0.3 eV) the electronic spectra of $B_{12}F_{11}H^{2-}$ essentially overlaps with that of the fully fluorinated dianion. Considering that the oscillator strength of the first absorption band (1-4 transitions) of $B_{12}F_{11}H^{2-}$ is predicted to be at least an order of magnitude larger than that of $B_{12}F_{12}^{2-}$ there is a chance that this by-product could be responsible for the observed fast decaying spectral feature (A_1).

The most intriguing observation in this study is the very long lifetime of $B_{12}F_{12}^{2-*}{}_{aq}$ (A_2). The weakly interacting nature of this dianion and its relatively small transition dipole moment, $B_{12}F_{12}^{2-} \rightarrow B_{12}F_{12}^{2-*}$, is a quasi-forbidden transition, account for the observed negligible internal conversion to the ground electronic state. However, in accord with the energetics presented in Figure 5.2, an excited electron should autodetach to form $B_{12}F_{12}^{-}{}_{aq}$ and $e^{-}{}_{aq}$. Such a process, which is favoured by the presence of an excess negative charge on the nascent monoanion core, is anticipated to occur on the sub-picosecond timescale.[18,17]

Table 5.2. Excited States of $B_{12}F_{11}H^{2-}$ in water.

Solvent Model	Excitation Energies, eV									
	1	2	3	4	5	6	7	8	9	10
PCM	4.32	4.32	4.48	4.48	6.03	6.03	6.03	6.03	6.17	6.20
PCM with 20 water molecules shell	4.42	4.44	4.54	4.57	5.74	5.75	5.89	5.91	5.98	6.00

All calculations are carried out at TD-B3LYP/6-311++g(d,p) level of theory.

For the sake of gaining information about the degree of electron transfer to the solvent, we look to the explicit water molecule electronic structure calculations. Representative snapshots, such as the one shown in Figure 5.11 (a), were utilized to perform TD-DFT calculations in which $B_{12}F_{12}^{2-}$ and its first solvation shell were treated explicitly within a water PCM. Figure 5.11 (b), depicts the difference in electron densities between the first electronic excited state and the ground state. A reorganization of the electronic distribution within the boron cage and outer shell of fluorine atoms is observed, with a small fraction of the excess negative charge being transferred to the surrounding water molecules, *i.e.*, mostly to hydrogen atoms bonded to fluorine centers *via* hydrogen bonding. Figure 5.11 (c), shows the calculated total charges on the boron cage, the fluorine shell, and the water molecules. From this analysis we can conclude that photoexcitation does not substantially alter the total charge on the dianion with only about 0.1*e* being transferred to the surrounding water molecules. Calculations with and without explicit water molecules show a very similar trend for the electron density redistribution within the dianion moiety, suggesting that the local stabilization of the excess two electrons arises mostly from electrostatic interactions.

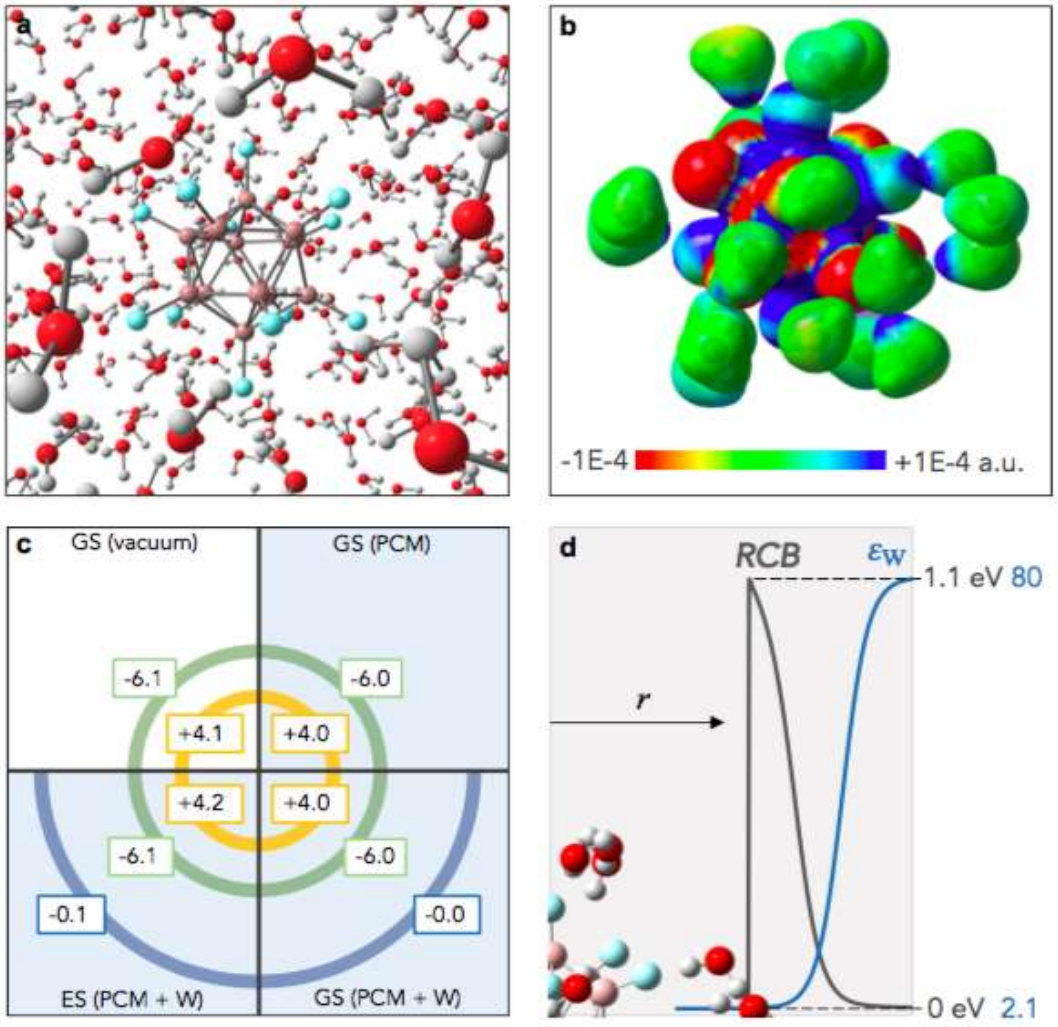

Figure 5.11. MD simulations, electronic structure calculations and RCB model in water. (a) Snapshot from MD simulation of $B_{12}F_{12}^{2-}$ in a box with 760 water molecules. (b) Electron density mapped surface obtained from TD-DFT (B3LYP) calculations. Blue and red correspond to gain and loss of electron density upon transition of the dianion to the first excited singlet state; a.u., atomic units. (c) Cartoon of calculated total charges under different conditions as specified in the quadrants. Circumferences in yellow, green and light blue represent the B-cage, the F-shell and the explicit water molecules (W) in the first solvation shell, respectively. The light blue background represents the inclusion of PCM. Ground electronic state; first excited electronic state. (d) Schematic representation of the calculated RCB (black trace) and the dielectric constant of water in the vicinity of the dianion, see Eqs. 5.12–5.14. The value of 1.1 eV was obtained at an arbitrary cutoff radius of r = 5.5 Å, which encloses the extent of the delocalization of photoelectron density in the excited state.

Moreover, a simple inspection of the shape of the unoccupied molecular orbitals (UMOs) in the vacuum, PCM, and PCM + W, suggests that the MCA is the major contributor to the lowest UMO (PCM + W) with an increased electronic delocalization about explicit water molecules in

upper UMOs, Figure 5.12. Although these findings are well-aligned with the aforementioned negligible dependence of electronic transition energies on changes of the solvent media, they do not explain the persistence of $B_{12}F_{12}^{2-*}{}_{aq}$ against electron autodetachment.

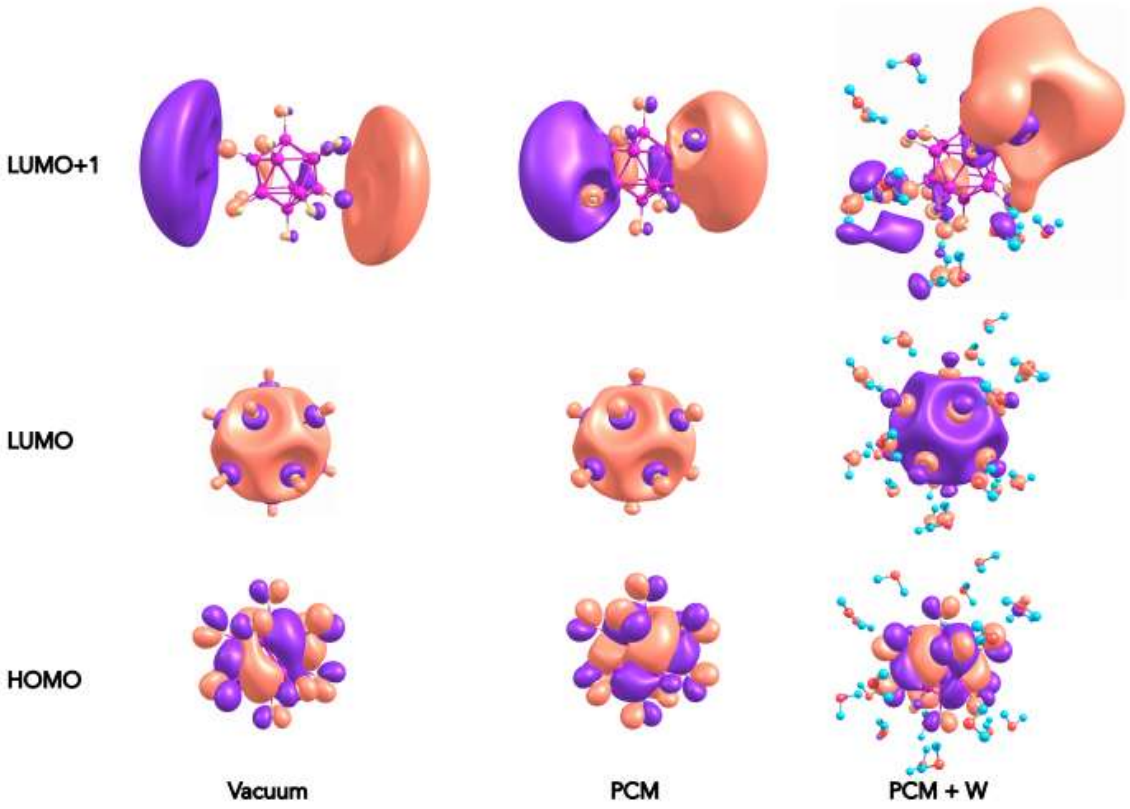

Figure 5.12. Molecular orbitals of $B_{12}F_{12}^{2-}$. Highest occupied molecular orbital (HOMO), LUMO, and LUMO+1 for $B_{12}F_{12}^{2-}$ as computed in the vacuum, within a PCM and within a PCM plus explicit water molecules. As can be seen the orbital delocalization increases as we move to upper energy orbitals.

We modelled the RCB of $B_{12}F_{12}^{2-}$ in water by considering a point charge interacting with a polarizable monoanion ($B_{12}F_{12}^{-}$, α = 21.02 Å^3).[13] The dependence of the relative dielectric constant of water, ε_w, as a function of the distance from the centre of mass of $B_{12}F_{12}^{-}{}_{aq}$, r, was approximated as in Equation 5.12,

$$\varepsilon_w(r) \approx 2.1 + \frac{77.9}{1+exp\left(-\frac{r-a}{b}\right)} \qquad (5.12)$$

where the parameters a = 8.1 Å and b = 0.35 Å were adjusted to reproduce the behavior of $\varepsilon_w(r) \approx \varepsilon_\perp$ for the component of the dielectric constant of water in the direction perpendicular to a planar polar wall[105] (see ε_w trace in Figure 5.11 (d)). The limit value of 2.1 for ε_w was obtained from very recent dielectric measurements in confined water.[106] Thus, the RCB potential in water, $V_{RCB,\,w}(r)$, becomes,

$$V_{RCB,w}(r) = \frac{1}{\varepsilon_w(r)} V_{RCB,vac}(r) \tag{5.13}$$

with

$$V_{RCB,vac}(r) = \frac{e^2}{4\pi\varepsilon_0 r} - \frac{\alpha e^2}{4\pi\varepsilon_0 r^4} \tag{5.14}$$

where $V_{RCB,\,vac}$ is the RCB potential in vacuum. The first term in Equation 5.14 is the repulsive Coulomb potential, and the second attractive term is associated with the charge-induced dipole interaction. The result of our point charge model in combination with the above observations are illustrated in Figure 5.11 (d). We calculated the height of $V_{RCB,\,w}$ to be approximately 1.1 eV. Thus, although the stabilization energy for $B_{12}F_{12}^{2-*}{}_{aq} \rightarrow B_{12}F_{12}^{-}{}_{aq} + e^-_{aq}$ is $|\Delta E| \approx 0.3 - 0.7$ eV (see Figure 5.2), the maximum of the RCB lies about 0.4 – 0.8 eV above the $B_{12}F_{12}^{2-*}{}_{aq}$ energy level. The presence of this local potential barrier explains the slow decay of $B_{12}F_{12}^{2-*}{}_{aq}$ to produce solvated electrons.

5.4 Conclusions

Our investigation of $B_{12}F_{12}^{2-}{}_{aq}$ has uncovered a photoelectron trapping mechanism that can be described as follows; UV excitation brings the system to the first electronic excited-state manifold, in which the electron is still primarily localized about the $B_{12}F_{12}^-$ core and within the attractive region of the RCB potential. The presence of this local activation energy barrier in the

exit channel slows down electron ejection kinetics, conferring a characteristic detachment time of tens to hundreds of nanoseconds, and therefore leading to the observed metastability of $B_{12}F_{12}^{2-*}{}_{aq}$. The similarities between the ground electronic state and the first excited electronic state of $B_{12}F_{12}^{2-}{}_{aq}$ and the stabilizing effects of the RCB seem to imply that the superweak character of this interesting MCA is maintained upon UV photoexcitation. Further quantum simulations with more sophisticated models are necessary to provide a deeper microscopic understanding of this process by including entropic factors and solvent reorganization effects. Nevertheless, since the RCB is a universal aspect shared by MCAs, we believe it should play an important role in modulating the photochemical reactivity of MCAs in solution.

Chapter 6. Conclusion

Through studying the gas- and solution-phase chemistry of $B_{12}X_{12}^{2-}$ (X = H, F − I), we obtain a better understanding of their respective electronic structures, transition energies, solvent interaction potentials, and structural properties. This thesis studied $B_{12}X_{12}^{2-}$ through theoretical calculations with comparisons to three experimental methods: DMS (X = H, F), PES (X = H, F − I), and pump probe absorption spectroscopy (X = F). Each experimental study was coupled with computational methods which employed DFT to investigate further the observed physical behaviour. Studies centred around $B_{12}H_{12}^{2-}$ and $B_{12}F_{12}^{2-}$ and their interactions with solvent clusters provides insight into more general $B_{12}X_{12}^{2-}$ (X = H, F − I) behaviour in solution and the gas phase through comparisons with $B_{12}H_{12}^{2-}$ and $B_{12}F_{12}^{2-}$ experiments and calculations.

In Chapter 3, the ion-solvent interactions of $B_{12}X_{12}^{2-}$ (X = H, F) were studied using DMS. Charge-dipole and charge-induced dipole dominated interactions between the dianion and solvent modifier. Due to the high symmetry of $B_{12}X_{12}^{2-}$ and large binding energies computed for $B_{12}X_{12}^{2-}$ with solvent modifiers it is believed that multiply solvated $B_{12}X_{12}^{2-}$ likely contributed to the observed DMS behaviour. This is due to observations indicative of large changes in mobility due to changes in collision cross section (CCS).[10] Coupling DMS experiments with computational work, the trends observed for $B_{12}H_{12}^{2-}$ and $B_{12}F_{12}^{2-}$ can be extended to the rest of the series (X= Cl, Br, I) for prediction of their solvent interaction potentials. Computational studies attribute the stronger clustering behaviour in $B_{12}H_{12}^{2-}$ experiments, in comparison to $B_{12}F_{12}^{2-}$, to higher electrostatic energy, which results from closer proximity of the solvent molecules to the $B_{12}X_{12}^{2-}$ cage. Thus, weaker clustering and solvent interactions are predicted for $B_{12}X_{12}^{2-}$ as X progresses from Cl to I.

Chapter 4 details DFT and FCF calculations employed to predict and assign the PES of $B_{12}X_{12}^{2-}$ (X = H, F − I). The accuracy of the computed spectra was evaluated by comparing them to experimentally obtained spectra published by Warneke *et al*.[13,14] Theoretical calculations predict ADEs and VDEs for X = H, F − I, which are comparable to experimental data. Overall comparisons of band shape between PES experimental data and calculated simulations were adequate for purely electronic transitions. FCF calculations were only completed for the first electronic transition (S_0 to D_0), but the accuracy of the calculated PES band was improved and shows clear vibronic transitions. Extending the FCF calculations to higher energy doublet states will allow for a better prediction of the vibronic structures and more accurate comparisons to experimental data. These calculations are ongoing. Experimental and calculated results show that the difference between ADE and VDE decreases in $B_{12}X_{12}^{2-}$ as X progresses from H to I. This suggests that geometric distortion upon electron detachment to the monoanion is reduced in $B_{12}X_{12}^{2-}$ as X goes from H to I. Additionally, it was found that the energy required to detach an electron from $B_{12}X_{12}^{-}$ decreased as X progressed from H to I. This aligns with the RCB trend, which decreases as charge separation (or size of the boron species) increases,[13] suggesting an increase in multiple charge stability as $B_{12}X_{12}^{2-}$ progresses from X= H, F − I.

The solution-phase behavior of $B_{12}F_{12}^{2-}$ was investigated in Chapter 5. Investigations of $B_{12}F_{12}^{2-}{}_{aq}$ suggests a photoelectron trapping mechanism for $B_{12}X_{12}^{2-}{}_{aq} \xrightarrow{h\nu} B_{12}X_{12}^{-}{}_{aq} + e^-$, in which the electron is still primarily localized about the $B_{12}F_{12}^{-}$ core and within the attractive region of the RCB potential. The RCB provides an activation barrier for $B_{12}F_{12}^{2-}{}_{aq} \rightarrow B_{12}F_{12}^{-}{}_{aq}$ which slows down electron ejection kinetics by a factor of $10^5 - 10^6$. The presence of an RCB confers a characteristic detachment time of tens to hundreds of nanoseconds, and therefore leads to an observed metastability of $B_{12}F_{12}^{2-*}{}_{aq}$ in experiments. The similarities between the ground and

excited states of $B_{12}F_{12}^{2-}{}_{aq}$ and the stabilizing effects of the RCB seem to imply that the superweak character of this MCA is maintained upon UV photoexcitation.

$B_{12}X_{12}^{2-}$ has been extensively studied experimentally and theoretically. Experimental findings indicate interesting electronic and geometric properties of this MCA, with extension of these studies to X= Cl, Br, and I made possible through calculations. Differential mobility spectrometry, photoelectron spectroscopy, and time-resolved absorption spectroscopy are shown useful in investigating and linking the gas-phase properties to the observed stability in solution. Expansion to other MCAs is believed possible through further studies of this model compound.

References

1. Verlet, J. R. R., Horke, D. A. & Chatterley, A. S. Excited states of multiply-charged anions probed by photoelectron imaging: Riding the repulsive Coulomb barrier. *Phys. Chem. Chem. Phys.* **16**, 15043–15052 (2014).
2. Boxford, W. E. & Dessent, C. E. H. Probing the intrinsic features and environmental stabilization of multiply charged anions. *Phys. Chem. Chem. Phys.* **8**, 5151–5165 (2006).
3. Boldyrev, A. I., Gutowski, M. & Simons, J. Small Multiply Charged Anions as Building Blocks in Chemistry. *Acc. Chem. Res.* **29**, 497–502 (1996).
4. Bukovsky, E. V. *et al.* Comparison of the Coordination of B12F122- , B12 Cl122- , and B12H122- to Na+ in the Solid State: Crystal Structures and Thermal Behavior of Na2(B12F12), Na 2(H2O)4(B12F12),Na2(B12Cl12), and Na2(H2O)6(B12Cl12). *Inorg. Chem.* **56**, 4369–4379 (2017).
5. Plesek, J. Potential Applications of the Boron Cluster Compounds. *Chem. Rev.* **92**, 269–278 (1992).
6. Soloway, A. H. *et al.* The chemistry of neutron capture therapy. *Chem. Rev.* **98**, 1515–1562 (1998).
7. De Vlugt, I. J. S. *et al.* Infrared-Driven Charge-Transfer in Transition Metal-Containing B12X122- (X = H, F) Clusters. *J. Phys. Chem. A* **122**, 7051–7061 (2018).
8. Hopkins, W. S. *et al.* Infrared-Driven Charge Transfer in Transition Metal B12F12 Clusters. *J. Phys. Chem. A* **119**, 8469–8475 (2015).
9. Carr, P. J. J. *et al.* The structure of proton-bound Triethylammonia (X = F, Cl) Clusters. *Mol. Phys.* **0**, 1–8 (2019).
10. Donald, W. A., Prell, J. S. & Hopkins, W. S. Comprhensive Analytical Chemistry: Advances in Ion Mobility-Mass Spectrometry: Fundamentals, Instrumentation and Applications, Chapter 4.
11. Hopkins, W. S. Determining the properties of gas-phase clusters. *Mol. Phys.* **113**, 3151–3158 (2015).
12. Campbell, J. L., Zhu, M. & Hopkins, W. S. Ion-molecule clustering in differential mobility spectrometry: Lessons learned from tetraalkylammonium cations and their isomers. *J. Am. Soc. Mass Spectrom.* **25**, 1583–1591 (2014).
13. Warneke, J. *et al.* Electronic Structure and Stability of [B12X12]2- (X = F-At): A Combined Photoelectron Spectroscopic and Theoretical Study. *J. Am. Chem. Soc.* **139**, 14749–14756 (2017).
14. Aprà, E., Warneke, J., Xantheas, S. S. & Wang, X. Bin. A benchmark photoelectron spectroscopic and theoretical study of the electronic stability of [B12H12]2-. *J. Chem. Phys.* **150**, (2019).
15. Hüfner, S. Photoelectron Spectroscopy: Principles and Applications, Third Edition. (2003).
16. Jenne, C., Keßler, M. & Warneke, J. Protic anions [H(B12X12)]- (X=F, Cl, Br, I) that act as brønsted acids in the gas phase. *Chem. - A Eur. J.* **21**, 5887–5891 (2015).
17. Chen, X. & Bradforth, S. E. The Ultrafast Dynamics of Photodetachment. *Annu. Rev. Phys. Chem.* **59**, 203–231 (2008).
18. Messina, F., Bräm, O., Cannizzo, A. & Chergui, M. Real-time observation of the charge transfer to solvent dynamics. *Nat. Commun.* **4**, (2013).
19. Wang, X. Bin, Ding, C. F. & Wang, L. S. Photodetachment spectroscopy of a doubly

charged anion: Direct observation of the repulsive coulomb barrier. *Phys. Rev. Lett.* **81**, 3351–3354 (1998).
20. Cramer, C. J. *Cramer, C. J. (2004) Essential of Computational Chemistry. Theories and Models, 2 Nd ed.;John Wiley and Sons, Ltd., Chichester.* (2004).
21. Phys, J. C. & Becke, A. D. Perspective : Fifty years of density-functional theory in chemical physics. **301**, 1–18 (2016).
22. Amusia, M. Y., Msezane, A. Z. & Shaginyan, V. R. Density Functional Theory versus the Hartree–Fock Method: Comparative Assessment. *Phys. Scr.* **68**, C133–C140 (2003).
23. Lewars, E. Computational chemistry: introduction to the theory and applications of molecular and quantum mechanics. (2016).
24. Frisch, M. J., Trucks, G. W., Schlegel, H. B., Scuseria, G. E., Robb, M. A., Cheeseman, J. R., Scalmani, G., Barone, V., Petersson, G. A., Nakatsuji, H., et al. Gaussian 16, Revision B.01, Gaussian, Inc., Wallingford CT, 2016. 2016 (2016).
25. Ansgar, S., Horn Hans & Ahlrichs, R. Fully optimized contracted Gaussian basis sets for atoms Li to Kr. **2571**, (1999).
26. Adamo, C. & Jacquemin, D. The calculations of excited-state properties with time-dependent density functional theory. *Chem. Soc. Rev.* **42**, 845–856 (2013).
27. Campbell, J. L., Le Blanc, J. Y. & Kibbey, R. G. Differential mobility spectrometry: A valuable technology for analyzing challenging biological samples. *Bioanalysis* **7**, 853–856 (2015).
28. Schneider, B. B., Covey, T. R., Coy, S. L., Krylov, E. V. & Nazarov, E. G. Planar differential mobility spectrometer as a pre-filter for atmospheric pressure ionization mass spectrometry. *Int. J. Mass Spectrom.* **298**, 45–54 (2010).
29. Schneider, B. B. *et al.* Differential Mobility Spectrometry / Mass Spectrometry History, Theory, Design, Optimization, Simulations, and Applications. doi:10.1002/mas.21453
30. Kolakowski, B. M. & Mester, Z. Review of applications of high-field asymmetric waveform ion mobility spectrometry (FAIMS) and differential mobility spectrometry (DMS). *Analyst* **132**, 842–864 (2007).
31. Liu, C. *et al.* Using differential mobility spectrometry to measure ion solvation: An examination of the roles of solvents and ionic structures in separating quinoline-based drugs. *Analyst* **140**, 6897–6903 (2015).
32. Tellinghuisen, J. *The Franck — Condon Principle in Bound - Free Transitions*.
33. Luis, J. M., Bishop, D. M. & Kirtman, B. A different approach for calculating Franck-Condon factors including anharmonicity. *J. Chem. Phys.* **120**, 813–822 (2004).
34. Kelley, A. M. *Spectroscopy and Condensed-Phase Molecular Spectroscopy and Photophysics*. (2013).
35. Andrews, D. L., Demidov, A. A. & Beeby, A. *An Introduction to Laser Spectroscopy Second Edition, Chapter 4*.
36. SciEx. 5500 Series of Instruments: System User Guide. 1–32 (2012).
37. Halkier, A., Coriani, S. & Jørgensen, P. The molecular electric quadrupole moment of N2. *Chem. Phys. Lett.* **294**, 292–296 (1998).
38. NIST Experimental Dipole Moments NIST Standard Reference Database Number 81, National Institute of Standards and Technology, Gaithersburg MD, www.cccbdb.nist.gov/diplistx (accessed March 4, 2019). 2019 (2019).
39. Walker, S. W. C. *et al.* Determining molecular properties with differential mobility spectrometry and machine learning. *Nat. Commun.* **9**, 1–7 (2018).

40. Boldyrev, A. I. & Simons, J. Isolated SO42- and PO43- anions do not exist. *J. Phys. Chem.* **98**, 2298–2300 (1994).
41. Dreuw, A. & Cederbaum, L. S. Nature of the repulsive Coulomb barrier in multiply charged negative ions. *Phys. Rev. A - At. Mol. Opt. Phys.* **63**, 1–13 (2001).
42. Malischewski, M., Bukovsky, E. V., Strauss, S. H. & Seppelt, K. Jahn-Teller Effect in the B12F12 Radical Anion and Energetic Preference of an Octahedral B6(BF2)6 Cluster Structure over an Icosahedral Structure for the Elusive Neutral B12F12. *Inorg. Chem.* **54**, 11563–11566 (2015).
43. Wang, X. Bin & Wang, L. S. Development of a low-temperature photoelectron spectroscopy instrument using an electrospray ion source and a cryogenically controlled ion trap. *Rev. Sci. Instrum.* **79**, (2008).
44. Schindewolf, U. Formation and Properties of Solvated Electrons. *Angew. Chemie Int. Ed. English* **7**, 190–203 (1968).
45. Deng, Z., Martyna, G. J. & Klein, M. L. Electronic states in metal-ammonia solutions. *Phys. Rev. Lett.* **71**, 267–270 (1993).
46. Jacobson, L. D. & Herbert, J. M. A one-electron model for the aqueous electron that includes many-body electron-water polarization: Bulk equilibrium structure, vertical electron binding energy, and optical absorption spectrum. *J. Chem. Phys.* **133**, (2010).
47. Jordan, K. D. & Johnson, M. A. Downsizing the Hydrated Electron's Lair. *Science (80-.).* **329**, 42–43 (2010).
48. Larsen, R. E., Glover, W. J. & Schwartz, B. J. Does the hydrated electron occupy a cavity. **2**, 0–14 (2011).
49. Abel, B. Hydrated Interfacial Ions and Electrons. *Annu. Rev. Phys. Chem.* **64**, 533–552 (2013).
50. Turi, L. & Rossky, P. J. Theoretical Studies of Spectroscopy and Dynamics of Hydrated Electrons. *Chem. Rev.* **112**, 5641–5674 (2012).
51. Young, R. M. & Neumark, D. M. Dynamics of Solvated Electrons in Clusters. *Chem. Rev.* **112**, 5553–5577 (2012).
52. Elkins, M. ; et al. Relaxation Mechanism of the Hydrated Electron. **342**, 1496–1499 (2013).
53. Herbert, J. ; et al. The hydrated electron. *Q. Rev. Chem. Soc.* **21**, 79–108 (1967).
54. Staib, A. & Borgis, D. Molecular dynamics simulation of an excess charge in water using mobile Gaussian orbitals. *J. Chem. Phys.* **103**, 2642–2655 (1995).
55. Emde, M. F., Baltuška, A., Kummrow, A., Pshenichnikov, M. S. & Wiersma, D. A. Ultrafast librational dynamics of the hydrated electron. *Phys. Rev. Lett.* **80**, 4645–4648 (1998).
56. Yokoyama, K., Silva, C., Son, D. H., Walhout, P. K. & Barbara, P. F. Detailed investigation of the femtosecond pump-probe spectroscopy of the hydrated electron. *J. Phys. Chem. A* **102**, 6957–6966 (1998).
57. Kambhampati, P., Son, D. H., Kee, T. W. & Barbara, P. F. Solvation dynamics of the hydrated electron depends on its initial degree of electron delocalization. *J. Phys. Chem. A* **106**, 2374–2378 (2002).
58. Hammer, N. I. How Do Small Water Clusters Bind an Excess How Do Small Water Clusters Bind an Excess Electron ? **675**, 675–679 (2006).
59. Turi, L. Characterization of Excess Electrons in Water-Cluster Anions by Quantum Simulations. *Science (80-.).* **310**, 1769c-1769c (2005).

60. Verlet, J. R. R. Observation of Large Water-Cluster Anions with Surface-Bound Excess Electrons. *Science (80-.).* **93**, 93–97 (2008).
61. Neumark, D. M. Spectroscopy and dynamics of excess electrons in clusters. *Mol. Phys.* **106**, 2183–2197 (2008).
62. Blandamer, M. J. & Fox, M. F. Theory and applications of charge-transfer-to-solvent spectra. *Chem. Rev.* **70**, 59–93 (1970).
63. Okuyama, H., Suzuki, Y. I., Karashima, S. & Suzuki, T. Charge-transfer-to-solvent reactions from I- to water, methanol, and ethanol studied by time-resolved photoelectron spectroscopy of liquids. *J. Chem. Phys.* **145**, (2016).
64. Pham, V. T. *et al.* Probing the transition from hydrophilic to hydrophobic solvation with atomic scale resolution. *J. Am. Chem. Soc.* **133**, 12740–12748 (2011).
65. Sheu, W. S. & Rossky, P. J. Charge-Transfer-to-Solvent Spectra of an Aqueous Halide Revisited via Computer Simulation. *J. Am. Chem. Soc.* **115**, 7729–7735 (1993).
66. Bradforth, S. E. & Jungwirth, P. Excited states of iodide anions in water: A comparison of the electronic structure in clusters and in bulk solution. *J. Phys. Chem. A* **106**, 1286–1298 (2002).
67. Robertson, W. H. & Johnson, M. A. MOLECULAR ASPECTS OF HALIDE ION HYDRATION: The Cluster Approach. *Annu. Rev. Phys. Chem.* **54**, 173–213 (2003).
68. Lehr, L. Electron Solvation in Finite Systems : Femtosecond Dynamics of Iodide*(Water)n Anion Clusters. **635**, 635–639 (2013).
69. Kloepfer, J. A., Vilchiz, V. H., Lenchenkov, V. A., Germaine, A. C. & Bradforth, S. E. The ejection distribution of solvated electrons generated by the one-photon photodetachment of aqueous I− and two-photon ionization of the solvent. *J. Chem. Phys.* **113**, 6288–6307 (2002).
70. Lian, R. *et al.* Electron photodetachment from aqueous anions. 3. Dynamics of geminate pairs derived from photoexcitation of Mono- Vs polyatomic anions. *J. Phys. Chem. A* **110**, 9071–9078 (2006).
71. Moskun, A. C., Bradforth, S. E., Thøgersen, J. & Keiding, S. Absence of a signature of aqueous I(2P1/2) after 200-nm photodetachment of I-(aq). *J. Phys. Chem. A* **110**, 10947–10955 (2006).
72. Lübcke, A., Buchner, F., Heine, N., Hertel, I. V. & Schultz, T. Time-resolved photoelectron spectroscopy of solvated electrons in aqueous NaI solution. *Phys. Chem. Chem. Phys.* **12**, 14629–14634 (2010).
73. Schwartz, B. J. Optical control of the electron during electron transfer. *Abstr. Pap. Am. Chem. Soc.* **222**, U241–U241 (2001).
74. Shoshana, O., Pérez Lustres, J. L., Ernsting, N. P. & Ruhman, S. Mapping CTTS dynamics of Na- in tetrahydrofurane with ultrafast multichannel pump-probe spectroscopy. *Phys. Chem. Chem. Phys.* **8**, 2599–2609 (2006).
75. Bragg, A. et al. Linear Response Breakdown in Solvation Dynamics Induced by Atomic Electron-Transfer Reactions. *Conserv. Exhib.* **321**, 225–240 (2013).
76. Reinhard, M. *et al.* Photooxidation and photoaquation of iron hexacyanide in aqueous solution: A picosecond X-ray absorption study. *Struct. Dyn.* **1**, (2014).
77. King, R. B. Three-dimensional aromaticity in polyhedral boranes and related molecules. *Chem. Rev.* **101**, 1119–1152 (2001).
78. Soloway, A. H. *et al.* The Chemistry of Neutron Capture Therapy. *Chem. Rev.* **98**, 1515–1562 (1998).

79. Xu, K. Electrolytes and Interphases in Li-Ion Batteries and Beyond. *Chem. Rev.* **114**, 11503–11618 (2014).
80. Wang, X.-B. & Wang, L.-S. Photoelectron Spectroscopy of Multiply Charged Anions. *Annu. Rev. Phys. Chem.* **60**, 105–126 (2009).
81. Yang, X., Wang, X. Bin & Wang, L. S. Photodetachment of hydrated sulfate doubly charged anions: SO42-(H2O)n(n = 4-40). *J. Phys. Chem. A* **106**, 7607–7616 (2002).
82. Becke, A. D. Density-functional thermochemistry. III. The role of exact exchange. *J. Chem. Phys.* **98**, 5648–5652 (1993).
83. Chengteh, L. ; et al. Development of the Colic-Salvetti correlation-energy into a functional of the electron density. *EE Eval. Eng.* **50**, 36–39 (2011).
84. Vosko, S. H., Wilk, L. & Nusair, M. Accurate spin-dependent electron liquid correlation energies for local spin density calculations: a critical analysis. *Can. J. Phys.* **58**, 1200–1211 (1980).
85. Stephens, P. J., Devlin, F. J., Chabalowski, C. F. & Frisch, M. J. Ab Initio calculation of vibrational absorption and circular dichroism spectra using density functional force fields. *J. Phys. Chem.* **98**, 11623–11627 (1994).
86. Ieritano, C., Campbell, J. L. & Hopkins, W. S. Unravelling the factors that drive separation in differential mobility spectrometry: A case study of regioisomeric phosphatidylcholine adducts. *Int. J. Mass Spectrom.* **444**, 116182 (2019).
87. Miertus, S. ; et al. Electrostatic Interaction of a Solute with a Continuum. A Direct Utilization of AB Initio Molecular Potentials for the Prevision of Solvent Effects.
88. Miertus, S. ; et al. Approximate Evaluations of the Electrostatic Free Energy and Internal Energy Changes in Solution Processes.
89. Pascual-Ahuir, J. L., Silla, E. & Tunon, I. GEPOL: An Improved Description of Molecular Surfaces. III. A New Algorithm for the Computation of a Solvent-Excluding Surface. *J. Comput. Chem.* **15**, 1127–1138 (1994).
90. D.A. Case, I.Y. Ben-Shalom, S.R. Brozell, D.S. Cerutti, T.E. Cheatham, III, V.W.D. Cruzeiro, T.A. Darden, R.E. Duke, D. Ghoreishi, M.K. Gilson, et al. AMBER 2018. 2018 (2018).
91. Berendsen, H., Postma, J., Van Gunsteren, W., and Hermans, J. 'Intermolecular Forces', Interaction Models for Water in Relation to Protein Hydration. *Intermol. Forces* 331–342 (1981).
92. Wang, J., Wolf, R. M., Caldwell, J. W., Kollman, P. A. & Case, D. A. Development and Testing of a General Amber Force Field. **56531**, (2004).
93. Kloepfer, J. ; et al. Femtosecond dynamics of photodetachment of the iodide anion in solution: resonant excitation into the charge-transfer-to-solvent state.
94. Jou, F.-Y. & Freeman, G. R. Band resolution of optical spectra of solvated electrons in water, alcohols, and tetrahydrofuran. *Can. J. Chem.* **57**, 591–597 (2006).
95. Jacquemin, D., Wathelet, V., Perpète, E. A. & Adamo, C. Extensive TD-DFT benchmark: Singlet-excited states of organic molecules. *J. Chem. Theory Comput.* **5**, 2420–2435 (2009).
96. Siefermann, K. R. *et al.* Binding energies, lifetimes and implications of bulk and interface solvated electrons in water. *Nat. Chem.* **2**, 274–279 (2010).
97. Tang, Y. *et al.* Direct measurement of vertical binding energy of a hydrated electron. *Phys. Chem. Chem. Phys.* **12**, 3653–3655 (2010).
98. Luckhaus, D., Yamamoto, Y., Suzuki, T. & Signorell, R. Supplementary Materials for

Genuine binding energy of the hydrated electron. **3**, 1603224 (2017).
99. We would like to mention that the estimated value for DE assumes that the dianion and the radical anion experience a similar magnitude of energy relaxation caused by structural reorganization. Calculations at the DFT-B3LYP level of theory in a PCM showed . 4
100. Boeré, R. T. *et al.* On the oxidation of the three-dimensional aromatics [B12X 12]2- (X=F, Cl, Br, I). *Chem. - A Eur. J.* **20**, 4447–4459 (2014).
101. GirishKumar, G., Bailey, W. H., Peterson, B. K. & Casteel, W. J. Electrochemical and Spectroscopic Investigations of the Overcharge Behavior of StabiLife Electrolyte Salts in LithiumIon Batteries. **153**, 2011 (2011).
102. Shreve, A. T., Elkins, M. H. & Neumark, D. M. Photoelectron spectroscopy of solvated electrons in alcohol and acetonitrile microjets. *Chem. Sci.* **4**, 1633–1639 (2013).
103. Ivanov, S. V., Miller, S. M., Anderson, O. P., Solntsev, K. A. & Strauss, S. H. Synthesis and stability of reactive salts of dodecafluoro-closo-dodecaborate(2-). *J. Am. Chem. Soc.* **125**, 4694–4695 (2003).
104. Peryshkov, D. V., Popov, A. A. & Strauss, S. H. Direct perfluorination of K2B12H12 in acetonitrile occurs at the gas bubble-solution interface and is inhibited by HF. Experimental and DFT study of inhibition by protic acids and soft, polarizable anions. *J. Am. Chem. Soc.* **131**, 18393–18403 (2009).
105. Schlaich, A., Knapp, E. W. & Netz, R. R. Water Dielectric Effects in Planar Confinement. *Phys. Rev. Lett.* **117**, 1–5 (2016).
106. Fabregas, R. *et al.* Anomalously low dielectric constant of confined water. *Science (80-.).* **360**, 1339–1342 (2018).

Appendix A.1

Visually represented optimized structures for Chapter 3.

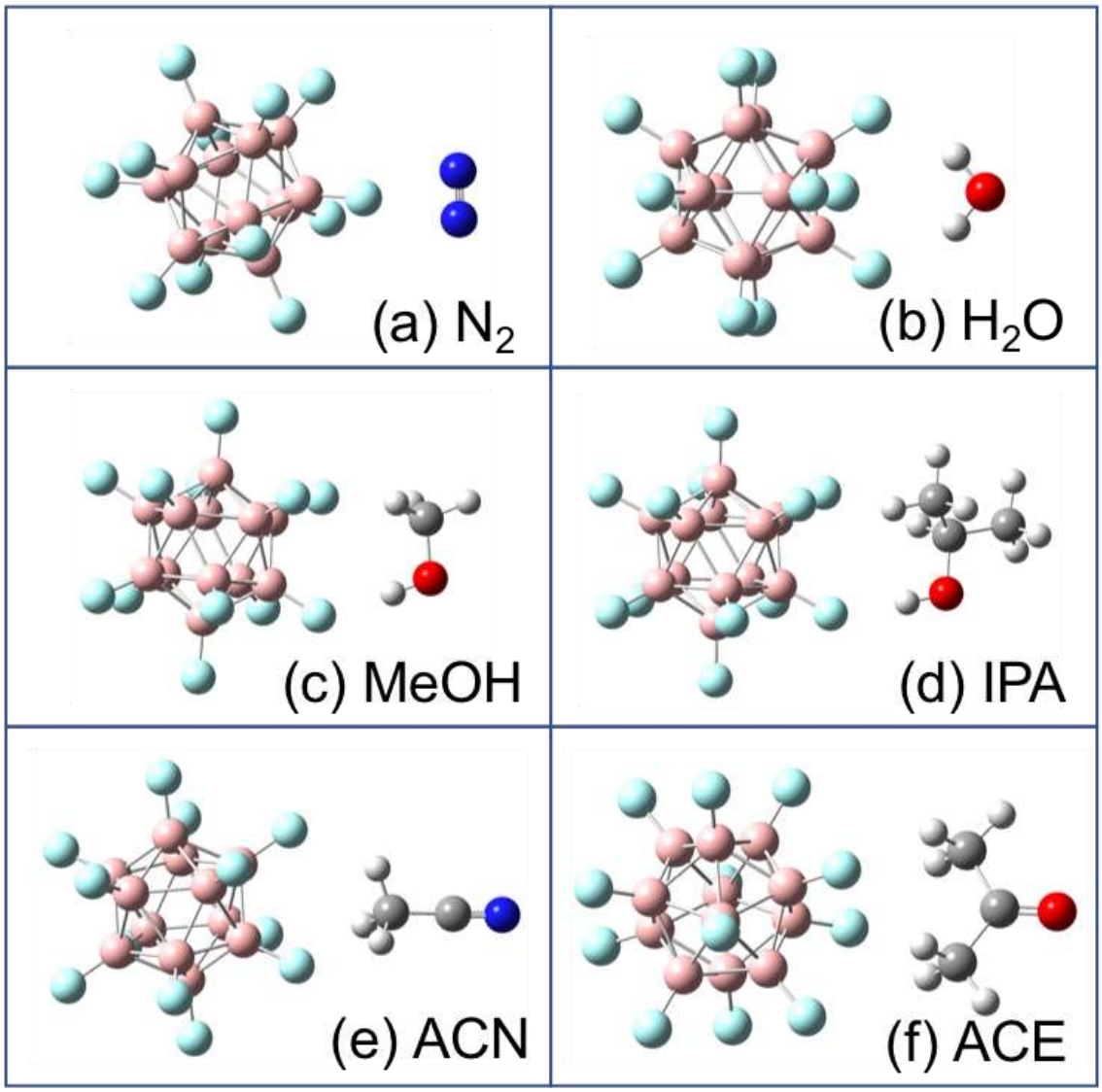

Figure A.1. Optimized geometries of $B_{12}F_{12}^{2-}$ and solvent molecules as determined by DFT calculations.

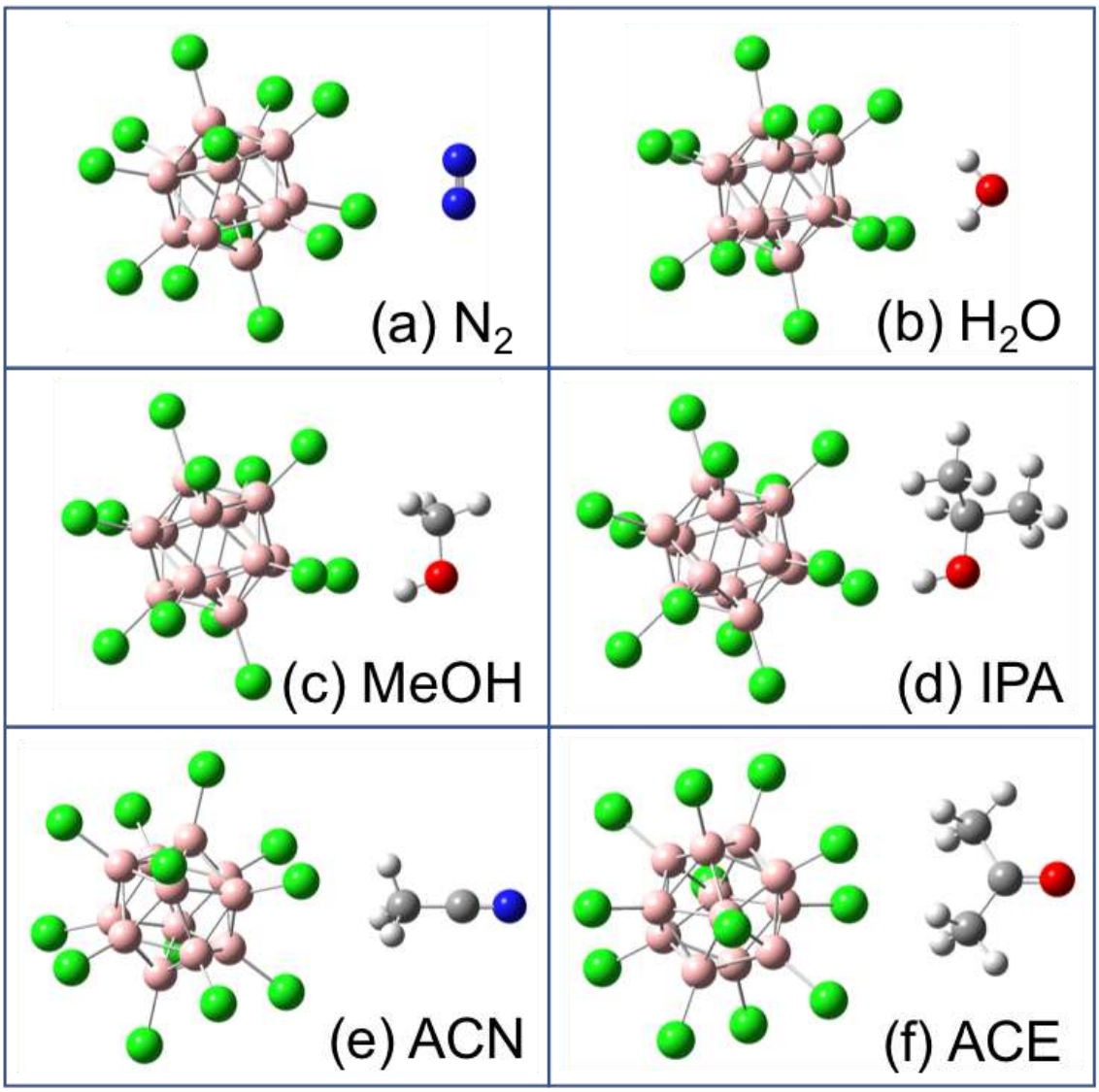

Figure A.2. Optimized geometries of $B_{12}Cl_{12}^{2-}$ and solvent molecules as determined by DFT calculations.

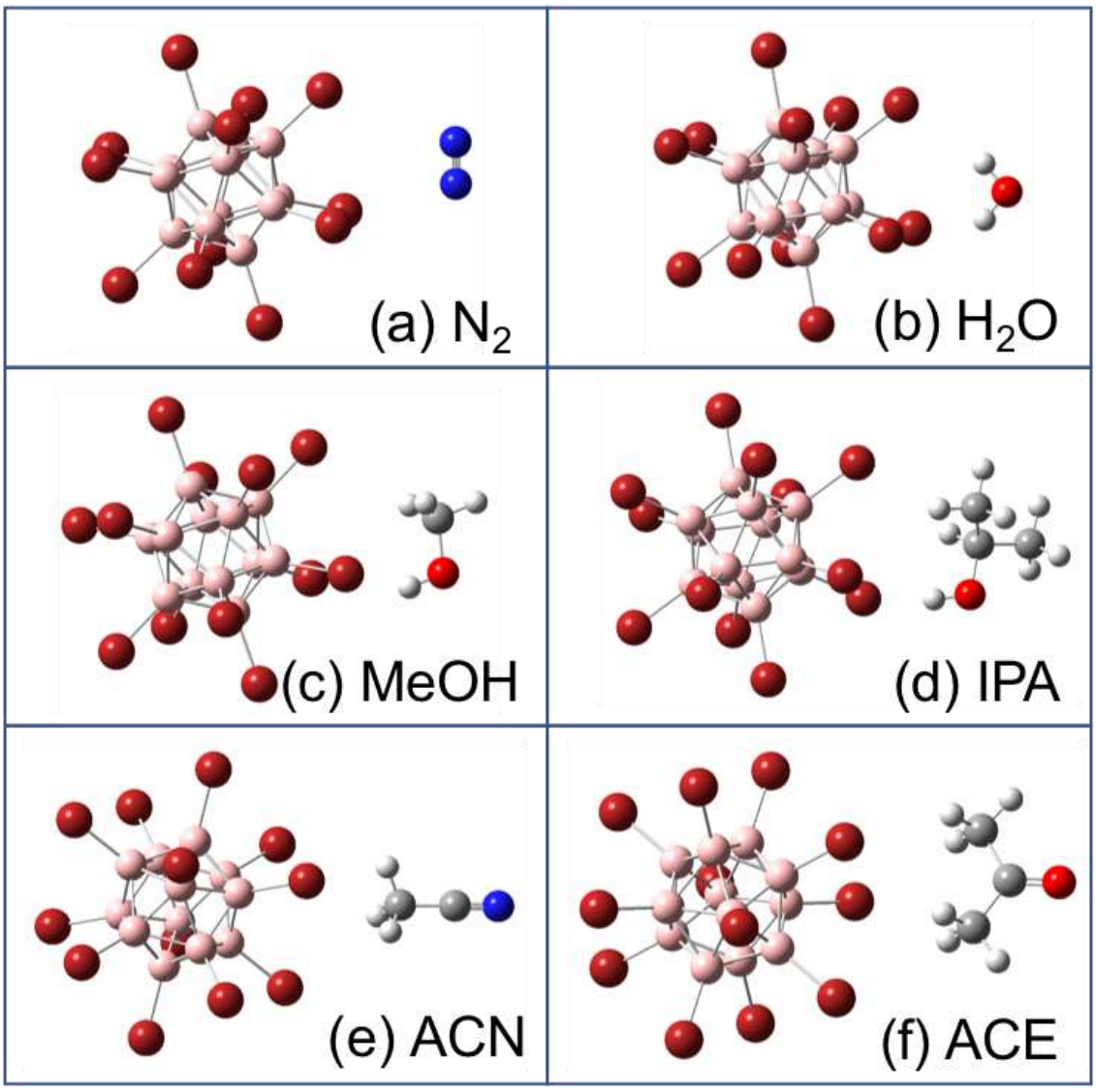

Figure A.3. Optimized geometries of $B_{12}Br_{12}^{2-}$ and solvent molecules as determined by DFT calculations.

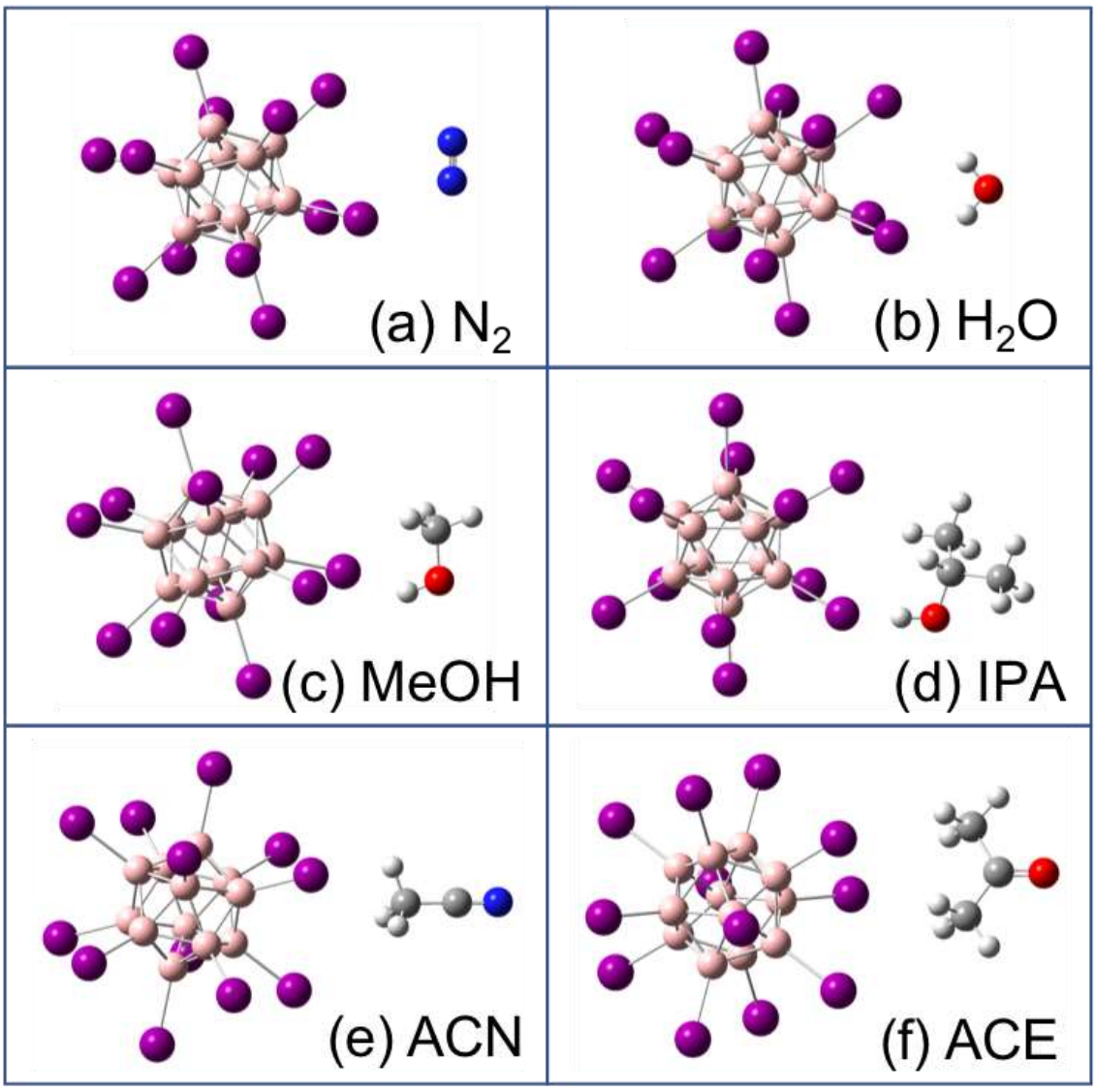

Figure A.4. Optimized geometries of $B_{12}I_{12}^{2-}$ and solvent molecules as determined by DFT calculations.

Appendix A.2

Optimized structures for Chapter 3 given in XYZ coordinate.

$B_{12}H_{12}^{2-}$ + N_2	X (Å)	Y (Å)	Z (Å)
B	-2.141706	-0.529422	0.892298
B	-1.124479	0.828994	-1.443744
B	-0.472202	-0.832080	-1.443859
B	-1.100537	-1.671672	0.000011
B	-0.495513	1.668626	-0.000011
B	-0.472204	-0.832062	1.443870
B	0.559019	-1.018072	0.000007
B	0.544493	0.525850	-0.891679
B	-2.141705	-0.529433	-0.892292
B	-1.124480	0.829013	1.443733
B	0.544493	0.525861	0.891673
B	-2.156225	1.016053	-0.000007
H	-1.354352	1.417002	2.465887
H	-3.117754	1.736386	-0.000012
H	-3.093099	-0.903141	1.523669
H	-3.093098	-0.903161	-1.523659
H	-1.354350	1.416970	-2.465906
H	-1.313924	-2.853942	0.000018
H	-0.239578	-1.419683	-2.465603
H	1.521576	-1.736413	0.000012
H	1.495924	0.899046	-1.523012
H	1.495923	0.899066	1.523002
H	-0.279973	2.850410	-0.000018
H	-0.239580	-1.419651	2.465622
N	4.034796	0.548705	0.000000
N	4.176277	-0.533159	0.000000

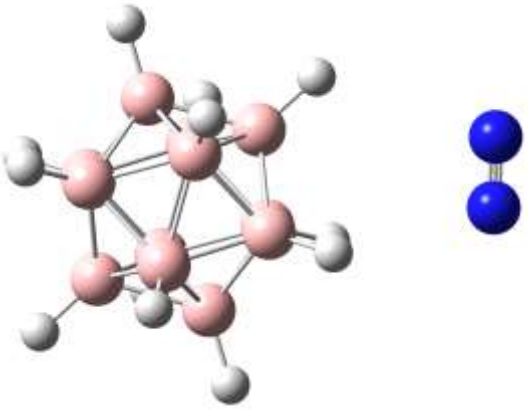

$B_{12}F_{12}^{2-}$ + N_2	X (Å)	Y (Å)	Z (Å)
B	1.050787	-0.090925	0.897705
B	-1.249070	1.441922	-0.001074
B	-1.853213	0.007739	0.898282
B	-0.430885	-0.939541	1.454380
B	-0.370167	0.855321	-1.454887
B	0.448325	-1.526138	0.000532
B	-1.347470	-1.464951	0.000579
B	-1.853286	0.006720	-0.898751
B	-0.370040	0.856992	1.453331
B	1.050726	-0.091936	-0.898316
F	-3.033854	0.048203	1.628152
F	-2.117449	-2.620520	0.001300
F	-0.455050	-1.668166	2.636175
F	-0.343986	1.586896	2.634282
F	-1.939042	2.646941	-0.001765
F	-3.033981	0.046330	-1.628579
F	2.234436	-0.130231	-1.626196
F	-0.344196	1.583837	-2.636700
F	-0.455287	-1.671230	-2.634830
F	1.320797	2.532961	-0.001877
F	2.234554	-0.128482	1.625528
F	1.139301	-2.730341	0.001247
B	-0.430996	-0.941209	-1.453901
B	0.546479	1.380521	-0.001118
N	4.735085	1.046021	0.007957
N	4.863986	-0.036743	-0.001422

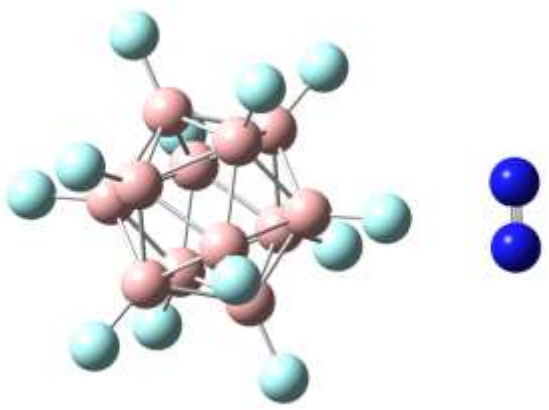

$B_{12}Cl_{12}^{2-}$ + N_2	X (Å)	Y (Å)	Z (Å)
B	0.389855	-0.987512	-1.450789
B	0.390686	-0.993724	1.446225
B	-1.158545	-0.286820	0.894558
B	-1.159058	-0.282982	-0.895207
B	1.714451	0.078278	0.894872
B	0.164230	0.788768	-1.446900
B	-0.792707	1.221072	0.002800
B	0.165061	0.782556	1.450083
B	-0.428274	-1.652372	-0.003466
B	1.713937	0.082117	-0.895603
B	0.982833	1.447602	0.002776
B	1.347871	-1.426654	-0.003492
Cl	0.508175	-1.926826	-2.990837
Cl	-1.178864	-3.296871	-0.006778
Cl	2.484418	-2.832475	-0.006832
Cl	3.239204	0.277938	-1.846100
Cl	0.042227	1.735068	-2.982419
Cl	-2.685690	-0.473376	-1.846283
Cl	-1.932564	2.624699	0.006137
Cl	1.730878	3.093273	0.006091
Cl	0.043939	1.722262	2.989717
Cl	3.240263	0.270022	1.845324
Cl	0.509889	-1.939635	2.982162
Cl	-2.684631	-0.481293	1.845684
N	-5.494533	0.687602	0.003008
N	-5.346134	1.768313	0.005260

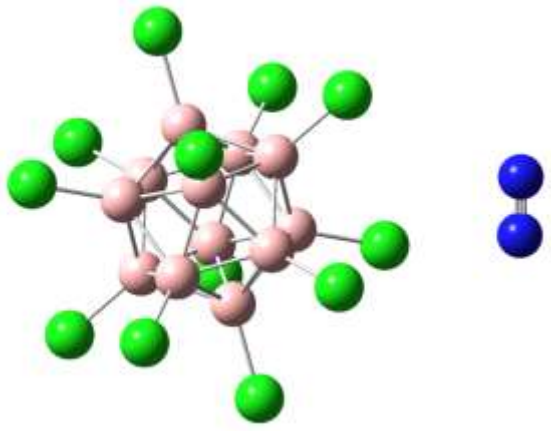

$B_{12}Br_{12}^{2-}$ + N_2	X (Å)	Y (Å)	Z (Å)
B	-0.252320	1.030503	-1.429635
B	1.288002	0.274587	0.906644
B	0.928765	-1.212955	-0.024305
B	-0.023161	-0.746216	-1.468428
B	-0.266363	0.965442	1.468771
B	-1.578016	-0.055530	-0.906651
B	-0.847771	-1.442300	-0.038060
B	-0.037204	-0.811278	1.430020
B	1.296678	0.314783	-0.884046
B	-1.218592	1.432635	0.024677
B	-1.586696	-0.095742	0.884768
B	0.558474	1.661558	0.038426
Br	1.374705	3.459143	0.082732
Br	-2.462897	2.965876	0.053066
Br	2.950133	0.464836	1.957243
Br	-0.406256	1.957032	3.170945
Br	-3.257827	-0.333688	1.909901
Br	0.088783	-1.878651	3.086825
Br	-1.661625	-3.241089	-0.082381
Br	2.176197	-2.743674	-0.052621
Br	-3.239090	-0.246874	-1.957565
Br	0.119098	-1.738198	-3.170161
Br	2.968865	0.551620	-1.908904
Br	-0.375937	2.097503	-3.086876
N	5.863282	-0.773500	0.009461
N	5.719098	-1.854571	-0.015493

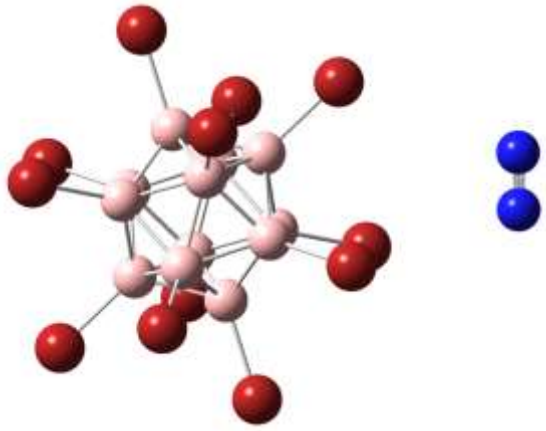

$B_{12}I_{12}^{2-}$ + N_2	X (Å)	Y (Å)	Z (Å)
B	-0.456928	-0.839355	-1.453291
B	-0.456664	-0.834834	1.456026
B	-1.483781	0.531517	0.898395
B	-1.483944	0.528722	-0.899724
B	1.224954	-0.528141	0.899495
B	0.198141	0.835131	-1.455967
B	-0.436422	1.682377	-0.002550
B	0.198405	0.839652	1.453378
B	-1.496413	-1.027139	0.001757
B	1.224791	-0.530934	-0.898021
B	1.237390	1.027193	-0.001683
B	0.178014	-1.682125	0.002623
I	0.575685	-3.850555	0.005955
I	2.973632	-1.215265	-2.053888
I	-0.877443	-1.911385	3.333385
I	2.974004	-1.208878	2.057165
I	3.003033	2.347176	-0.003894
I	0.622271	1.921795	3.326850
I	-0.831228	3.851369	-0.005883
I	-3.230203	1.216632	2.056611
I	0.621667	1.911447	-3.332869
I	-3.230577	1.210236	-2.059746
I	-0.878047	-1.921733	-3.327220
I	-3.258932	-2.351657	0.003975
N	6.273701	-0.545725	0.000313
N	6.399669	0.538050	-0.001365

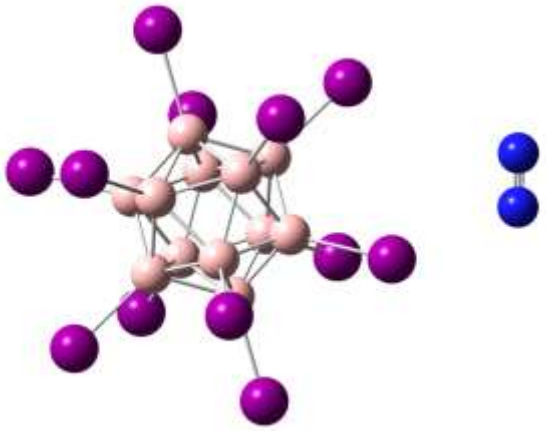

$B_{12}H_{12}^{2-}$ + H_2O	X (Å)	Y (Å)	Z (Å)
B	0.484543	-1.443536	0.873842
B	-0.872408	0.890913	-0.136881
B	-0.209724	-0.000126	-1.531938
B	0.634383	-1.443836	-0.906136
B	0.484547	1.443683	0.873601
B	1.996448	-0.891845	0.104725
B	1.567935	-0.000116	-1.380862
B	0.634387	1.443686	-0.906377
B	-0.872410	-0.890931	-0.136732
B	1.326166	0.000125	1.497549
B	1.996451	0.891860	0.104576
B	-0.451714	0.000115	1.349397
H	1.868850	0.000213	2.568274
H	-1.172353	0.000195	2.307734
H	0.426831	-2.465194	1.501004
H	-1.883951	-1.540902	-0.225559
H	-1.883947	1.540873	-0.225816
H	0.682504	-2.465665	-1.533916
H	-0.758519	-0.000214	-2.598611
H	2.281706	-0.000197	-2.346092
H	0.682511	2.465411	-1.534327
H	3.013704	1.523675	0.189844
H	0.426837	2.465446	1.500594
H	3.013700	-1.523648	0.190098
O	-4.145602	0.000020	0.159723
H	-3.519146	-0.736409	0.109204
H	-3.519144	0.736440	0.109082

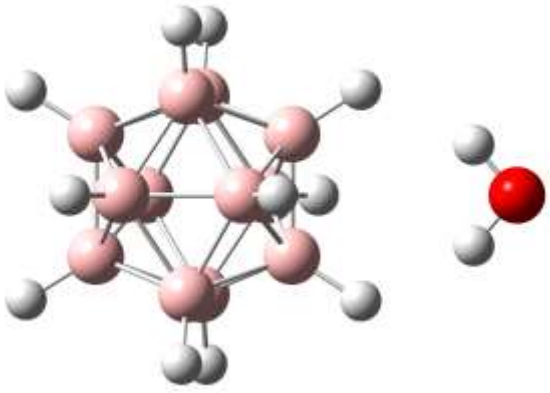

$B_{12}F_{12}^{2-}$ + H_2O	X (Å)	Y (Å)	Z (Å)
B	-1.173007	-0.896475	0.000115
B	1.172672	-0.000289	1.454737
B	0.274570	1.454116	0.899970
B	-1.173001	0.896484	0.000467
B	1.727189	-0.898829	-0.000654
B	-0.625079	0.000289	-1.456063
B	0.274093	1.454469	-0.899584
B	1.727195	0.898818	-0.000302
B	-0.624308	-0.000283	1.456356
B	0.274083	-1.454116	-0.900155
F	0.270068	2.634805	1.627592
F	0.269205	2.635444	-1.626740
F	-2.360036	1.634812	0.000924
F	-1.359592	-0.000511	2.631467
F	1.902578	-0.000523	2.634241
F	2.907143	1.628128	-0.000470
F	0.269186	-2.634806	-1.627774
F	2.907131	-1.628147	-0.001109
F	1.901182	0.000511	-2.635289
F	0.270050	-2.635444	1.626558
F	-2.360048	-1.634794	0.000282
F	-1.360987	0.000522	-2.630784
B	1.171901	0.000282	-1.455399
B	0.274560	-1.454469	0.899399
O	-4.766381	0.000019	0.000841
H	-4.151932	0.745290	0.000903
H	-4.151939	-0.745258	0.000610

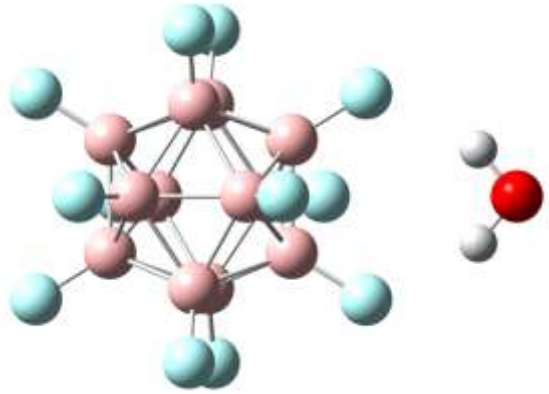

$B_{12}Cl_{12}^{2-}$ + H_2O	X (Å)	Y (Å)	Z (Å)
B	-0.107328	-1.678745	-0.024785
B	1.563905	0.523979	-0.888478
B	1.564301	0.497533	0.902819
B	0.531203	-0.864034	1.436387
B	-0.108565	0.851498	-1.437343
B	-1.139652	-0.535991	0.886711
B	-0.107924	0.808696	1.461853
B	0.531365	1.666648	0.024464
B	1.564516	-1.039943	-0.015723
B	-1.140047	-0.509588	-0.901692
B	-1.137370	1.025447	0.015367
B	0.530562	-0.821250	-1.461550
Cl	-0.451890	-3.452178	-0.050890
Cl	3.000054	-2.136764	-0.032233
Cl	0.865674	-1.686068	-3.011972
Cl	-2.583132	-1.045500	-1.851027
Cl	-2.582320	-1.099704	1.820451
Cl	0.866994	-1.774241	2.960455
Cl	-0.451643	1.673485	3.010218
Cl	-2.570097	2.139376	0.032129
Cl	0.866613	3.441826	0.050598
Cl	-0.452963	1.761616	-2.959352
Cl	2.998881	1.087232	-1.830771
Cl	2.999697	1.032733	1.860694
O	-5.361526	0.047706	0.001864
H	-4.735019	0.781871	0.012555
H	-4.761466	-0.706629	-0.009395

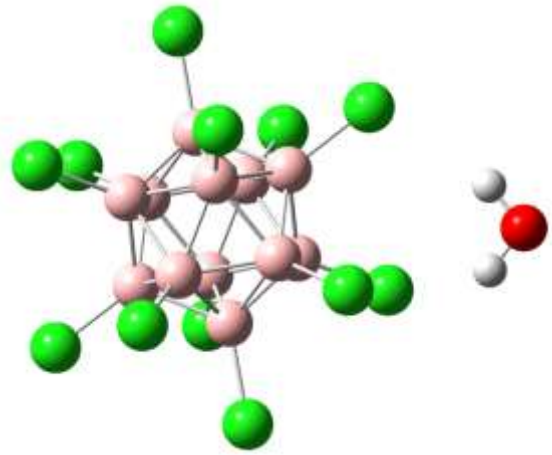

$B_{12}Br_{12}^{2-}$ + H_2O	X (Å)	Y (Å)	Z (Å)
B	-0.191617	-1.673480	0.098964
B	-0.194652	0.918318	1.400131
B	-1.233232	1.025035	-0.054327
B	-1.233606	-0.574460	-0.857400
B	1.477550	0.572510	0.857297
B	0.437403	-0.920469	-1.400616
B	-0.208305	0.748578	-1.495883
B	0.435261	1.671288	-0.100054
B	-1.224909	-0.469686	0.930045
B	1.479410	-1.029230	0.053327
B	1.469112	0.467622	-0.932207
B	0.451149	-0.750846	1.494298
Br	0.829614	-1.619309	3.226027
Br	3.051954	-2.220561	0.115442
Br	-0.564692	1.982767	3.020476
Br	3.048163	1.237359	1.851038
Br	3.029902	1.011288	-2.011427
Br	0.795572	3.608863	-0.215094
Br	-0.594404	1.616933	-3.225756
Br	-2.802477	2.232644	-0.117177
Br	0.799768	-1.985327	-3.022641
Br	-2.810390	-1.236027	-1.845571
Br	-2.791006	-1.011734	2.005505
Br	-0.559028	-3.609462	0.214054
O	-5.697484	-0.022671	0.024173
H	-5.082458	0.716750	-0.055293
H	-5.088402	-0.765553	0.103790

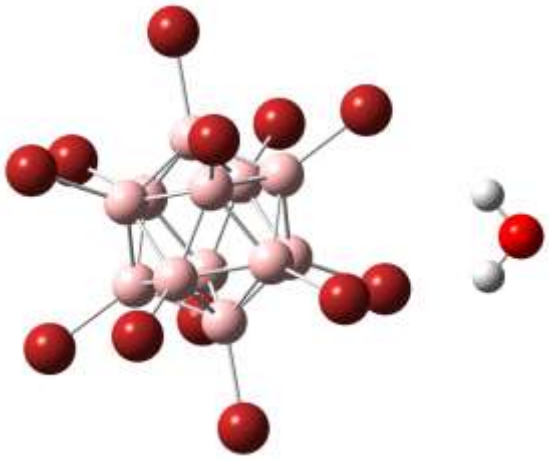

$B_{12}I_{12}^{2-}$ + H_2O	X (Å)	Y (Å)	Z (Å)
B	0.255480	-1.609583	-0.494915
B	0.214027	0.372912	1.635265
B	-1.457068	0.213883	0.991289
B	-1.431490	-1.011335	-0.325181
B	1.258408	0.996760	0.312560
B	-0.384547	-0.385817	-1.646513
B	-1.443089	0.741110	-0.728321
B	-0.426458	1.596633	0.482930
B	-0.407515	-1.239023	1.135263
B	1.286004	-0.226853	-1.002820
B	0.236679	1.226178	-1.147508
B	1.270847	-0.753563	0.715538
I	3.022468	-1.716171	1.650046
I	3.059420	-0.507227	-2.279229
I	0.603134	0.861972	3.748606
I	2.990328	2.304727	0.729141
I	0.655241	2.813955	-2.617251
I	-0.863447	3.663131	1.113158
I	-3.192651	1.704877	-1.659510
I	-3.224685	0.498044	2.276507
I	-0.766877	-0.874885	-3.760997
I	-3.166144	-2.307015	-0.736414
I	0.698616	-3.674656	-1.124118
I	-0.819666	-2.827294	2.606562
O	6.077944	0.022376	0.015884
H	5.477453	-0.731492	-0.010108
H	5.457843	0.760449	0.059795

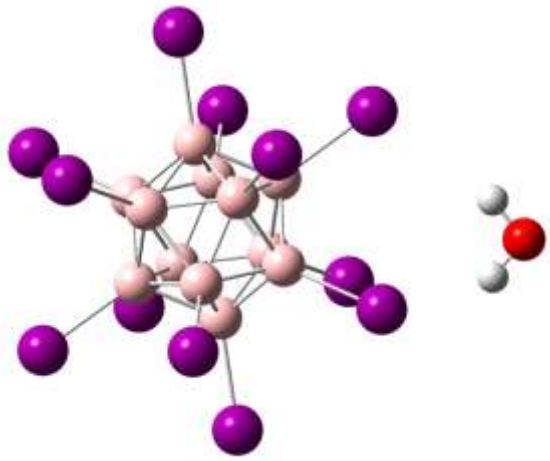

$B_{12}H_{12}^{2-}$ + MeOH	X (Å)	Y (Å)	Z (Å)
B	2.305922	-0.343479	-0.980355
B	0.679125	-1.049542	1.298759
B	-0.363719	-1.022295	-0.144958
B	0.635998	-0.591062	-1.554652
B	1.297395	0.604501	1.554038
B	1.254407	1.062563	-1.297213
B	-0.398395	0.640158	-0.782154
B	-0.371748	0.356707	0.981318
B	1.303188	-1.635883	-0.268886
B	2.302196	1.040832	0.146130
B	0.629288	1.648591	0.269218
B	2.332515	-0.626642	0.781693
H	3.248270	1.772816	0.249534
H	3.299271	-1.074765	1.334796
H	3.253939	-0.591156	-1.674107
H	1.535614	-2.797817	-0.459114
H	0.469838	-1.797121	2.213647
H	0.396168	-1.015326	-2.651247
H	-1.302586	-1.770474	-0.251470
H	-1.364521	1.083934	-1.336663
H	-1.319361	0.598269	1.676773
H	0.388400	2.809271	0.459478
H	1.529360	1.027669	2.653191
H	1.455862	1.809968	-2.214789
C	-4.013014	0.619619	0.000538
H	-5.053484	0.798334	0.293362
H	-3.350179	1.132250	0.702106
H	-3.847290	1.058544	-0.990389
O	-3.805365	-0.780072	0.004467
H	-2.848664	-0.943794	-0.057455

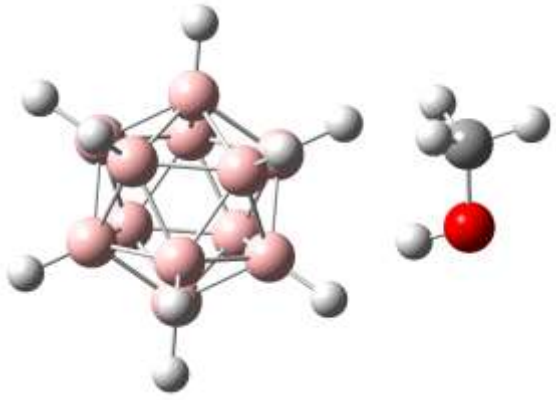

$B_{12}F_{12}^{2-}$ + MeOH	X (Å)	Y (Å)	Z (Å)
B	0.909813	0.804934	1.454985
B	0.663191	-1.702915	0.000033
B	1.808672	-0.649570	-0.899163
B	1.960875	0.899942	-0.000021
B	-0.935695	-0.892928	0.000020
B	0.353316	1.703790	-0.000033
B	0.909807	0.804877	-1.455018
B	0.107593	-0.803739	-1.455589
B	1.808675	-0.649535	0.899183
B	-0.790041	0.650556	0.898978
F	2.864710	-1.176884	-1.627900
F	1.234563	1.457818	-2.635008
F	3.140749	1.629557	-0.000037
F	2.864716	-1.176820	1.627937
F	0.783375	-3.084620	0.000060
F	-0.225045	-1.456917	-2.632802
F	-1.853354	1.171367	1.625862
F	-2.128760	-1.626750	0.000037
F	-1.853361	1.171303	-1.625899
F	-0.225035	-1.456814	2.632862
F	1.234574	1.457921	2.634947
F	0.224954	3.085118	-0.000060
B	-0.790044	0.650521	-0.898998
B	0.107599	-0.803682	1.455622
C	-4.730074	0.664845	0.000000
H	-5.748595	1.063117	0.000011
H	-4.201229	1.037430	0.881877
H	-4.201248	1.037430	-0.881889
O	-4.833164	-0.754098	0.000000
H	-3.930754	-1.104026	0.000005

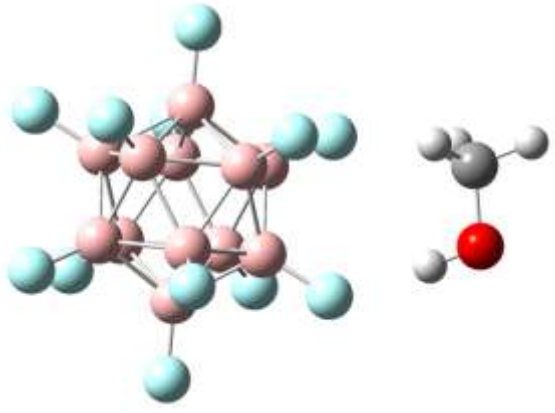

$B_{12}Cl_{12}^{2-}$ + MeOH	X (Å)	Y (Å)	Z (Å)
B	-0.826522	1.197697	0.000009
B	-0.144294	-1.618858	-0.000013
B	0.594170	-0.870064	1.449220
B	0.171895	0.871066	1.449296
B	0.594169	-0.870042	-1.449234
B	0.911973	1.619634	0.000012
B	1.790391	0.341905	0.895757
B	1.594547	-1.196655	-0.000010
B	-1.020601	-0.340045	0.893027
B	0.171893	0.871088	-1.449284
B	1.790390	0.341919	-0.895754
B	-1.020602	-0.340031	-0.893032
Cl	-2.115072	2.466432	0.000020
Cl	-2.523567	-0.707435	1.833505
Cl	-2.523569	-0.707406	-1.833514
Cl	-0.057804	1.793135	-2.986013
Cl	1.470900	3.337847	0.000025
Cl	-0.057801	1.793089	2.986040
Cl	3.283687	0.704378	1.846116
Cl	3.283685	0.704407	-1.846109
Cl	2.879564	-2.466791	-0.000021
Cl	0.813362	-1.793049	-2.986741
Cl	-0.714559	-3.333161	-0.000026
Cl	0.813365	-1.793095	2.986711
C	-5.380193	0.676809	0.000006
H	-6.404614	1.056777	0.000011
H	-4.856665	1.056657	0.881793
H	-4.856669	1.056669	-0.881779
O	-5.461175	-0.742098	-0.000004
H	-4.554033	-1.071720	-0.000007

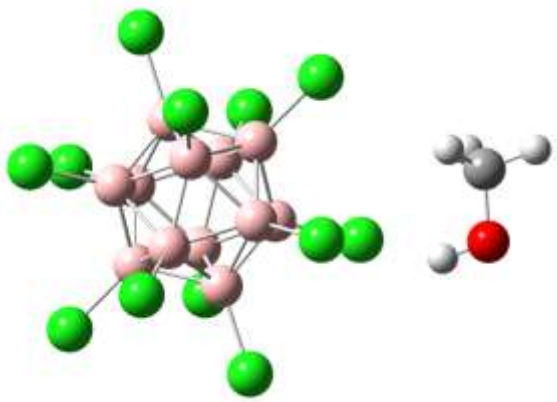

$B_{12}Br_{12}^{2-}$ + MeOH	X (Å)	Y (Å)	Z (Å)
B	-0.362976	-1.635833	-0.058428
B	-0.013474	0.891757	-1.436771
B	1.601163	0.317227	-0.913847
B	1.384917	-1.244611	-0.061859
B	-0.994543	1.193091	0.031440
B	0.402337	-0.943329	1.406291
B	1.616646	0.263765	0.877867
B	0.753057	1.583976	0.028001
B	0.377288	-0.856842	-1.492251
B	-1.209521	-0.368088	0.881405
B	0.011576	0.805265	1.461915
B	-1.224969	-0.314748	-0.906249
Br	-2.878518	-0.653901	-1.935892
Br	-2.845219	-0.768876	1.917393
Br	-0.259455	1.953148	-3.082908
Br	-2.374974	2.604928	0.085496
Br	-0.205399	1.766501	3.172405
Br	1.397986	3.449054	0.078079
Br	3.263819	0.599298	1.912747
Br	3.230394	0.714710	-1.955168
Br	0.638963	-2.005625	3.053092
Br	2.762916	-2.656942	-0.115909
Br	0.584897	-1.818945	-3.203295
Br	-1.016322	-3.497860	-0.108342
C	-5.781018	0.781340	0.060516
H	-6.792028	1.194278	0.081567
H	-5.238027	1.117539	0.948277
H	-5.253251	1.170146	-0.814860
O	-5.909175	-0.633735	0.019401
H	-5.014510	-0.995414	0.000879

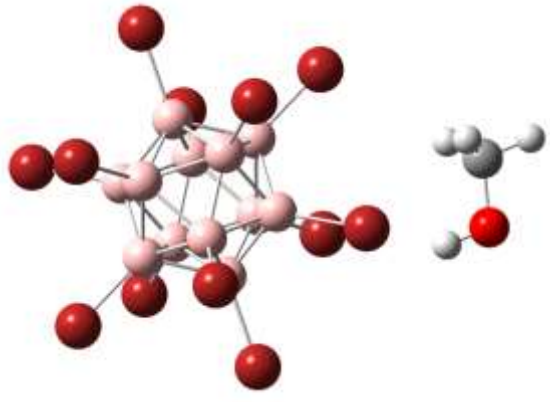

$B_{12}I_{12}^{2-}$ + MeOH	X (Å)	Y (Å)	Z (Å)
B	-1.562163	0.425761	0.875127
B	1.080183	1.184609	-0.073713
B	0.072838	0.777751	-1.505871
B	-1.560824	0.308486	-0.919659
B	1.251950	-0.300643	0.923165
B	-1.388020	-1.177165	0.078771
B	-0.377375	-0.959967	-1.392610
B	1.253286	-0.417720	-0.868584
B	-0.659769	1.633885	-0.104367
B	-0.379540	-0.770248	1.510876
B	0.352213	-1.626782	0.109448
B	0.070673	0.967477	1.397715
I	0.364034	2.208107	3.195654
I	-0.667367	-1.767439	3.455159
I	2.673322	2.705783	-0.171921
I	3.070134	-0.695464	2.108919
I	1.009509	-3.725825	0.247091
I	3.073190	-0.963307	-1.990178
I	-0.662412	-2.201715	-3.191023
I	0.368988	1.773896	-3.449527
I	-2.978379	-2.699691	0.177069
I	-3.374385	0.701315	-2.108762
I	-3.377449	0.969810	2.000307
I	-1.310419	3.735113	-0.242149
C	6.183076	0.644854	-0.034623
H	7.202126	1.036201	-0.059449
H	5.656757	0.960526	-0.940017
H	5.655486	1.075572	0.821257
O	6.282228	-0.770224	0.057882
H	5.381482	-1.116706	0.079842

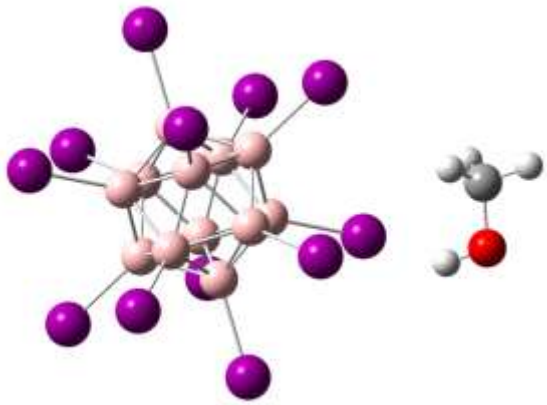

$B_{12}H_{12}^{2-}$ + IPA	X (Å)	Y (Å)	Z (Å)
B	-3.161449	0.373991	0.889233
B	-1.775891	0.244527	-1.639150
B	-1.820633	-1.402775	-0.947839
B	-2.676671	-1.321388	0.614195
B	-0.822800	1.277769	-0.538472
B	-1.724592	-0.287901	1.713484
B	-0.894022	-1.386235	0.578886
B	-0.347201	-0.415737	-0.808879
B	-3.220352	-0.314532	-0.755700
B	-1.680028	1.358481	1.023127
B	-0.281718	0.271040	0.831661
B	-2.604488	1.341590	-0.502956
H	-1.626651	2.333845	1.720529
H	-3.207747	2.306096	-0.885653
H	-4.160723	0.654429	1.492317
H	-4.260606	-0.521717	-1.317603
H	-1.785751	0.430262	-2.824481
H	-3.332641	-2.240017	1.022042
H	-1.862750	-2.376633	-1.647285
H	-0.281766	-2.346184	0.956404
H	0.638683	-0.696845	-1.442419
H	0.754369	0.480796	1.397025
H	-0.161265	2.192487	-0.947846
H	-1.703464	-0.474335	2.898906
C	3.499689	-0.024169	0.199756
H	2.922121	-0.179779	1.118004
C	4.980224	-0.219373	0.500090
H	5.162519	-1.230163	0.869845
H	5.568212	-0.078463	-0.411363
H	5.323385	0.497123	1.250245
C	3.191832	1.376594	-0.319918
H	3.746944	1.561075	-1.244601
H	2.125624	1.478509	-0.518922
H	3.470196	2.134994	0.417747
O	3.146704	-1.019199	-0.754522
H	2.183881	-0.971079	-0.894662

$B_{12}F_{12}^{2-}$ + IPA	X (Å)	Y (Å)	Z (Å)
B	-0.104691	1.035505	-0.805013
B	1.072429	0.180307	1.712154
B	2.402018	0.711511	0.625681
B	1.673905	1.241102	-0.930761
B	0.276998	-1.245566	0.959573
B	0.879585	-0.184664	-1.684085
B	2.429364	-0.385774	-0.798448
B	2.057560	-1.041170	0.834574
B	0.834869	1.591014	0.620994
B	-0.441696	-0.711258	-0.593439
F	3.560811	1.290224	1.121519
F	3.609850	-0.696452	-1.456758
F	2.240465	2.248991	-1.696582
F	0.716727	2.882229	1.113198
F	1.148562	0.329274	3.088872
F	2.936798	-1.882712	1.499469
F	-1.613254	-1.290406	-1.098541
F	-0.299513	-2.250460	1.721389
F	1.224721	-2.886878	-1.086331
F	-1.663646	0.688904	1.477898
F	-0.998072	1.867809	-1.468228
F	0.792879	-0.334503	-3.059762
B	1.116519	-1.595810	-0.592586
B	-0.474677	0.380898	0.826330
C	-4.574990	-0.045575	0.202244
H	-3.878906	-0.140182	1.041468
C	-4.286389	1.273653	-0.506681
H	-3.263350	1.296957	-0.878991
H	-4.971534	1.401569	-1.350095
H	-4.405394	2.116668	0.178700
C	-6.003245	-0.120002	0.723734
H	-6.709244	-0.044669	-0.108203
H	-6.173702	-1.071396	1.230456
H	-6.203604	0.692933	1.424978
O	-4.407790	-1.153685	-0.682680
H	-3.461364	-1.236839	-0.870605

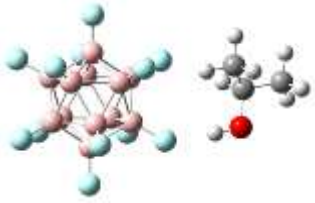

$B_{12}Cl_{12}^{2-}$ + IPA	X (Å)	Y (Å)	Z (Å)
B	-0.598788	0.188879	-1.028556
B	1.038930	1.272982	1.094144
B	2.095298	0.956637	-0.316589
B	1.080808	0.287114	-1.631144
B	0.374596	-0.295119	1.651300
B	0.418011	-1.281167	-1.074003
B	2.085670	-0.807055	-0.631036
B	2.059306	-0.198016	1.053069
B	0.432855	1.573115	-0.564783
B	-0.637713	-0.961973	0.335842
B	1.021720	-1.580791	0.584944
B	-0.627283	0.798803	0.651503
Cl	-2.021616	0.387424	-2.135036
Cl	0.111091	3.242548	-1.175363
Cl	-2.072074	1.649610	1.330066
Cl	-2.102138	-1.970796	0.666854
Cl	0.078998	-2.632050	-2.223786
Cl	1.448674	0.596073	-3.372481
Cl	3.526187	-1.658697	-1.311423
Cl	1.329444	-3.253052	1.194461
Cl	3.472399	-0.403567	2.159525
Cl	-0.006394	-0.603736	3.389962
Cl	1.365307	2.627422	2.244041
Cl	3.546338	1.975426	-0.663220
C	-5.224384	-0.033659	0.152869
H	-4.393570	-0.140265	0.855990
C	-5.265394	1.410970	-0.335828
H	-4.324253	1.669020	-0.818214
H	-6.080918	1.539064	-1.053272
H	-5.413927	2.100841	0.498620
C	-6.517485	-0.448158	0.839456
H	-7.352790	-0.382810	0.136599
H	-6.445066	-1.478277	1.190225
H	-6.729201	0.199911	1.692478
O	-5.033719	-0.934457	-0.940511
H	-4.094949	-0.926120	-1.166392

$B_{12}Br_{12}^{2-}$ + IPA	X (Å)	Y (Å)	Z (Å)
B	-0.847986	0.912844	0.500198
B	1.916930	0.842273	-0.361329
B	0.944067	-0.079399	-1.550633
B	-0.762601	-0.035687	-1.014776
B	1.805657	-0.000744	1.216950
B	-0.875587	-0.876660	0.558960
B	0.232009	-1.491851	-0.707771
B	1.889845	-0.949063	-0.301433
B	0.275352	1.407002	-0.804373
B	0.095335	0.043281	1.749093
B	0.763655	-1.442993	1.002667
B	0.808783	1.455517	0.906199
Br	1.140179	3.162174	1.840679
Br	-0.402113	0.113555	3.657885
Br	3.534766	1.838888	-0.895283
Br	3.295037	0.019464	2.512004
Br	1.041731	-3.093338	2.048613
Br	3.476095	-2.027691	-0.766080
Br	-0.109052	-3.195652	-1.643301
Br	1.429858	-0.150102	-3.462478
Br	-2.502654	-1.869171	1.078595
Br	-2.258755	-0.059599	-2.310615
Br	-0.015206	3.054750	-1.851571
Br	-2.436831	1.991778	0.962702
C	-5.670362	0.023675	0.005175
H	-4.853801	0.068591	0.731441
C	-5.689016	1.326677	-0.787599
H	-4.736540	1.470088	-1.295173
H	-6.488780	1.298735	-1.532855
H	-5.848161	2.182673	-0.127267
C	-6.979056	-0.224652	0.740142
H	-7.800778	-0.311180	0.023892
H	-6.921876	-1.153045	1.309392
H	-7.200530	0.595385	1.426231
O	-5.467657	-1.095220	-0.861827
H	-4.523669	-1.149572	-1.056856

$B_{12}I_{12}^{2-}$ + IPA	X (Å)	Y (Å)	Z (Å)
B	-1.651818	-0.251275	1.052412
B	-0.038334	1.603076	-0.504605
B	-0.686143	0.353646	-1.624662
B	-1.683363	-0.791998	-0.662350
B	1.039199	0.782813	0.677393
B	-0.603688	-1.611787	0.519522
B	-0.007527	-1.238317	-1.135174
B	1.006425	0.241337	-1.034771
B	-1.702611	0.963805	-0.272947
B	0.043863	-0.362550	1.639638
B	1.058915	-0.971604	0.287712
B	-0.635788	1.229118	1.149966
I	-1.038283	2.818841	2.622179
I	0.520009	-0.824464	3.741212
I	0.332297	3.672666	-1.165618
I	2.797233	1.798195	1.537304
I	2.846613	-2.212522	0.639017
I	2.725757	0.558687	-2.383786
I	0.403030	-2.825501	-2.607497
I	-1.151626	0.815742	-3.728777
I	-0.963367	-3.683347	1.179212
I	-3.438158	-1.807323	-1.526081
I	-3.366386	-0.569473	2.399807
I	-3.482462	2.211924	-0.634722
C	6.217608	-0.033522	0.144440
H	5.368884	-0.150954	0.825134
C	7.487518	-0.482587	0.850991
H	7.394321	-1.520574	1.171766
H	8.340743	-0.408571	0.171408
H	7.684871	0.139317	1.726332
C	6.286869	1.423072	-0.302443
H	7.117530	1.560234	-0.999914
H	5.359664	1.709687	-0.796716
H	6.428588	2.087490	0.553340
O	6.043972	-0.901671	-0.978743
H	5.110911	-0.884736	-1.226670

$B_{12}H_{12}^{2-}$ + CAN	X (Å)	Y (Å)	Z (Å)
B	-2.737780	-0.809665	0.636011
B	-1.708282	1.314548	-1.026459
B	-1.073554	-0.232106	-1.651706
B	-1.710440	-1.544868	-0.623409
B	-1.069840	1.547233	0.623980
B	-1.071998	-1.313419	1.027170
B	-0.046471	-0.955011	-0.386624
B	-0.045149	0.810821	-0.635340
B	-2.738735	-0.141729	-1.018602
B	-1.706712	0.233698	1.651254
B	-0.044178	0.143283	1.018126
B	-2.736460	0.957285	0.387082
H	-1.926053	0.398565	2.819695
H	-3.688832	1.634558	0.660970
H	-3.691155	-1.383393	1.086175
H	-3.692751	-0.242641	-1.739979
H	-1.928840	2.244132	-1.752928
H	-1.932476	-2.638708	-1.064733
H	-0.844207	-0.396719	-2.818365
H	0.901617	-1.640877	-0.664083
H	0.904382	1.391508	-1.090974
H	0.905883	0.245448	1.748565
H	-0.837871	2.639369	1.064660
H	-0.841524	-2.241573	1.752557
C	3.358487	-0.007767	-0.006159
H	2.957458	0.789234	-0.631490
H	2.962473	-0.948276	-0.387752
H	2.950698	0.131787	0.994584
C	4.810940	-0.003045	0.001253
N	5.964129	0.000353	0.006919

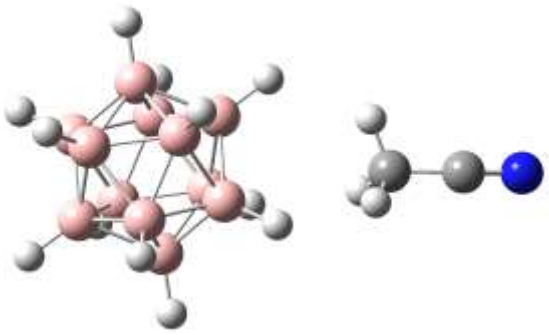

$B_{12}F_{12}^{2-}$ + ACN	X (Å)	Y (Å)	Z (Å)
B	0.642357	0.721513	0.743427
B	-1.032230	0.459346	-1.616126
B	-2.068464	1.007419	-0.253076
B	-1.031126	1.170665	1.206310
B	-0.391139	-1.170396	-1.205647
B	-0.390022	-0.459067	1.616787
B	-2.068401	-0.283191	0.999691
B	-2.069079	-0.722776	-0.744381
B	-0.390102	1.629567	-0.410487
B	0.641735	-1.005012	0.253210
F	-3.170607	1.823507	-0.458323
F	-3.170490	-0.512736	1.809348
F	-1.287245	2.119842	2.184216
F	-0.120953	2.948848	-0.743095
F	-1.289283	0.831692	-2.926902
F	-3.171719	-1.308436	-1.347702
F	1.754964	-1.818815	0.457770
F	-0.122775	-2.118113	-2.182066
F	-1.289114	-2.950607	0.744249
F	1.754715	0.511584	-1.804472
F	1.756070	1.305567	1.345001
F	-0.120801	-0.830837	2.925561
B	-1.032137	-1.629304	0.411138
B	0.641645	0.282825	-0.996931
C	4.274817	-0.002567	-0.004091
H	3.878474	0.704512	0.723961
H	3.882325	0.274112	-0.982064
H	3.882170	-0.988169	0.243814
C	5.728213	-0.000420	-0.001566
N	6.880955	0.001064	0.000234

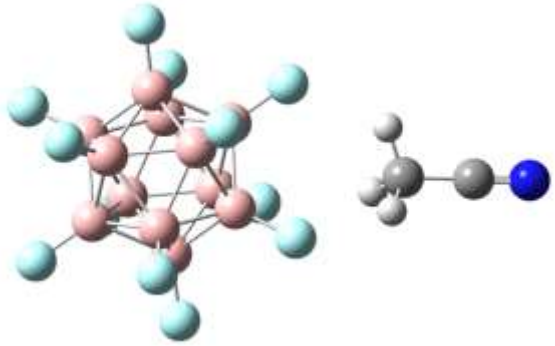

$B_{12}Cl_{12}^{2-}$ + CAN	X (Å)	Y (Å)	Z (Å)
B	0.847071	-0.614196	-0.827917
B	-0.824093	-0.661086	1.535943
B	-1.855646	-1.029088	0.119493
B	-0.821745	-1.000669	-1.342347
B	-0.188018	1.002130	1.340513
B	-0.185618	0.662470	-1.538281
B	-1.857894	0.406512	-0.951845
B	-1.859317	0.616395	0.827132
B	-0.182005	-1.660692	0.195250
B	0.843300	1.028617	-0.121282
B	-0.827753	1.661723	-0.197287
B	0.845556	-0.404374	0.948273
Cl	2.285143	-1.272443	-1.712011
Cl	0.168041	-3.420576	0.403350
Cl	2.282092	-0.838060	1.963578
Cl	2.277981	2.127800	-0.249531
Cl	0.160650	1.363744	-3.166566
Cl	-1.153017	-2.062817	-2.765114
Cl	-3.292751	0.837325	-1.960709
Cl	-1.165226	3.423796	-0.405566
Cl	-3.295671	1.269822	1.705830
Cl	0.155817	2.063028	2.761555
Cl	-1.157769	-1.363004	3.166294
Cl	-3.288158	-2.121681	0.247209
C	5.095954	0.013328	0.010806
H	4.708866	0.423509	-0.920021
H	4.692339	-0.991225	0.122297
H	4.704593	0.618152	0.826617
C	6.549272	0.000432	0.015997
N	7.701200	-0.009221	0.020364

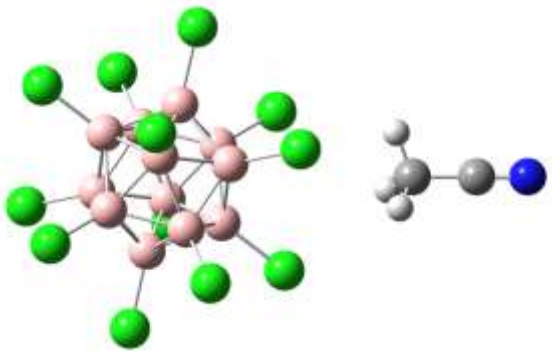

$B_{12}Br_{12}^{2-}$ + ACN	X (Å)	Y (Å)	Z (Å)
B	-0.048552	-1.168238	-1.200658
B	-1.079462	0.719965	0.740663
B	-0.047005	1.622621	-0.410867
B	0.591970	0.454837	-1.611201
B	-0.047919	-0.456839	1.611227
B	1.625394	-0.723117	-0.742101
B	1.626371	1.001592	-0.254018
B	0.592581	1.166114	1.200235
B	-1.079850	0.281144	-0.994309
B	0.591059	-1.624304	0.410585
B	1.625816	-0.283516	0.995637
B	-1.080415	-1.001901	0.253405
Br	-2.648813	-2.170712	0.549288
Br	0.956516	-3.504389	0.886163
Br	-2.646902	1.562032	1.605356
Br	-0.424954	-0.984084	3.475383
Br	3.192763	-0.610662	2.149467
Br	0.959575	2.517867	2.590405
Br	3.194091	2.163269	-0.548385
Br	-0.422832	3.501006	-0.885949
Br	3.192097	-1.560005	-1.601757
Br	0.958565	0.982599	-3.477070
Br	-2.647459	0.610291	-2.155108
Br	-0.425887	-2.518741	-2.589532
C	-5.578505	0.002346	0.002528
H	-5.189499	0.991548	-0.232249
H	-5.191279	-0.283542	0.978898
H	-5.176410	-0.694661	-0.730586
C	-7.032170	-0.005460	-0.007825
N	-8.184001	-0.011437	-0.015857

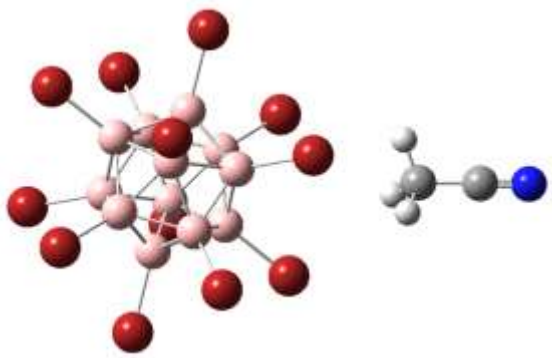

$B_{12}I_{12}^{2-}$ + CAN	X (Å)	Y (Å)	Z (Å)
B	-1.529702	0.878806	-0.553162
B	0.149648	-1.485945	-0.787639
B	-0.492508	-1.424310	0.891265
B	-1.530112	0.037043	1.036200
B	1.185943	-0.038925	-1.037176
B	-0.492274	1.483732	0.785140
B	0.149214	0.060285	1.678239
B	1.185556	-0.879459	0.549954
B	-1.529754	-0.918461	-0.487596
B	0.149936	1.422652	-0.893788
B	1.185593	0.915275	0.484555
B	-0.491811	-0.062222	-1.680269
I	-0.901977	-0.141124	-3.843805
I	0.568683	3.255551	-2.043004
I	0.568270	-3.397837	-1.800184
I	2.935667	-0.088294	-2.382115
I	2.934807	2.105004	1.115262
I	2.934955	-2.019892	1.265336
I	0.567055	0.138994	3.840409
I	-0.903422	-3.258375	2.041304
I	-0.903384	3.396735	1.798364
I	-3.280466	0.085962	2.373477
I	-3.279369	2.013011	-1.264947
I	-3.279682	-2.101306	-1.114765
C	6.041659	0.000254	0.005468
H	5.658689	-0.911989	-0.448951
H	5.654544	0.054412	1.021667
H	5.636672	0.844397	-0.550223
C	7.495323	0.017627	-0.002169
N	8.646883	0.030961	-0.008251

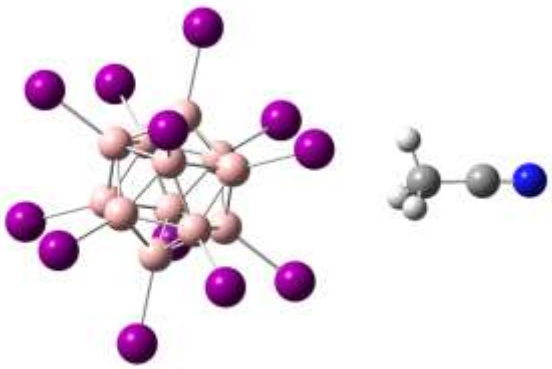

$B_{12}H_{12}^{2-}$ + ACE	X (Å)	Y (Å)	Z (Å)
B	2.480555	-1.491607	0.000001
B	2.642259	1.392904	0.000004
B	1.722364	0.892196	1.443531
B	1.622238	-0.890717	1.443580
B	1.722363	0.892199	-1.443523
B	0.699568	-1.390205	0.000002
B	0.237018	0.081492	0.891574
B	0.860359	1.492624	0.000005
B	3.112149	-0.080314	0.891819
B	1.622238	-0.890714	-1.443575
B	0.237018	0.081494	-0.891567
B	3.112148	-0.080312	-0.891813
H	1.580916	-1.519604	-2.464982
H	4.131207	-0.137210	-1.523352
H	3.052089	-2.546949	0.000000
H	4.131207	-0.137213	1.523357
H	3.328604	2.377493	0.000005
H	1.580917	-1.519608	2.464986
H	1.752000	1.521405	2.465131
H	-0.774911	0.137921	1.537347
H	0.278394	2.543303	0.000006
H	-0.774912	0.137924	-1.537339
H	1.751999	1.521410	-2.465121
H	0.004706	-2.369809	0.000001
C	-3.947660	-0.008450	0.000004
C	-3.193174	1.293610	0.000005
H	-3.887317	2.132381	0.000006
H	-2.519528	1.337181	0.858600
H	-2.519528	1.337182	-0.858589
C	-3.109991	-1.256966	0.000003
H	-2.433092	-1.258654	0.857007
H	-3.746506	-2.140121	0.000002
H	-2.433092	-1.258652	-0.857001
O	-5.168699	-0.046591	0.000004

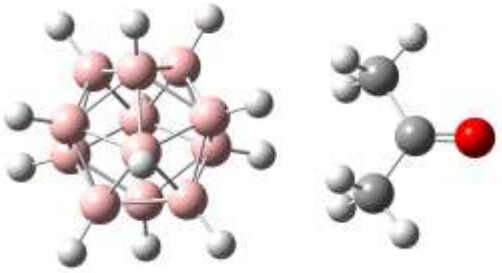

$B_{12}F_{12}^{2-}$ + ACE	X (Å)	Y (Å)	Z (Å)
B	-0.523863	0.120095	0.897529
B	0.836949	-0.905334	-1.454422
B	1.680700	-1.540204	-0.000259
B	0.836944	-0.905850	1.454127
B	0.997850	0.887030	-1.454141
B	0.997845	0.886514	1.454483
B	2.364174	-0.139800	0.898785
B	2.364178	-0.139481	-0.898804
B	-0.108354	-1.376327	-0.000232
B	0.150214	1.519592	0.000283
F	2.301387	-2.780239	-0.000477
F	3.539606	-0.245181	1.627002
F	0.763670	-1.630407	2.634388
F	-0.957829	-2.475590	-0.000429
F	0.763677	-1.629471	-2.634940
F	3.539613	-0.244603	-1.627053
F	-0.487836	2.752408	0.000500
F	1.056370	1.612418	-2.634668
F	2.772861	2.469719	0.000456
F	-1.703014	0.222744	-1.635661
F	-1.703024	0.222160	1.635755
F	1.056363	1.611481	2.635269
B	1.940747	1.360350	0.000257
B	-0.523858	0.120413	-0.897463
C	-4.979101	0.022716	-0.000036
C	-4.250186	1.341653	0.000234
H	-4.962563	2.164565	0.000378
H	-3.586083	1.399425	0.864501
H	-3.586043	1.399760	-0.863980
C	-4.117630	-1.211314	-0.000279
H	-3.449647	-1.203375	0.862678
H	-4.737768	-2.105412	-0.000435
H	-3.449682	-1.203052	-0.863259
O	-6.197663	-0.038087	-0.000058

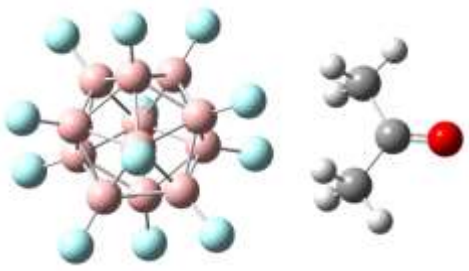

$B_{12}Cl_{12}^{2-}$ + ACE	X (Å)	Y (Å)	Z (Å)
B	0.721435	0.228237	0.892455
B	-1.823309	1.284286	0.010520
B	-2.132213	-0.244688	0.892024
B	-0.557038	-0.897109	1.437917
B	-0.852688	0.897467	-1.442574
B	0.416290	-1.281671	-0.015250
B	-1.349979	-1.575927	-0.016277
B	-2.133920	-0.228196	-0.898408
B	-0.849927	0.870783	1.454389
B	0.719731	0.244707	-0.895568
B	-0.559800	-0.870423	-1.459228
B	-0.056265	1.576396	0.011526
Cl	2.230933	0.471216	1.865918
Cl	-0.998594	1.793290	3.000137
Cl	0.642792	3.242464	0.026207
Cl	2.227374	0.505603	-1.867265
Cl	1.614029	-2.636844	-0.028875
Cl	-0.394103	-1.847530	2.965215
Cl	-2.032007	-3.248317	-0.031031
Cl	-0.399794	-1.792546	-3.004083
Cl	-3.650051	-0.470774	-1.849570
Cl	-1.004286	1.848289	-2.970780
Cl	-3.009602	2.646289	0.024197
Cl	-3.646532	-0.504772	1.841445
C	5.977824	-0.031287	-0.009033
C	5.025029	-1.195719	-0.018860
H	5.574414	-2.134520	-0.028026
H	4.357866	-1.150636	0.843955
H	4.356238	-1.134761	-0.879437
C	5.353380	1.342206	0.004198
H	4.697696	1.448971	0.870126
H	6.128062	2.106398	0.010519
H	4.696097	1.464893	-0.858402
O	7.186891	-0.181947	-0.011554

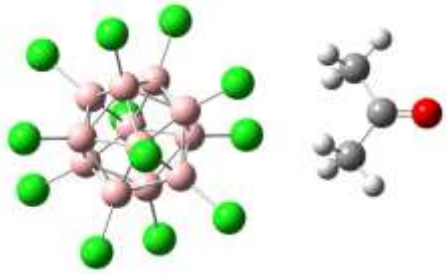

$B_{12}Br_{12}^{2-}$ + ACE	X (Å)	Y (Å)	Z (Å)
B	0.187460	1.591405	0.003648
B	-0.259268	-0.877058	-1.452660
B	-1.849244	-0.266517	-0.896724
B	-1.573582	1.259233	0.003195
B	0.724909	-1.257464	-0.004104
B	-0.591303	0.877050	1.451656
B	-1.848801	-0.271309	0.895078
B	-1.035518	-1.591219	-0.004561
B	-0.592021	0.884804	-1.447774
B	0.996494	0.266113	0.894541
B	-0.258550	-0.884813	1.446954
B	0.996051	0.270898	-0.894721
Br	2.638826	0.587534	-1.951660
Br	2.639792	0.577093	1.952346
Br	-0.062372	-1.892035	-3.133734
Br	2.063357	-2.710376	-0.008320
Br	-0.060824	-1.908767	3.122477
Br	-1.739548	-3.434751	-0.009317
Br	-3.497511	-0.586135	1.932929
Br	-3.498468	-0.575790	-1.935428
Br	-0.780320	1.892381	3.133458
Br	-2.902742	2.717904	0.007425
Br	-0.781868	1.909115	-3.124029
Br	0.906344	3.429836	0.008387
C	6.528978	-0.037178	-0.002275
C	5.930880	1.348421	0.001573
H	6.719474	2.098106	0.003392
H	5.277344	1.478420	-0.862989
H	5.277753	1.473792	0.867126
C	5.553066	-1.182358	-0.005102
H	4.886513	-1.114511	-0.867089
H	6.082637	-2.132369	-0.007772
H	4.886932	-1.119125	0.857559
O	7.734373	-0.210857	-0.003030

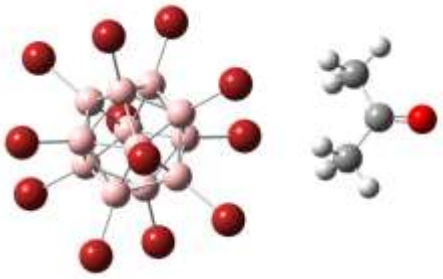

$B_{12}I_{12}^{2-}$ + ACE	X (Å)	Y (Å)	Z (Å)
B	0.450618	0.882404	1.449639
B	0.841149	-1.614911	0.007752
B	1.687981	-0.311630	-0.897223
B	1.445821	1.231970	-0.006222
B	-0.917205	-1.240365	0.004395
B	-0.313042	1.605589	-0.009575
B	0.453023	0.867612	-1.460096
B	0.079242	-0.892155	-1.451552
B	1.686495	-0.302489	0.900827
B	-1.156159	0.301479	0.894085
B	-1.154675	0.292351	-0.901321
B	0.076837	-0.877362	1.458370
I	-0.169198	-2.001324	3.337766
I	-2.985257	0.699459	2.065091
I	1.580998	-3.690363	0.018915
I	-2.446389	-2.828570	0.011205
I	-2.981831	0.678390	-2.079335
I	-0.163695	-2.035171	-3.319827
I	0.693523	1.991755	-3.340210
I	3.521821	-0.707528	-2.052786
I	-1.065420	3.677030	-0.020727
I	2.966628	2.826323	-0.013070
I	0.688020	2.025608	3.318620
I	3.518419	-0.686602	2.063385
C	-7.070036	-0.027303	-0.006858
C	-6.077392	-1.158335	-0.000288
H	-6.592137	-2.116302	0.004161
H	-5.412302	-1.088041	-0.863599
H	-5.413723	-1.079256	0.863356
C	-6.490445	1.366359	-0.013471
H	-5.838871	1.498583	-0.879525
H	-7.288057	2.106210	-0.017886
H	-5.840285	1.507389	0.852256
O	-8.272205	-0.217593	-0.006877

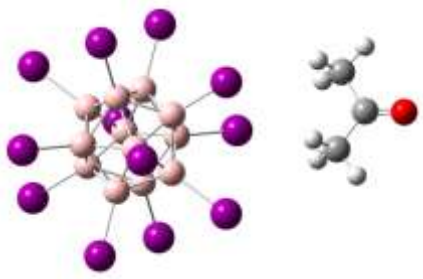

Appendix A.3

Thermochemical data for Chapter 3: Thermochemical data for the solvent, $B_{12}X_{12}^{2-}$, and $B_{12}X_{12}^{2-}$ + solvent species as calculated at the B3LYP/DEF2-TZVPP level of theory at a temperature of four varies temperatures and a pressure of P = 1 atm.

Species	Temp. (ºC)	Electronic Structure (Hartree)	Zero-point Corrected Energy (Hartree)	Enthalpy (Hartree)	Gibbs Free Energy (Hartree)	Entropy (Cal/Mol*K)
N_2	25	-109.5732618	-109.567674	-109.56437	-109.586099	45.733
	150			-109.562982	-109.595466	48.173
	225			-109.562144	-109.601294	49.317
	300			-109.561298	-109.607249	50.309
H_2O	25	-76.4666816	-76.445369	-76.44159	-76.463008	45.08
	150			-76.43998	-76.472285	47.907
	225			-76.438991	-76.478094	49.257
	300			-76.437981	-76.484053	50.442
MeOH	25	-115.7797156	-115.728667	-115.724368	-115.751443	56.985
	150			-115.721975	-115.763221	61.166
	225			-115.720298	-115.77067	63.452
	300			-115.718447	-115.778384	65.621
IPA	25	-194.4534905	-194.34575	-194.339372	-194.373125	71.038
	150			-194.334537	-194.388126	79.469
	225			-194.331017	-194.397912	84.267
	300			-194.32708	-194.408262	88.882
ACN	25	-132.8123854	-132.767218	-132.762665	-132.791226	60.112
	150			-132.759951	-132.803686	64.857
	225			-132.758079	-132.811592	67.409
	300			-132.756041	-132.819793	69.798
ACE	25	-193.245011	-193.161671	-193.155358	-193.18995	72.806
	150			-193.151087	-193.205208	80.258
	225			-193.148034	-193.215051	84.42
	300			-193.144649	-193.22538	88.388

Species	Temp. (ºC)	Electronic Structure (Hartree)	Zero-point Corrected Energy (Hartree)	Enthalpy (Hartree)	Gibbs Free Energy (Hartree)	Entropy (Cal/Mol*K)
$B_{12}H_{12}^{2-}$	25	-305.8262368	-305.660165	-305.651322	-305.690992	83.492
	150			-305.63977	-305.709601	103.556
	225			-305.630887	-305.722704	115.661
	300			-305.62092	-305.737231	127.343
$B_{12}F_{12}^{2-}$	25	-1497.918907	-1497.830077	-1497.808495	-1497.875544	141.117
	150			-1497.790168	-1497.906923	173.14
	225			-1497.777673	-1497.92865	190.183
	300			-1497.764382	-1497.952326	205.769
$B_{12}Cl_{12}^{2-}$	25	-5821.978525	-5821.904846	-5821.878976	-5821.958251	166.848
	150			-5821.85891	-5821.995087	201.944
	225			-5821.845531	-5822.020333	220.195
	300			-5821.831475	-5822.047653	236.68
$B_{12}Br_{12}^{2-}$	25	-31189.42421	-31189.35794	-31189.3285	-31189.42144	195.614
	150			-31189.30764	-31189.46416	232.116
	225			-31189.29391	-31189.49304	250.851
	300			-31189.27956	-31189.52405	267.674
$B_{12}I_{12}^{2-}$	25	-3872.782427	-3872.721295	-3872.689636	-3872.792091	215.634
	150			-3872.668214	-3872.838913	253.138
	225			-3872.654218	-3872.870331	272.234
	300			-3872.639657	-3872.903908	289.313

Species	Temp. (°C)	Electronic Structure (Hartree)	Zero-point Corrected Energy (Hartree)	Enthalpy (Hartree)	Gibbs Free Energy (Hartree)	Entropy (Cal/Mol*K)
$B_{12}H_{12}^{2-}$ + N_2	25	-415.4042373	-415.231833	-415.21886	-415.271159	110.072
	150			-415.205343	-415.295427	133.59
	225			-415.195273	-415.31222	147.315
	300			-415.184111	-415.330615	160.399
$B_{12}F_{12}^{2-}$ + N_2	25	-1607.496508	-1607.40159	-1607.375695	-1607.458066	173.366
	150			-1607.355402	-1607.496232	208.844
	225			-1607.34172	-1607.522326	227.507
	300			-1607.327233	-1607.550549	244.496
$B_{12}Cl_{12}^{2-}$ + N_2	25	-5931.555917	-5931.476121	-5931.446014	-5931.538365	194.369
	150			-5931.423978	-5931.581049	232.928
	225			-5931.409408	-5931.610098	252.804
	300			-5931.394155	-5931.6414	270.695
$B_{12}Br_{12}^{2-}$ + N_2	25	-31299.00138	-31298.92903	-31298.89533	-31299.00129	223.026
	150			-31298.87249	-31299.04984	262.998
	225			-31298.85757	-31299.08252	283.359
	300			-31298.84203	-31299.11749	301.589
$B_{12}I_{12}^{2-}$ + N_2	25	-3982.359279	-3982.29207	-3982.256148	-3982.371636	243.066
	150			-3982.232754	-3982.424288	284.035
	225			-3982.217567	-3982.459499	304.757
	300			-3982.201807	-3982.497048	323.242

Species	Temp. (ºC)	Electronic Structure (Hartree)	Zero-point Corrected Energy (Hartree)	Enthalpy (Hartree)	Gibbs Free Energy (Hartree)	Entropy (Cal/Mol*K)
$B_{12}H_{12}^{2-}$ + H_2O	25	-382.3176791	-382.127114	-382.114934	-382.162955	101.069
	150			-382.101263	-382.185452	124.848
	225			-382.091036	-382.201213	138.788
	300			-382.079679	-382.218603	152.1
$B_{12}F_{12}^{2-}$ + H_2O	25	-1574.408797	-1574.295467	-1574.270641	-1574.345916	158.429
	150			-1574.250182	-1574.381131	194.19
	225			-1574.23633	-1574.405487	213.084
	300			-1574.221637	-1574.432	230.315
$B_{12}Cl_{12}^{2-}$ + H_2O	25	-5898.464526	-5898.367324	-5898.337563	-5898.426526	187.237
	150			-5898.315255	-5898.467835	226.267
	225			-5898.300476	-5898.496105	246.43
	300			-5898.284986	-5898.526662	264.597
$B_{12}Br_{12}^{2-}$ + H_2O	25	-31265.90913	-31265.81951	-31265.7861	-31265.8888	216.163
	150			-31265.76298	-31265.93604	256.634
	225			-31265.74784	-31265.96797	277.291
	300			-31265.73205	-31266.00223	295.805
$B_{12}I_{12}^{2-}$ + H_2O	25	-3949.266011	-3949.181752	-3949.146928	-3949.256766	231.174
	150			-3949.123629	-3949.307028	271.971
	225			-3949.108456	-3949.340795	292.672
	300			-3949.092687	-3949.376901	311.169

Species	Temp. (ºC)	Electronic Structure (Hartree)	Zero-point Corrected Energy (Hartree)	Enthalpy (Hartree)	Gibbs Free Energy (Hartree)	Entropy (Cal/Mol*K)
$B_{12}H_{12}^{2-}$ + MeOH	25	-421.6290361	-421.410052	-421.396343	-421.449475	111.825
	150			-421.381784	-421.474267	137.147
	225			-421.370832	-421.491555	152.073
	300			-421.358609	-421.510594	166.4
$B_{12}F_{12}^{2-}$ + MeOH	25	-1613.71962	-1613.577878	-1613.551406	-1613.631481	168.531
	150			-1613.530054	-1613.668862	205.845
	225			-1613.515479	-1613.69467	225.722
	300			-1613.499923	-1613.722754	243.964
$B_{12}Cl_{12}^{2-}$ + MeOH	25	-5937.776866	-5937.650698	-5937.619797	-5937.711777	193.587
	150			-5937.596634	-5937.754496	234.1
	225			-5937.581142	-5937.783759	255.232
	300			-5937.564793	-5937.815428	274.406
$B_{12}Br_{12}^{2-}$ + MeOH	25	-31305.22171	-31305.10304	-31305.06853	-31305.17406	222.099
	150			-31305.04457	-31305.22262	264.036
	225			-31305.02872	-31305.25549	285.658
	300			-31305.01208	-31305.29082	305.175
$B_{12}I_{12}^{2-}$ + MeOH	25	-3988.57878	-3988.465328	-3988.428595	-3988.543574	241.993
	150			-3988.404059	-3988.596205	284.944
	225			-3988.387941	-3988.631601	306.933
	300			-3988.37108	-3988.669486	326.71

Species	Temp. (ºC)	Electronic Structure (Hartree)	Zero-point Corrected Energy (Hartree)	Enthalpy (Hartree)	Gibbs Free Energy (Hartree)	Entropy (Cal/Mol*K)
$B_{12}H_{12}^{2-}$ + IPA	25	-500.3050614	-500.029647	-500.013644	-500.072539	123.956
	150			-499.996642	-500.100171	153.527
	225			-499.983846	-500.119568	170.965
	300			-499.969536	-500.141011	187.738
$B_{12}F_{12}^{2-}$ + IPA	25	-1692.39543	-1692.197405	-1692.16857	-1692.254416	180.678
	150			-1692.144762	-1692.294642	222.264
	225			-1692.128338	-1692.322564	244.663
	300			-1692.110688	-1692.353059	265.358
$B_{12}Cl_{12}^{2-}$ + IPA	25	-6016.452895	-6016.2703	-6016.237105	-6016.334098	204.139
	150			-6016.211488	-6016.379344	248.922
	225			-6016.194148	-6016.41053	272.573
	300			-6016.175708	-6016.444419	294.197
$B_{12}Br_{12}^{2-}$ + IPA	25	-31383.89755	-31383.72249	-31383.69	-31383.80	232.79
	150			-31383.65924	-31383.84738	279
	225			-31383.64154	-31383.88219	303.144
	300			-31383.62281	-31383.91976	325.112
$B_{12}I_{12}^{2-}$ + IPA	25	-4067.254368	-4067.084581	-4067.045489	-4067.165831	253.281
	150			-4067.018493	-4067.221138	300.512
	225			-4067.000525	-4067.258545	325.023
	300			-4066.98157	-4067.298741	347.253

Species	Temp. (ºC)	Electronic Structure (Hartree)	Zero-point Corrected Energy (Hartree)	Enthalpy (Hartree)	Gibbs Free Energy (Hartree)	Entropy (Cal/Mol*K)
$B_{12}H_{12}^{2-}$ + ACN	25	-438.6681573	-438.455968	-438.441536	-438.497233	117.224
	150			-438.426507	-438.523187	143.371
	225			-438.415286	-438.541242	158.665
	300			-438.40281	-438.561087	173.289
$B_{12}F_{12}^{2-}$ + ACN	25	-1630.759774	-1630.624668	-1630.597622	-1630.678921	171.106
	150			-1630.575831	-1630.716896	209.192
	225			-1630.561003	-1630.743125	229.416
	300			-1630.545208	-1630.771667	247.937
$B_{12}Cl_{12}^{2-}$ + ACN	25	-5954.81536	-5954.695743	-5954.664173	-5954.759211	200.024
	150			-5954.64062	-5954.803284	241.222
	225			-5954.624897	-5954.833419	262.67
	300			-5954.608329	-5954.865993	282.102
$B_{12}Br_{12}^{2-}$ + ACN	25	-31322.25958	-31322.1474	-31322.11226	-31322.22064	228.086
	150			-31322.08792	-31322.27046	270.697
	225			-31322.07184	-31322.30414	292.63
	300			-31322.05498	-31322.34032	312.401
$B_{12}I_{12}^{2-}$ + ACN	25	-4005.615878	-4005.508928	-4005.471514	-4005.589797	248.948
	150			-4005.446596	-4005.643885	292.568
	225			-4005.430253	-4005.68021	314.865
	300			-4005.413177	-4005.71906	334.894

Species	Temp. (ºC)	Electronic Structure (Hartree)	Zero-point Corrected Energy (Hartree)	Enthalpy (Hartree)	Gibbs Free Energy (Hartree)	Entropy (Cal/Mol*K)
$B_{12}H_{12}^{2-}$ + ACE	25	-499.0988913	-498.84808	-498.832057	-498.89165	125.424
	150			-498.815514	-498.919499	154.205
	225			-498.803134	-498.938944	171.077
	300			-498.789332	-498.960366	187.255
$B_{12}F_{12}^{2-}$ + ACE	25	-1691.19026	-1691.016367	-1690.987842	-1691.072679	178.553
	150			-1690.964547	-1691.112397	219.254
	225			-1690.948563	-1691.139923	241.052
	300			-1690.931443	-1691.169949	261.127
$B_{12}Cl_{12}^{2-}$ + ACE	25	-6015.246298	-6015.087992	-6015.054918	-6015.153178	206.804
	150			-6015.029855	-6015.198862	250.628
	225			-6015.012975	-6015.230215	273.654
	300			-6014.99508	-6015.264195	294.639
$B_{12}Br_{12}^{2-}$ + ACE	25	-31382.6905	-31382.53977	-31382.50306	-31382.61485	235.276
	150			-31382.47719	-31382.66636	280.535
	225			-31382.45995	-31382.70132	304.053
	300			-31382.44176	-31382.73896	325.384
$B_{12}I_{12}^{2-}$ + ACE	25	-4066.046907	-4065.901462	-4065.862477	-4065.98401	255.786
	150			-4065.836034	-4066.039723	302.061
	225			-4065.818524	-4066.077278	325.947
	300			-4065.800114	-4066.117547	347.539

Appendix B

Optimized structures for Chapter 4 given in XYZ coordinates.

$B_{12}H_{12}^{2-}$	X (Å)	Y (Å)	Z (Å)
B	-0.885871	0.126120	-1.442077
B	-0.887277	0.074094	1.444855
B	0.161507	1.418305	0.917965
B	0.162369	1.450481	-0.866141
B	-0.162369	-1.450480	0.866142
B	0.887276	-0.074094	-1.444854
B	1.534713	0.724508	0.013766
B	0.885871	-0.126119	1.442078
B	-1.334520	1.048333	0.018214
B	-0.161507	-1.418304	-0.917964
B	1.334519	-1.048333	-0.018213
B	-1.534713	-0.724507	-0.013765
H	-0.275749	-2.422412	-1.568155
H	-2.621263	-1.237670	-0.023587
H	-1.513199	0.215442	-2.463113
H	-2.279523	1.790517	0.031283
H	-1.515498	0.126305	2.467909
H	0.277159	2.477540	-1.479330
H	0.275748	2.422413	1.568156
H	2.621262	1.237670	0.023588
H	1.513199	-0.215442	2.463114
H	2.279523	-1.790516	-0.031282
H	-0.277160	-2.477540	1.479331
H	1.515498	-0.126304	-2.467908

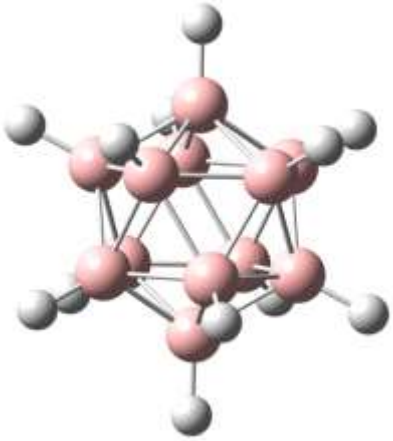

$B_{12}H_{12}^{-}$	X (Å)	Y (Å)	Z (Å)
B	0.408799	1.186102	-1.162329
B	-0.094033	-1.607381	-0.576759
B	-1.563405	-0.693266	-0.022096
B	-1.269639	1.039754	-0.481736
B	1.269645	-1.039749	0.481732
B	0.094038	1.607378	0.576752
B	-1.058672	0.508977	1.242907
B	-0.408806	-1.186105	1.162328
B	-0.705718	-0.197065	-1.545335
B	1.563405	0.693262	0.022100
B	0.705724	0.197070	1.545332
B	1.058672	-0.508967	-1.242905
H	2.657333	1.156366	0.063483
H	1.807589	-0.832558	-2.107366
H	0.662569	2.007476	-1.983183
H	-1.175568	-0.359195	-2.625060
H	-0.183699	-2.730271	-0.956133
H	-2.149785	1.777792	-0.787531
H	-2.657337	-1.156363	-0.063482
H	-1.807586	0.832566	2.107370
H	-0.662569	-2.007475	1.983187
H	1.175539	0.359167	2.625078
H	2.149757	-1.777818	0.787546
H	0.183707	2.730269	0.956129

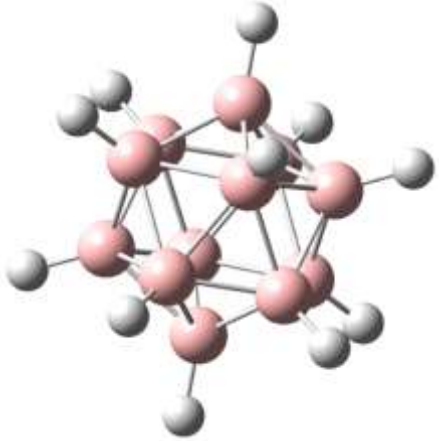

$B_{12}F_{12}^{2-}$	X (Å)	Y (Å)	Z (Å)
B	0.636036	-1.251241	-0.975087
B	-0.015348	-0.277932	1.686297
B	-1.526248	-0.287760	0.713381
B	-1.123641	-0.889290	-0.931437
B	1.123643	0.889292	0.931435
B	0.015350	0.277933	-1.686299
B	-1.321021	0.873373	-0.642742
B	-0.636034	1.251242	0.975085
B	-0.316673	-1.600857	0.507971
B	1.526250	0.287762	-0.713383
F	-2.766555	-0.521611	1.293122
F	-2.394591	1.583175	-1.165045
F	-2.036779	-1.611993	-1.688438
F	-0.573988	-2.901852	0.920719
F	-0.027776	-0.503790	3.056695
F	-1.152895	2.268118	1.767545
F	2.766557	0.521613	-1.293124
F	2.036781	1.611994	1.688436
F	0.573990	2.901854	-0.920721
F	2.394593	-1.583173	1.165042
F	1.152896	-2.268117	-1.767547
F	0.027778	0.503791	-3.056697
B	0.316674	1.600859	-0.507973
B	1.321023	-0.873371	0.642740

$B_{12}F_{12}^{-}$	X (Å)	Y (Å)	Z (Å)
B	0.659196	-1.173596	-1.083434
B	0.710717	0.056915	1.574024
B	-1.006080	-0.528169	1.301909
B	-1.000264	-1.370778	-0.327017
B	1.000264	1.370778	0.327017
B	-0.710717	-0.056915	-1.574024
B	-1.688916	0.321884	-0.172819
B	-0.659196	1.173596	1.083434
B	0.409381	-1.526317	0.698942
B	1.006080	0.528169	-1.301909
F	-1.792529	-0.982546	2.313517
F	-3.020057	0.581269	-0.267866
F	-1.811120	-2.425147	-0.607990
F	0.764459	-2.709393	1.266833
F	1.232778	0.111513	2.828070
F	-1.158759	2.126679	1.914195
F	1.792529	0.982546	-2.313517
F	1.811120	2.425147	0.607990
F	-0.764459	2.709393	-1.266833
F	3.020057	-0.581269	0.267866
F	1.158759	-2.126679	-1.914195
F	-1.232778	-0.111513	-2.828070
B	-0.409381	1.526317	-0.698942
B	1.688916	-0.321884	0.172819

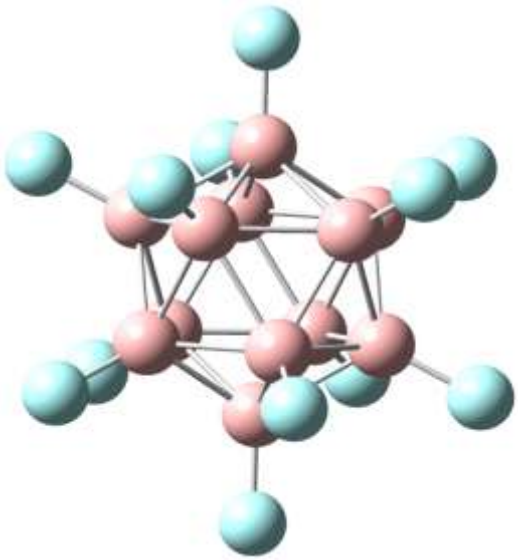

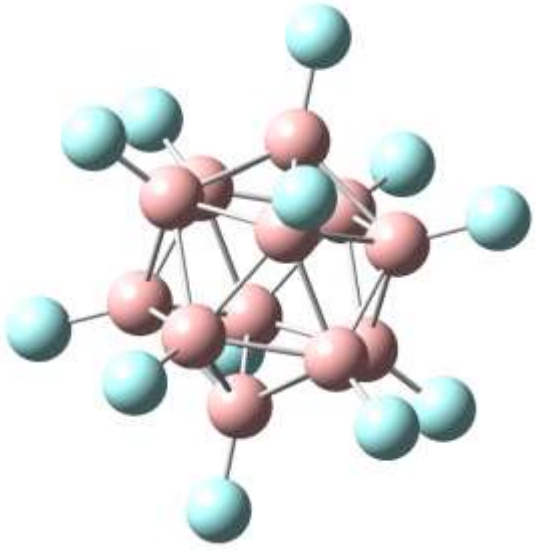

$B_{12}Cl_{12}^{2-}$	X (Å)	Y (Å)	Z (Å)
B	-0.269515	1.680806	0.039160
B	-1.045501	-0.960976	0.939482
B	0.663242	-0.697812	1.404413
B	1.142833	0.934831	0.848011
B	-1.142833	-0.934831	-0.848010
B	1.045501	0.960975	-0.939481
B	1.622015	-0.509103	-0.095703
B	0.269514	-1.680806	-0.039159
B	-0.505833	0.655576	1.487761
B	-0.663243	0.697812	-1.404412
B	0.505833	-0.655577	-1.487761
B	-1.622016	0.509103	0.095704
Cl	-0.555646	3.465656	0.080706
Cl	-1.042998	1.351863	3.067639
Cl	-3.344439	1.049704	0.197255
Cl	-1.367429	1.438752	-2.895874
Cl	2.155860	1.981360	-1.937100
Cl	2.356376	1.927626	1.748579
Cl	3.344439	-1.049704	-0.197254
Cl	1.042998	-1.351863	-3.067638
Cl	0.555645	-3.465656	-0.080705
Cl	-2.356377	-1.927626	-1.748578
Cl	-2.155861	-1.981360	1.937101
Cl	1.367428	-1.438752	2.895875

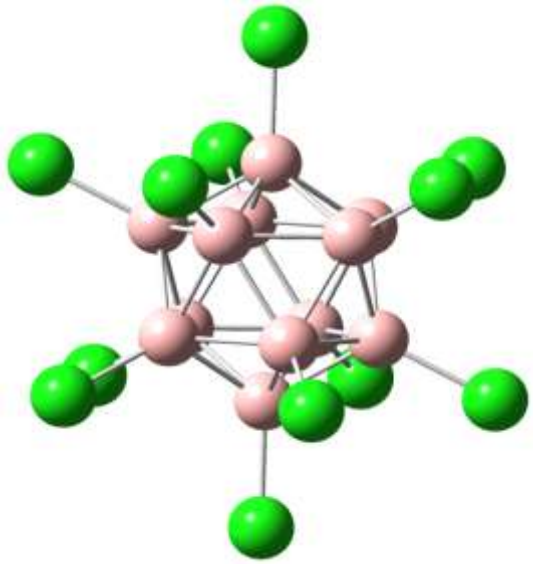

$B_{12}Cl_{12}^{-}$	X (Å)	Y (Å)	Z (Å)
B	-1.021520	-0.035488	1.380336
B	-0.676594	0.683507	-1.422961
B	-0.389804	-1.104167	-1.256529
B	-0.537884	-1.552435	0.500270
B	0.537884	1.552435	-0.500270
B	0.676594	-0.683507	1.422961
B	1.104314	-1.293935	-0.236965
B	1.021520	0.035488	-1.380336
B	-1.653960	-0.356437	-0.295055
B	0.389804	1.104167	1.256529
B	1.653960	0.356437	0.295055
B	-1.104314	1.293935	0.236965
Cl	-2.068402	-0.101176	2.819883
Cl	-3.377465	-0.705729	-0.576301
Cl	-2.239019	2.649334	0.454286
Cl	0.762525	2.253581	2.565278
Cl	1.397842	-1.366568	2.901389
Cl	-1.116180	-3.163210	0.993167
Cl	2.239019	-2.649334	-0.454286
Cl	3.377465	0.705729	0.576301
Cl	2.068402	0.101176	-2.819883
Cl	1.116180	3.163210	-0.993167
Cl	-1.397842	1.366568	-2.901389
Cl	-0.762525	-2.253581	-2.565278

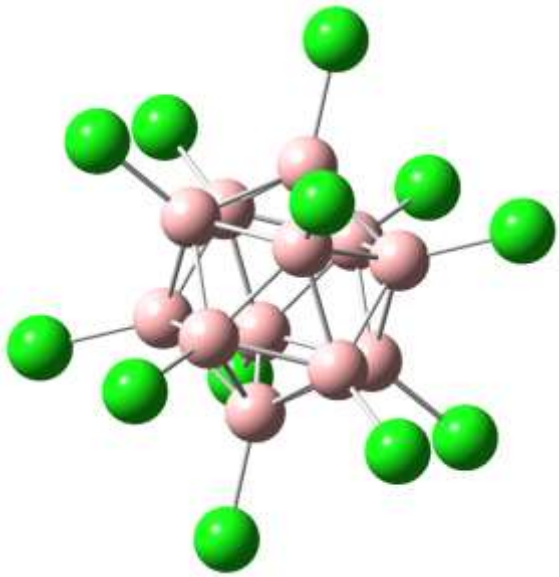

$B_{12}Br_{12}^{2-}$	X (Å)	Y (Å)	Z (Å)
B	-0.769531	-1.292332	-0.800987
B	1.167011	-0.415447	1.170322
B	-0.431294	0.251875	1.629159
B	-1.628129	-0.290079	0.410829
B	1.628130	0.290080	-0.410829
B	-1.167011	0.415447	-1.170322
B	-0.958015	1.369724	0.331684
B	0.769532	1.292332	0.800987
B	-0.314892	-1.393302	0.929190
B	0.431295	-0.251875	-1.629159
B	0.314892	1.393302	-0.929190
B	0.958015	-1.369724	-0.331684
Br	2.068125	-2.957394	-0.716319
Br	0.931303	-0.543795	-3.517531
Br	2.519517	-0.896797	2.526739
Br	3.515284	0.626204	-0.887098
Br	0.679991	3.008357	-2.005947
Br	1.661456	2.790081	1.729592
Br	-2.068124	2.957394	0.716319
Br	-0.931303	0.543795	3.517531
Br	-2.519517	0.896797	-2.526739
Br	-3.515284	-0.626204	0.887098
Br	-0.679990	-3.008357	2.005947
Br	-1.661456	-2.790081	-1.729592

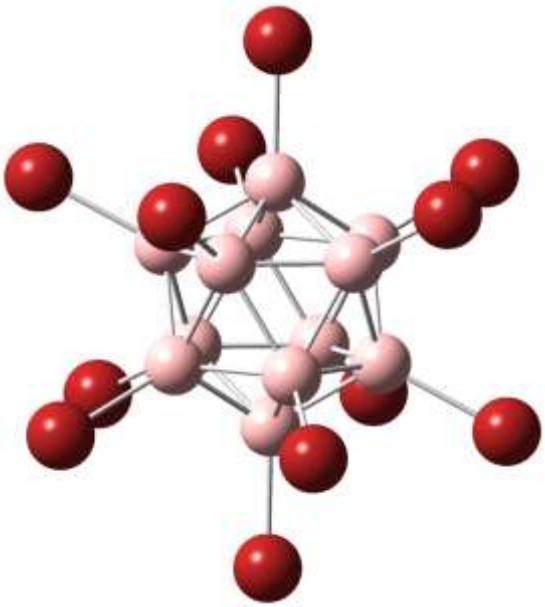

$B_{12}Br_{12}^{-}$	X (Å)	Y (Å)	Z (Å)
B	-1.189464	1.155021	0.447127
B	0.913990	0.361871	-1.407894
B	-0.301377	-0.987813	-1.371836
B	-1.634359	-0.459453	-0.256706
B	1.634359	0.459453	0.256706
B	-0.913990	-0.361871	1.407894
B	-0.382951	-1.642941	0.320457
B	1.189464	-1.155021	-0.447127
B	-0.859024	0.739138	-1.290034
B	0.301377	0.987813	1.371836
B	0.859024	-0.739138	1.290034
B	0.382951	1.642941	-0.320457
Br	0.803894	3.516981	-0.660348
Br	0.669175	2.096474	2.933921
Br	1.952993	0.744814	-3.013697
Br	3.489208	0.999768	0.525898
Br	1.811448	-1.593987	2.762090
Br	2.556992	-2.458291	-0.932730
Br	-0.803894	-3.516981	0.660348
Br	-0.669175	-2.096474	-2.933921
Br	-1.952993	-0.744814	3.013697
Br	-3.489208	-0.999768	-0.525898
Br	-1.811448	1.593987	-2.762090
Br	-2.556992	2.458291	0.932730

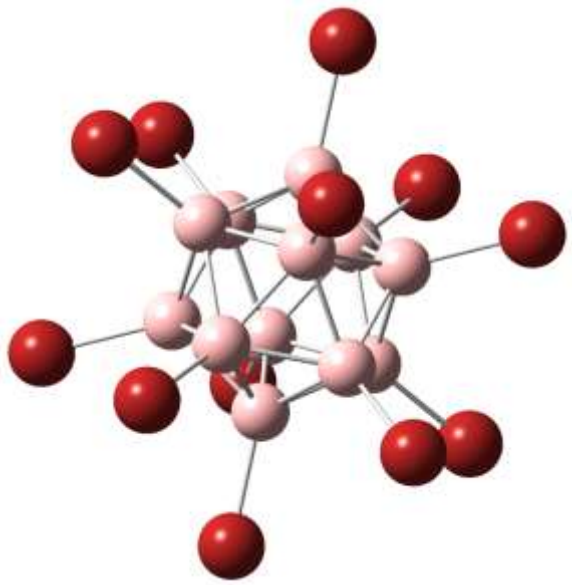

$B_{12}I_{12}^{2-}$	X (Å)	Y (Å)	Z (Å)
B	-0.091163	0.801856	1.507627
B	0.667133	-1.574647	0.010230
B	1.559112	-0.174509	-0.680377
B	1.090413	1.294136	0.245050
B	-1.090413	-1.294136	-0.245050
B	-0.667133	1.574647	-0.010230
B	0.352745	0.971156	-1.362507
B	0.091163	-0.801856	-1.507627
B	1.284735	-0.279200	1.093397
B	-1.559112	0.174509	0.680377
B	-1.284735	0.279200	-1.093397
B	-0.352745	-0.971156	1.362507
I	-0.807942	-2.222996	3.119594
I	-3.569387	0.399579	1.557623
I	1.526960	-3.604891	0.023778
I	-2.496817	-2.962673	-0.560849
I	-2.941125	0.639031	-2.503555
I	0.208559	-1.835778	-3.451536
I	0.807942	2.222996	-3.119594
I	3.569387	-0.399579	-1.557623
I	-1.526960	3.604891	-0.023778
I	2.496817	2.962673	0.560849
I	-0.208559	1.835778	3.451536
I	2.941125	-0.639031	2.503555

$B_{12}I_{12}^{-}$	X (Å)	Y (Å)	Z (Å)
B	0.333153	0.253924	-1.646150
B	-1.362127	-0.965909	0.364282
B	-1.365678	0.806225	0.636887
B	-0.316303	1.554567	-0.607360
B	0.316303	-1.554567	0.607360
B	1.362127	0.965909	-0.364282
B	0.310563	1.301398	1.046572
B	-0.333153	-0.253924	1.646150
B	-1.351587	0.156287	-1.033894
B	1.365678	-0.806225	-0.636887
B	1.351587	-0.156287	1.033894
B	-0.310563	-1.301398	-1.046572
I	-0.712960	-2.983262	-2.399742
I	3.115265	-1.846869	-1.458817
I	-3.107277	-2.212046	0.834395
I	0.726043	-3.563927	1.392259
I	3.083239	-0.358182	2.368140
I	-0.764627	-0.582090	3.774037
I	0.712960	2.983262	2.399742
I	-3.115265	1.846869	1.458817
I	3.107277	2.212046	-0.834395
I	-0.726043	3.563927	-1.392259
I	0.764627	0.582090	-3.774037
I	-3.083239	0.358182	-2.368140